Pharmacological Behavior of Systemically Administered Nanoparticles of Defined Properties: Mechanistic Investigations at the Organ, Tissue, and Cellular Levels

Thesis by

Chung Hang Jonathan Choi

In Partial Fulfillment of the Requirements

for the Degree of

Doctor of Philosophy

California Institute of Technology

Pasadena, California

2011

(Defended April 26, 2011)

To my dearest parents and brother,

for their incessant love and unwavering support
to my lifelong pursuit of dreams and happiness.

Acknowledgments

First and foremost, I would like to express heartfelt gratitude to my thesis advisor, Professor Mark Davis, for his mentorship. Mark's passion for science, engineering acumen, decisive judgment, effective communication skills as a scientist and leader, zeal for innovation, and commitment to education were sources of inspiration for me. From an inexperienced novice in science, Mark's tutelage catalyzed my metamorphosis to a more equipped scholar with higher intellectual maturity and technical prowess to tackle problems that matter to society.

Tremendous thanks must go to Dr. Paul Webster of the House Ear Institute (HEI). A significant portion of my thesis comprises microscopic studies of biological samples. Paul's rich experience and abundant knowledge in microscopy were extremely resourceful. From Paul, I came to appreciate microscopy as an artform and scientific discipline. From microscopy, I learned the importance of patience and meticulousness in research. I am also grateful to the kind assistance from Jennifer Bower, Debbie Guerrero, and Siva Wu from the HEI.

Serving as Teaching Assistant for Professor John Brady's courses on transport phenomena (ChE 151 ab) was a memorable journey. I deeply respect John's eloquent lecturing style, creative homework problems, incisive explanations, and genuine care for underperforming students in class. My dialogs with John cultivated my interest in transport, motivating me to incorporate insights from transport to understand behavior of therapeutic nanoparticles.

I must also thank Professor Zhen-Gang Wang, who showed consistent interest in my research as my thesis committee member. His effective lectures in statistical mechanics and polymer physics dawned on me the importance of using engineering fundamentals to interpret data.

I am indebted to the camaraderie displayed by all Davis research group members, past and present. Senior graduate students Christopher Alabi and Brendan Mack offered constructive criticism to my work when I commenced in the Davis group, constantly challenging me to improve and become a more independent researcher. Postdoctoral fellows Kuen-Chan Lee, Manuel Moliner Marín, Eranda Nikolla, Yuriy Román-Leshkov, and May Pang Xiong provided thoughtful advice on career planning and job applications. Devin Wiley and Jonathan Zuckerman gave critical evaluations to my engineering-oriented ideas within the context of medicine. Yashodhan Bhawe guided me in constructing my first ever chemical hood and fielded my questions on reaction engineering. Han Han gave useful advice in bioconjugate chemistry, and also was my uniquely caring officemate for 2.5 years. Leonard Medrano expanded my experimental toolbox in molecular biology. It was rewarding to work with SURF student Ioana Aanei, whose initiative and meticulousness made research in my final year fruitful and enjoyable.

I am grateful to the assistance received from various lab personnel outside my research group at Caltech. Gwen Williams taught me the essential techniques of animal manipulation. Carol Garland passed on insightful advice on TEM. Nathan Dalleska helped resolve ICP-MS related issues. I thank the Caltech Biological Imaging Center for training on confocal microscopy. Kathy Bubash and Martha Hepworth deserve much credit for efficient administrative support.

I am fortunate to have developed steadfast friendships with other members of the Caltech community. Among peer graduate students from other research groups within the chemical engineering (ChE) option, I shall not forget the deep conversations and warm encouragement derived from numerous dining excursions with Man Nin Chan, Joyce Huynh, Christina Ting, Candy Tong, Rui Wang, and Ming-Hsin Wei. I will salute ChE seniors Nicholas Brunelli, Arthur Chan, Yvonne Chen, and Sally Ng for salient advice. Other ChE peers of my year (Russ Komor, Joe Liang, Imogen Pryce, and Frank Truong) provided company and solidarity as we prepared

for qualifying exams. In the undergraduate circle, I would pay tribute to Eric Tai, who eased my transition to Caltech by exposing me to the intriguing aspects of Caltech dormitory culture (e.g., Ditch Day and Interhouse) as my neighbor at the Avery House. Justine Chia, Clara Eng, Dongying Shen, and Qinren Zhen generously brought me dessert, laughter, and company as moral support at moments of despair. Cultural exchanges with Jiayi Guo, Hiroko Okatsu, Alejandra Nieto Peña, and Helene Schmidt were illuminating during their sojourns as visiting scholars.

As my pastime, I played the violin and viola as part of the Caltech Chamber Music Program. I applaud Delores Bing for coaching my performances, and cherish fond memories of jamming music with Jackson Wang, whose passion in music motivated me to take up composition.

I will extend sincere gratitude to Christina Chan for her care and support. I shall not forget the episodes and vignettes from which we experienced, learned, and matured.

It was my honor to serve as the Hong Kong Student Association at Caltech as President. I am thankful for having built close rapport with Chefung Chan, Kawai Kwok, Lap Man Lee, Icy Ma, Heywood Tam, Raymond Tsang, and Wanwan Yang.

Sagacious advice from Sunney Chan, alumnus from Wah Yan College Hong Kong (my secondary school) and Caltech emeritus professor, were instructive, helping me reflect on my intellectual pursuits and define my future career goals. I also appreciate the generosity and friendship from members of the Wah Yan Past Student Association (SoCal chapter).

Unless otherwise mentioned, this thesis was primarily supported by the National Cancer Institute Grant CA 119347, the National Institute of Health Grants R01 EB004657 and NIH 2P30DC006272-06, as well as the Ahmanson Foundation.

Abstract

The objective of this thesis is to establish design rules for nanoparticle properties that enable their in vivo transport to target destinations. Gold nanoparticles containing surface-engrafted polyethylene glycol (PEG) chains are prepared with controlled physicochemical properties (hydrodynamic size, surface charge, targeting ligand density). Upon systemic injection into mice, the transport of nanoparticles is monitored by blood pharmacokinetics as well as distribution at the organ, tissue, and subcellular levels from the same injection in an individual animal.

At a constant, slightly negative surface charge (ca. -10 mV), most PEGylated gold nanoparticles (PEG-AuNPs) deposit in the liver, spleen, and kidney of normal mice 24 hours after injection. Increasing retention in the liver (Kupffer cells) and spleen correlate positively with increasing nanoparticle diameter over the range of 25-165 nm, largely due to phagocytic uptake. Accumulation in the kidney is size-dependent, but shows a maximum uptake at ca. 75 ± 25 nm that also gives the highest deposition in the mesangium (uptake by mesangial cells).

Tumor-bearing mice received injections of PEG-AuNPs of near-constant size (ca. 75 nm) and surface charge (ca. -10 mV) but with variable amounts of ligands that target cancer cells (0-144 ligands per nanoparticle). Independent of ligand content, nanoparticles accumulate in the tumor by the enhanced permeation and retention effect to the same magnitude, and adjacent to leukocytes. Nanoparticles only enter cancer cells in significant amounts when they contain targeting ligands above a threshold amount (between 18 and 144 ligands per nanoparticle).

Mechanistic studies from model nanoparticles provide insights for the delivery of therapeutic nanoparticles. Systemic administrations of targeted, cyclodextrin-based, siRNA-containing nanoparticles are investigated in animals and humans (Phase I clinical trial). A fluorescent chemical stain with exposed adamantane molecules for binding into the cyclodextrin cups of the targeted nanoparticles is created, allowing for the examination of tumor tissue sections from animals and patient biopsies. Results from both animal and human tissues reveal intracellular, dose-dependent accumulation of targeted nanoparticles in cancer cells of the tumor.

Contents

List of Figures

List of Tables

Chapter 1

Introduction

Chemical engineering (ChE) as an academic discipline has undergone much revision and innovation over the past decades, characterized by its rapid expansion from petroleum sciences into new frontiers such as medicine, microelectronics, and environmental sciences. With advances in computing, instrumentation, and synthesis and characterization of nanomaterials (e.g., biological [1], colloidal [2]), modern ChE has switched its focus from studying large-scale reactions or mechanisms to processes at the molecular/atomic level in the past three decades [3]. Armed with knowledge across multiple time and length scales, modern chemical engineers can contribute more to the emerging field of nanotechnology.

General interest in nanotechnology is enormous. Nanoscale objects can have properties (e.g., strength, electric conductivity, melting point, color, and magnetic moment) different from those of their macroscopic equivalents, owing to fundamental principles of quantum physics, and have seen their widespread application in many commercial prodicts. Giant magnetoresistive heads found in computer hard drives have nanoscale structural dimensions to reduce the size required for storing memory bits. Textiles blended with nanoparticles are in vogue due to their impressive stain-proof, water-proof, and wrinkle-resistant properties.

Bionanotechnology

Like ChE, biological sciences have also adopted a more “reductionist” approach [4], with their pedagogical focus shifting away from the “ensemble perspective” (e.g., anatomy and physiology) to “individual perspective” (e.g., cellular biology and molecular pharmacology). The manipulation of biological processes, mechanisms, and pathways (all building blocks that contribute to the integrated process of life [5]) have been conducted at the nanoscale level [6]. More exquisite tools from physics and chemistry are available to image and control the properties of cell membranes, proteins, nucleic acids, or even atoms (all of nanoscale dimensions).

Integration of nanotechnology with biotechnology, as well as with information technology and cognitive science, is expected to accelerate in the next decade [7]. In particular, “bionanotechnology” integrates nanoscale principles and techniques with biological systems in the development of biomimetic nanostructures, design tools and devices to facilitate biomedical research, and generate new therapeutics [8]. Active nano-based research by biomedical engineers began around 1999, accompanied by the concomitant increase in government support.

The ability to control material properties on the nanoscale catalyzes the development of novel diagnostics and imaging agents for detecting diseases [9]. Silicon-based nanowires can electrically detect femtomolar concentrations of marker proteins overexpressed in cancer cells present in blood serum [10]. Gold nanoparticles conjugated with DNA strands can identify marker proteins at a sensitivity of a million times higher than conventional ELISA assys [11], and have been extended to detect nucleic acid sequences, small molecules, and inorganic ions as well [12]. When injected in mice, cadmium-selenium quantum dots can reveal sentinel lymph nodes [13] and recently lung tissues [14] located at centimeters beneath the skin under near-infrared light.

Reasons for the widespread use of nanosized objects in biomedical applications are multifold. Despite their smallness, nanosized objects (1-1000 nm in diameter) are still considerably larger than molecules, and hence can receive surface engraftment of different types of moieties to achieve multiple functions simultaneously (e.g., target receptors, image cells, and inhibit gene). The smallness also translates to a high surface area to volume ratio, allowing more dense and compact packing of moieties on their periphery. Finally, the nanoscale dimension corresponds to the typical size of fenestrations and tight junctions of most tissues and cells.

As of 2006, drug delivery represents the most popular branch within the field of nanomedicine, netting the highest number of publications, patents, and commericalized products compared to biomaterials, active implants, in vitro diagnostics, and in vivo imaging agents [15]. As therapeutic delivery systems, nanoparticles allow targeted delivery and controlled release. For diagnostic applications, nanoparticles allow detection on the molecular scale.

Nanoparticle-based drug delivery

A historical perspective

The key objective of a delivery system is to release therapeutics at the desired anatomical site, at a suitable concentration and for a desired duration, independent of the route of administration (e.g., oral, parenteral, pulmonary, transdermal, systemic). For the past five decades, techniques such as compression, spray and dip coating, and encapsulation are widely used in the pharmaceutical industry to imbibe therapeutics with polymers [16]. Since the first report of sustained drug release systems in the 1970s [17], the field of drug delivery witnessed the development of new classes of polymer-based drug delivery devices, including diffusion-controlled, solvent-activated (swelling- [18] or osmotically controlled [19]), chemically controlled (biodegradable) [20], and environmentally induced systems (e.g., pH, temperature) [21].

Therapeutic nanoparticles are now under intense development for the treatment of diseases such as cancer, inflammatory disorders, and cardiovascular disease [22] [23]. Upon their administration, they can selectively accumulate in biological sites, enhance the delivery of the drug payload in the most non-invasive and cost-effective manner (i.e., utilizing minimal dosage to achieve maximal potency). Two archetypal therapeutic nanoparticles that laid the cornerstone for modern nanoparticle-based drug delivery are **liposomes** and **polymer–drug conjugates**.

Initially discovered in the 1960s [24], liposomes are spherical vesicles with a phospholipid bilayer membrane structure that can encapsulate both hydrophilic and hydrophobic agents. They are biologically inert and weakly immunogenic, and thus constitute attractive vehicles for delivering different types of therapeutic cargo (e.g., small molecules, nucleotides, proteins). Drug-loaded liposomes were first reported in 1973 [25], yet their in vivo delivery suffered from severe uptake by mononuclear macrophages and serum complement components. Their interaction with lipoproteins also led to the premature release of the cargo in blood [26]. Such limitations prompted the development of “stealth” liposomes [27] and “long-circulating” liposomes [28], both with longer circulation half-lives and reduced toxicity than the free drug. The first liposome-based therapeutic, liposome-encapsulated doxorubicin (Doxil), received FDA approval in 1995 for the treatment of HIV-related Kaposis sarcoma. The basic concept of liposomes spurred the development of new-generation nanocarriers (e.g., virosomes [29], polymersomes [30]) and new liposome-based applications (e.g., photothermal therapy [31], diagnostic imaging [32]). By modifying the lipid structure, liposomes can also contain targeting ligands (e.g., monoclonal antibodies or fragments, peptides, glycoproteins, carbohydrates, or receptor ligands) and form “immunoliposomes”, to enhance the selective accumulation in desired tissue and cellular locations [33] [34].

As a point of digression, other nanocarrier systems for drug delivery also appeared at the same time as drug-containing liposomes, although they did not receive as much attention as liposomes. One notable exception is albumin-bound paclitaxel (Abraxane) [35] [36], the first protein-based nanoparticle to receive FDA approval for the treatment of metastatic breast cancer in 2005. Polymeric nanoparticles, micelles, nanoshells, dendrimers, viral nanoparticles, metallic nanoparticles, and ceramic nanoparticles have also shown therapeutic potential in multiple branches of medicine, such as oncology, immunology, neurology, ophthalmology, and orthopedics [37].

Polymer-drug conjugates, the second important class of nanoparticle-based therapetics besides liposomes, first appeared in the 1970s [38]. Since their conception, polymer coating has immediately become an indispensable component of modern nanoparticle-based therapeutics to regulate their in vivo behavior. For sustained drug release applications, biodegradable polymers (e.g., poly(ϵ-caprolactone), poly(lactic acid) (PLA), poly(glycolic acid) (PGA), and their copolymers) have been under development for over two decades [39] [40] [41]. To prolong blood pharmacokinetics, hydrophilic and non-immunogenic polymers such as poly (ethylene glycol) (PEG) and N-(2-hydroxypropyl)methacrylamide (HPMA) have proven to be very effective. The next section features an overview of PEG in nanoparticle forumulations.

Poly (ethylene glycol)

Poly (ethylene glycol) (PEG) has a general structure of $\mathrm{HO}–(\mathrm{CH_2CH_2O})_n–\mathrm{CH_2CH_2}\text{-}\mathrm{OH}$ (polydispersity = 1.01), encompassing a chemically inert polyether backbone, with terminal hydroxyl groups that can be activated for conjugation to different types of polymers and drugs. It has high solubility in both organic and aqueous solvents. Despite its gradual decomposition in vivo by enzymolysis [42] and hydrolysis [43], PEG still represents the most common and validated polymer used in drug delivery formulations compared to other alternatives, such as dextran, chitosan, heparin, poly (amino acids), and vinyl polymers.

PEG has long been utilized as a modification agent of individual proteins, peptides, antibodies (and their fragments). Many therapeutic proteins have limited bioavailability due to their continuous enzymatic degradation by serum proteins. They require high doses to maintain efficacy, which can impart immunological risks. In 1977, Abuchowski et al. pioneered the covalent attachment of methoxy-PEG (mPEG) to bovine liver catalase, and reported marked improvements in blood circulation and reduced immunogenicity [44]. Most importantly, PEGylation (the covalent attachment of PEG) did not drastically hamper the biological activity of the enzyme. As a significant breakthrough in drug delivery, this study sparked the development of a plethora of PEG-protein conjugates [45] [46] [47] for various biomedical applications in the 1980s. Owing to its bulkiness and hydrophilicity, PEG augments the hydrodynamic size of the conjugated proteins far beyond the increase in molecular mass [48]. Due to their flexibility, PEG chains can shield protein sites from recognition by the immune system, cellular receptors, or proteases. Thus, PEG-protein conjugates are more resistant to non-specific uptake by the organs (e.g., liver, spleen) of the reticuloendothelial system (RES), and can remain in blood circulation in a prolonged manner to reach as well as accumulate in the target organs [49]. With multiple PEG_{5000} strands connected to each molecule of therapeutic protein, PEGylation enhanced the circulation of the protein by 3-4 times. Representative PEG-protein conjugates that met FDA approval include Adagen (bovine adenosine deaminase-PEG) [50] and Oncaspar (L-asparaginase-PEG) [51]. Despite the increase in blood circulation and solubility, PEGylation can adversely affect protein binding, leading to the concomitant reduction in functional activity (e.g., internalization, intracellular transport, and lyzosomal degradation) [52]. The recent creation of site-specific PEG modification techniques has shown promise in ameliorating the undesirable loss in protein function associated with random PEGylation [53] [54].

In contrast to therapeutic proteins, small-molecule drugs suffer from limited bioavailability due to poor aqueous solubility, high toxicity, rapid excretion, and untargeted biodistribution. To improve their solubility and extend their blood circulation, PEGylation typically entails polymer chains of at least 40,000 in molecular weight to avoid renal clearance [55] [56]. The conjugation chemistry for non-protein drugs is facile because of less functional groups present on a small molecule, absence of conformational constrains, and simpler purification and characterization procedures for the conjugates [57]. Examples of PEG-small molecule conjugates include PEG-paclitaxel [58] and Prothecan (PEG-camptothecin) [59], and PEG-doxorubicin [60]. A key drawback with PEGylation of small molecules lies on the low loading of PEG, with only 1-2 hydroxyl terminal groups per strand for activation. The recent development of multi-arm PEG-containing dendrimers permits the engraftment of multiple copies of PEG-small molecule conjugates on the same structure to increase loading [61] [62]. Dendrimers are highly branched, globular structures with an initiator core and mulitple layers of polymer strands.

In general, reaction with PEG derivatives does not alter the mechanism of action of a therapeutic protein/ small molecule. It enhances its therapeutic effect by altering its pharmacokinetics.

Thesis objectives

Spurred by advances in wet chemistry and fabrication techniques, nanosized objects can now assume different physical properties (e.g., hydrodynamic size, geometry, rigidity, porosity), surface properties (e.g., surface functionality, charge, hydrophobicity, polymer type and grafting density), targeting ligands (e.g., proteins, peptides, aptamers, small molecules, antibodies), and chemical composition (e.g., carbon nanotubes and bucky balls, quantum dots, supramagnetic oxide nanoparticles, nanocrystals, nanowires, nanocages, polymeric micelles). Such "modularity" allows for the creation of an infinite assortment of nanoparticles of various properties. Each class of nanoparticles will demonstrate distinct in vivo profiles (e.g., blood clearance, drug-release kinetics, tissue accumulation, intracellular localization, toxicity, and drug stability) [63] [64].

This thesis elucidates the **structure-function relationships** between nanoparticle properties and their in vivo behavior. Its objective is to seek new **mechanistic understanding** in factors that govern the systemic delivery of nanoparticles to biological desinations in vivo. Below features sample mechanistic approaches to examine the effects of two nanoparticle properties, particle size and targeting ligand density, for drug delivery applications.

Various physiological mechanisms are responsible for nanoparticle clearance from blood circulation. Rigid quantum dots smaller than 5 nm experience renal filtration via urine. On the other hand, metallic nanoparticles larger than 100 nm face severe removal by phagocytosis of the liver and spleen. Mechanistic studies that examine in vivo behavior as a function of **particle size** (Chapters 2 and 4) permit the optimization of nanocarriers with longer blood circulation.

Upon diffusion into the target tissues, systemically delivered nanoparticles must enter cells to exert their desired therapeutic action by crossing the cell membrane. With decoration of ligands, targeted nanoparticles can bind to receptors on the cell membrane with enhanced affinity and specificity. Internalization of the receptor/ligand complexes leads to receptor-mediated endocytosis of the targeted nanoparticles. Alternatively, nanoparticles can interact with the membrane via hydrophobic and electrostatic interactions and enter the cell through pinocytosis. For the first approach, mechanistic studies that examine in vivo behavior as a function of **ligand density** (Chapter 3) enables the design of nanoparticles with elevated intracellular accumulation.

Brief pharmarcology

The illustration of in vivo nanoparticle behavior warrants an introduction to the fundamental concepts in pharmacology, a field that examines the interactions between a living organism and chemicals that affect biochemical functions [65], such as drug composition, toxicity, and therapy. The two main areas of pharmacology are **pharmacokinetics** and **pharmacodynamics**.

Pharmacokinetics (PK) determines the in vivo fate of substances administered externally to a living organism [66]. It analyzes the extent and rate of liberation (release of chemicals from the formulation), absorption (entry into blood circulation), distribution (dispersion or dissemination in fluids and tissues), metabolism (irreversible decomposition into daughter metabolites), and excretion (elimination of the substances from the body). Some recurrent PK parameters discussed throughout this thesis are dose (D; quantity of injected drug), concentration (C_p; drug concentration in plasma), volume of distribution ($V_D = D/C_0$, where C_0 is the initial concentration), area under the curve ($\mathrm{AUC} = \int_0^\infty C_p dt$; integral of the plasma drug concentration (C_p) after injection), clearance ($\mathrm{CL} = D/\mathrm{AUC} = V_D \times K_e$; volume of plasma cleared of the drug per unit time, where K_e is the elimination rate constant), and biological half-life ($t_{1/2} = \ln 2/K_e$; time required for the drug concentration to reach half of its original value).

Pharmacokinetics (PD) determines the biochemical and physiological effects of drugs on the body, mechanisms of drug action, and relationship between drug concentration and effect [67]. Several PD concepts mentioned in this work include toxicity, dose-response relationships (e.g., efficacy, potency, cellular uptake), and ligand-receptor binding interaction.

Gold nanoparticles

For all mechanistic studies, this thesis involves the intravenous administration of model nanoparticles into mice to analyze their in vivo nanoparticle behavior. Below summarizes the rationales behind the use of PEGylated gold nanoparticles as model probes.

Due to their electronic, optical, fluorescent, and magnetic properties, metallic nanoparticles have found diverse applications in catalysis, energy, medicine, electronics, and the environment. Most applications of metallic nanoparticles stem from two principles: (1) surface functionalization to attain desirable in vivo properties (e.g., colloidal stability, biocompatibility, molecular targeting); (2) excitation of the surface plasmons to explore their unique optical properties across the vis-NIR band [68]. A significant portion of this thesis entails the use of PEGylated gold nanoparticles to interrogate the in vivo targeting of biological sites.

Gold nanoparticles (AuNPs) have a long history of use, dating back to the 5th century B.C. for making ruby glass and adding a reddish tinge to ceramics. Hindu chemists for Ayurveda, the

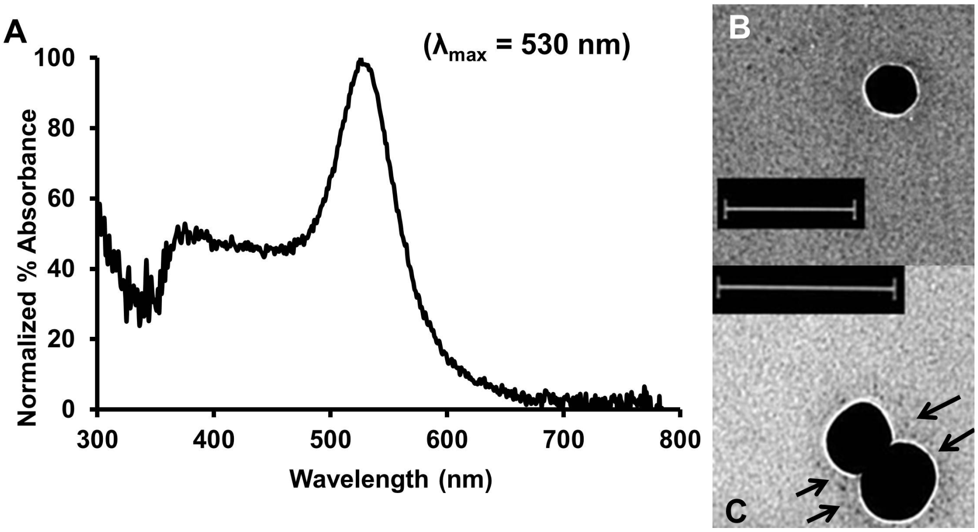

Figure 1.1: Properties of gold nanoparticles. (A) The large surface plasmon peak at 530 nm allows for easy quantification of bulk gold particle (diameter = 50 nm) content by UV-Vis spectrometry. (B) The high electron density of gold nanoparticles by transmission electron microscopy (TEM). (C) Negative staining by 1% phosphotungstic acid reveals the faint halo of PEG_{5000} layer (marked by black arrows) covalently grafted on the periphery of 80 nm gold nanoparticles under TEM. Scale bar = 100 nm.

ancient system of Indian medicine, prepared "longevity" concoctions based on gold colloids [69]. Significant experimental progress made from the 19th and 20th centuries aimed at deciphering the nature of colloidal matter. Faraday first examined the optical properties of metallic colloids (including AuNPs), within the context of aggregation and sedimentation [70]. Zsigmondy constructed an ultramicroscope to visualize the size and mobility of colloidal dispersions, and later developed the "seed-mediated" method to create AuNPs [71]. Svedberg pioneered the use of electrochemical methods to make AuNPs, and later invented analytical ultracentrifugation to size AuNPs [72]. Meanwhile, theoretical advances by Einstein [73], Smoluchowski [74], and Langevin [75] enriched the understanding of the continuous Brownian motion of colloidal suspensions.

Nanosized gold constitutes the most popular class of nanoparticles used in biomedical applications, ranging from targeted delivery (small molecule drugs, genetic materials, antigens), cellular imaging, medical diagnostics, to treatment of diseases (tumors or rheumatoid arthritis) [76] [77]. Several intravenous applications using nanosized gold for cancer treatment are currently under early clinical development, such as AurImmune [78], AuriTol, and AuroLase [79].

AuNPs provide a well-defined, rigid core for surface modification with ligands. Scalable synthesis of monodisperse AuNPs with tunable dimensions is straightforward [80] [81]. The strong surface plasmon peak of AuNPs allows easy detection by UV-Vis spectrometry (Fig. 1.1A). For surface modification, purification of AuNPs from unreacted ligands by centrifugation is facile owing to the high density of gold ($\rho = 19.3$ g/cm^3). Dynamic light scattering (DLS) can characterize the hydrodynamic size and surface charge, by treating AuNPs as a dilute suspension of spherical spheres that exhibit strong Mie scattering [82]. Without non-spherical contaminants or aggregates (which can drastically skew the scattering intensity), DLS can provide reasonably accurate mean values for the physicochemical parameters of a single AuNP.

The examination of in vivo targeting necessitates the detection of nanoparticles in biological structures. The current "gold standards" to quantify bulk gold concentrations of tissues are inductively coupled plasmonic mass spectrometry (ICP-MS) [83] and instrumental neutron activation analysis (INAA), with an about 0.02-1 ppb detection limit. Atomic absorption spectroscopy (AAS) can also measure bulk gold content, albeit at a lower sensitivty. AuNPs can catalyze the selective reduction of silver ions to metallic silver and the subsequent deposition of metallic silver onto the particle surface. This "silver enhancement" method allows for their visualization of AuNPs as size-enhanced entities in tissue sections (prepared from routine histological procedures) under light microscopy (LM) [84]. Electron microscopy (e.g., transmission electron microscopy (TEM) and scanning electron microscopy (SEM)) can ascertain localization of AuNPs in cells and subcellular compartments, owing to the high electron density of AuNPs (Fig. 1.1B). When used together with energy dispersive X-ray spectroscopy (EDX) and X-ray absorption spectroscopy (XAS), EM can provide additional information about elemental data and structural information of gold and sulfur atoms, respectively. This thesis employs ICP-MS, histology with silver enhancement, and TEM to provide a top-down elucidation of in vivo distribution of AuNPs on organ, tissue, and (sub)cellular levels from the same animal (Fig. 1.2).

Like their bulk metal counterpart, AuNPs generally have low in vitro toxicity independent of size and geometry [85], opening the door for their i.v. injection and examination of their in vivo pharmacological behavior. When exposed to AuNPs with negative or neutral capping agents (e.g., citrate, biotin, glucose, cysteine), cells internalized AuNPs up to 100 µM with no apparent sign of toxicity. At minute concentrations (10 nM), the same cells showed toxicity for AuNPs capped with cetyltrimethylammonium bromide (CTAB), a structure directing agent with a quarternary amine group [86]. While cationic AuNPs induce toxicity than anionic AuNPs (perhaps due to the electrostatic interaction between positive particles and negative cell membranes [87]), this phenomenon depends on the specific cell lines under investigation [88].

Particle stability is crucial to maintain the physicochemical parameters (e.g., size, surface charge, targeting ligand density) of nanoparticles constant in vivo. Such parameters must be optimal to achieve effective delivery to the target site as individual entities and thus elicit the desirable biological response. While most naked nanoparticles are inherently stable in deionized water due to charge repulsion, the addition of salt induces charge screening and protein adsorption, respectively, shielding their surface charge and leading to particle aggregation. Unmodified nanoparticles (e.g., metallic, liposomes, latex) are also subject to non-specific binding by blood serum proteins (most notably fibrinogen, albumin, trypsin, apoproteins, immunoglobulins, and complement factors [89] [90] [91]) onto their periphery, causing their enlargement in size and elevated ability to cause blood clotting [92]. By grafting with PEG chains that serve as extended brush layers, adjacent nanoparticles are less vulnerable to salt- and serum-induced aggregation by maintaining considerable separation distance between particles.

The decoration of AuNPs with a monolayer of thiolated PEG (PEG-SH) via the formation of covalent gold-thiol linkages (bond energy = 30-40 kJ/mol [93]) is a popular approach to confer steric stability to AuNPs. For each AuNP grafted with alkanethiols, crystallization and X-ray structure determination studies show that all sulfur atoms bind in a bridge conformation to two

Organ level biodistribution (ICP-MS)

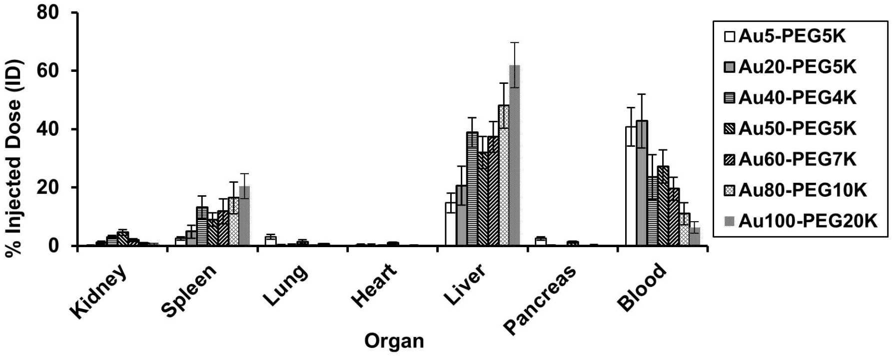

Tissue level biodistribution (Light microscopy)

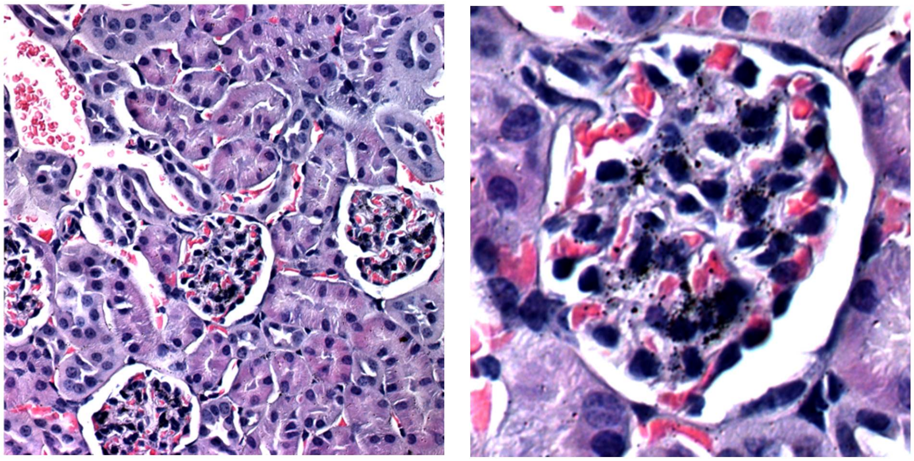

Cellular level biodistribution (TEM)

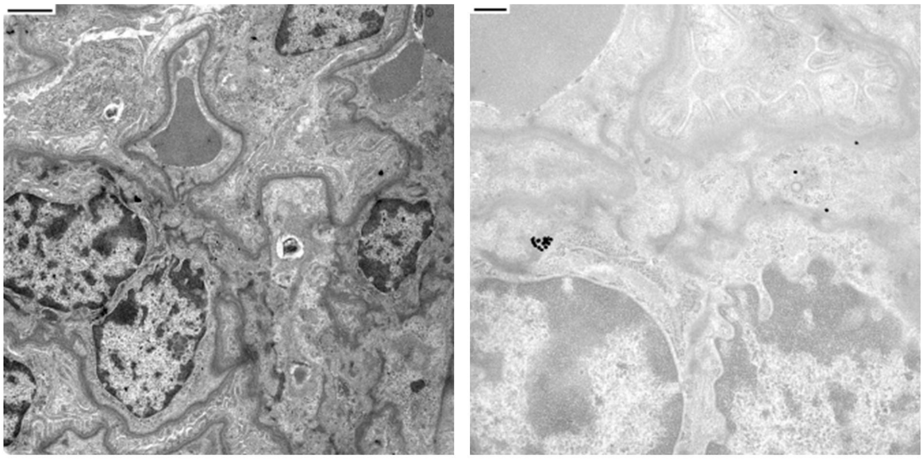

Figure 1.2: Levels of biodistribution. Inductively coupled plasma mass spectrometry (ICP-MS), light microscopy (LM) with silver enhancement, and transmission electron microscopy (TEM) collectively monitor the in vivo distribution of PEGylated gold nanoparticles at the organ, tissue, and cellular levels, respectively. Representative data of each imaging method is provided to illustrate this top-down approach in tracking particle localization in the kidney.

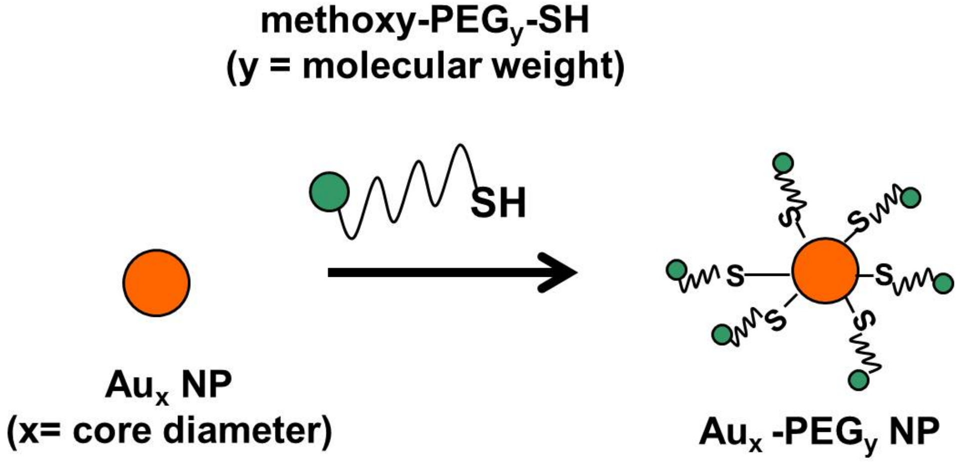

Figure 1.3: Assembly of Au$_x$-PEG$_y$ NPs. Unmodified gold nanoparticles of different core sizes (x) (Au$_x$ NPs) were reacted with methoxy-PEG-SH of different molecular weights (y) in deionized water for 30 min at RT under constant stirring to form PEGylated gold nanoparticles (Au$_x$-PEG$_y$ NPs).

gold atoms, at least one of which binding to two sulfurs, forming a "staple" motif [94]. Due to the soft character of gold and sulfur, sulfur ligands (e.g., alkanethiols, xanthates, disulfides, mercaptoalkanoic acids) can chelate to gold atoms to form thiolated AuNPs of reduced dispersity, controlled size, and stability in air and against heat [95]. Fig. 1.1C illustrates a 80 nm AuNP with covalent engraftment of mexthoxy-PEG$_{5000}$-thiol chains on the surface.

Thesis structure

Chapters 2-4 represent mechanistic studies in mice that received i.v. administration of PEGylated gold nanoparticles as in vivo model probes. Chapter 5 reports a technical development in ex vivo detection methods that employs PEGylated gold nanoparticles as the contrast agent.

Chapter 2 ascertains the mechanistic effects of passive tumor targeting. Using tumor-bearing mice, it studies the effect of particle size on tumor retention, clearance by the liver, and accumulation in the kidney. Results from passive targeting define the optimal particle size for subsequent analysis of active targeting using liganded nanoparticles.

Chapter 3 examines the mechanistic effects of active tumor targeting. Using probes with surface decoration of human transferrin (a popular ligand for cancer targeting), it investigates the effects of targeting ligand density attached onto the nanoparticle as well as receptor expression levels of cancer cells on the intracellular accumulation of nanoparticles in the tumor.

Investigations until now entailed the development of targeted delivery strategies for cancer applications. Chapter 4 demonstrates the translation of insights derived from tumor targeting to the targeting of other biological sites. In particular, it presents a novel approach that selectively targets the kidney mesangium, via the adjustment of nanoparticle properties (e.g., size and surface charge) in accordance to the unique characteristics of renal physiology.

Chapter 5 deviates from the design of delivery strategies using model nanoparticle probes. Instead, it evaluates the effectiveness of drug delivery by tracking the in vivo distribution of **actual** therapeutic nanoparticles. Through the creation of a novel chemical stain that can specifically recognize cyclodextrin-polymer (CDP) conjugates in cells, animal tumors, and patient tumor biopsies, this chapter reveals pharmacological insights of CDP-based therapeutic nanoparticles.

Appendix A details the materials and methods for common techniques, including dynamic light scattering (DLS), inductively coupled plasma mass spectrometry (ICP-MS), histology with silver enhancement, confocal immunofluorescence microscopy, and transmission electron microscopy (TEM). Protocols specific for individual studies are listed at the end of each chapter.

Appendix B provides theoretical justifications of using model PEGylated gold nanoparticles to mimic the in vivo flow patterns of actual therapeutic nanoparticles with reference to simple arguments from fluid mechanics. It lends support to the applicability of the data from Chapters 3 and 4 to interpret clinical results from Chapter 5.

NOTES

Table 1.1 presents abbreviations and their associated meanings used throughout this thesis.

Abbreviation	Meaning
RT	Room temperature
1× PBS	1× Phosphate buffered saline (150 mM NaCl, 2.7 mM KCl, 10 mM Na_2HPO_4, 2 mM K_3PO_4, pH = 7.4)
D5W	5% Dextrose in water
PFA	Paraformaldehyde
DMEM	Dulbecco's Modification of Eagle's Medium
FBS	Fetal bovine serum
i.v.	Intravenous
s.d.	Standard deviation
PEG_y	Poly (ethylene glycol) (Molecular weight: y Da)
Au_x NP	Gold nanoparticle (Core diameter: x nm)
Au_x-PEG_y NP	PEGylated gold nanoparticle
Tf	Transferrin
TfR	Transferrin receptor
% ID	Percent injected dose
LM	Light microscopy
TEM	Transmission electron microscopy
ICP-MS	Inductively coupled plasma mass spectrometry
DLS	Dynamic light scattering
HD	Hydrodynamic diameter
ZP	ζ-potential
EPR	Enhanced permeation and retention
RES	Reticuloendothelial system
siRNA	Small interfering ribonucleic acid
N2A	Neuro2A cells (mouse neuroblastoma)

Table 1.1: List of abbreviations.

Chapter 2

Optimizing the Nanoparticle Size for Passive Tumor Targeting

2.1 Abstract

As nanoparticles are receiving enormous attention as drug delivery agents for cancer applications, mechanistic analysis of the effect of physicochemical parameters on the in vivo fate of nanoparticles can lead to the more targeted delivery of nanoparticle-based therapeutics to the tumor. Here, we examine the in vivo distribution of nanoparticles as a function of particle size. Mice bearing subcutaneous Neuro2A tumors (mouse neuroblastoma) received i.v. injections of PEGylated gold particles (Au_x-PEG_{5000} NPs) of different sizes in the submicron size range (x = 20, 50, and 80; final hydrodynamic size $\leq$ 100 nm). All particles demonstrate steric stability against physiological concentrations of salt. Histological and TEM data captured the tissue and cellular level in vivo distribution of Au_x-PEG_{5000} NPs in the tumor, liver, and kidney 24 h after dosing. Au_x-PEG_{5000} NPs entered the tumor by the enhanced permeation and retention (EPR) effect, and primarily localized near leukocytes in the tumor interstitium regardless of particle size. Smaller particles (Au_{20}-PEG_{5000} NPs) could infrequently enter Neuro2A cells and reside in either vesicles or cytoplasm. Phagocytic response in the liver was largely size dependent, as reflected by more severe sequestration (6-fold increase by stereological estimates) of Au_{80}-PEG_{5000} NPs compared to Au_{20}-PEG_{5000} NPs by Kupffer cells. In the kidney, Au_{50}-PEG_{5000} and Au_{80}-PEG_{5000}

NPs had noticeably more accumulation inside renal corpuscles than Au_{20}-PEG_{5000} NPs. Based on these observations, passive tumor targeting using i.v. administered nanoparticles is optimal when particle diameter is <70 nm to prevent RES clearance, with concomitant implications of toxicity due to residency of particles within renal corpuscles.

2.2 Introduction

Cancer is currently the top killer in the world. With over 12 million incidents globally in 2008, cancer incidence is projected to further increase by 69% by 2030. In economic terms, the burden of cancer (cost of years lost from ill health, disability, or early death) outweighs all other health concerns, such as heart diseases, HIV/AIDS, liver cirrhosis, and malaria [96]. Since the 1970s, death rates from most common forms of cancer in the United States have not fallen, and the total number of US deaths each year from lung and pancreatic cancers has doubled [97].

A major emphasis in nanomedicine research is the development of sub-100 nm structures to improve the diagnosis and treatment of cancer. Early and non-invasive diagnosis of maligancies, imaging of tumor profiles and contours, and selective eradication of abnormal cells without harming healthy population are long-standing goals in cancer research [98]. In the past decade, nanotechnology has shown enormous utility in developing tools and strategies for cancer applications, as exemplified by the creation of immunoliposomes injected i.v. for the treatment of breast cancer [99], targeted nanosized contrast agents for imaging brain tumors [100], and nanoparticle-based methods for the specific detection of oncological DNA and protein [101].

Yet, these technological advancements do not yield a fundamental understanding in the interaction of nanosized objects with biological structures in vivo. The paucity of knowledge for their impact on environment, safety, and health (ESH) raises the eyebrows of the public following the growing prevalence and diversity of nano-inspired technologies. To support their continued

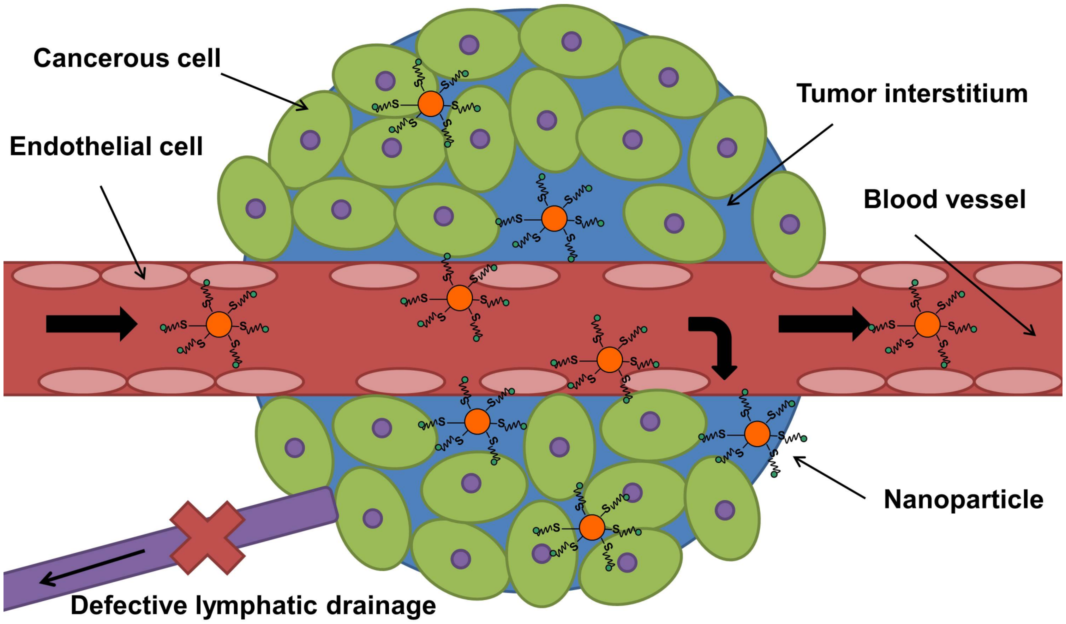

Figure 2.1: Passive tumor targeting. Passive tumor targeting of nanoparticles is achieved by extravasation of nanoparticles through the leaky tumour vasculature and ineffective lymphatic drainage (enhanced permeation and retention (EPR) effect). Over time, a concentration gradient between the tumor vasculature (high) drives the irreversible accumulation of nanoparticles in the tumor interstitium (low). The interstitial pressure increases to that of the tumor vasculature.

use in cancer applications and address EHS concerns, one possible route is to investigate the in vivo distribution of nanostructures. Here, we explore the effect of size, a key physicochemical property of nanoparticles, on the in vivo distribution in mice bearing solid tumors.

Tumor biology in brief

Tumors are solid lesions formed by an abnormal growth of cells. Depending on the stage of cancer progression, nature of mutation (carcinoma, sarcoma, or lyphoma), and primary organ, tumors can assume very hetereogenous morphological elements. Thus, developing a therapy that can target multiple cancer types across different patient populations can be a daunting task.

Most solid tumors demonstrate common physiological characteristics, such as hypervasculature (large network of vasculature), porous endothelium, and defective lymphatic drainage system [102]. These features poses significant challenges to the accumulation of macromolecular therapeutics within the tumor, including (1) heterogeneous blood supply (which limits delivery to well-perfused regions of the tumor); (2) high interstitial pressure (which reduces extravasation of fluid and macromolecules in the high interstitial pressure regions); and (3) large transport distances in the interstitium (which prolongs the diffusion of marcomolecules within the tumor) [103]. If there exists a tumor targeting strategy that accounts for all these general features of tumor biology, then this strategy is expected to be applicable to a broad class of tumors.

Passive targeting

From a seminal study in 1986, i.v. injected molecules of high molecular weight (e.g., IgG antibody, MW = 150 kDa) would preferentially accumulate within the tumor of mouse xenograft models than their lower molecular weight counterparts (e.g., anti-tumor protein NCS, MW = 12 kDa) [104]. This differential tumor accumulation as a function of molecular weight emerges after 3-6 h, with the gap reaching to its maximum plateau value after 24 h. This phenomenon, now called the "enhanced permeability and retention (EPR) effect," universally applies to macromolecular agents (e.g., liposomes, micelles, polymeric nanoparticles) for targeting solid tumors.

"Passive targeting" exploits the unique features of tumor biology that allow nanosized objects to accumulate in the tumor by the EPR effect. Unlike free drugs that may diffuse randomly, nanosized objects can penetrate into the tumor tissue via the leaky vessels (extravasation). The porous blood vessels enables rapid fluid intake into the tumor interstitium from the blood vessels. The dysfunctional lymphatic drainage traps the influx fluid and the nanosized objects within the tumor interstitium, providing sufficient time for nanosized objects to engage the tumor cells (Fig. 2.1). The threshold particle size for extravasation into tumors is <400 nm, but other studies have shown that particles with diameters <200 nm are more effective [105].

The discovery of the EPR effect represents a paradigm shift, empowering the sustained delivery of therapeutics or contrast agents (in the form of nanoparticles) within the tumor at elevated concentrations. It spurred the development and commercialization of nanoparticle-based therapetuics in the 1990s, most notably liposomes and polymer-protein conjugates, in treating multiple cancer indications ranging from lyphoma, heptaoma, leukemia, and sarcoma [106].

Despite its proven clinical utility, the EPR effect suffers from several limitations. The random retention of nanoparticles in the tumor due to the EPR effect is difficult to control, and can contriubte to multiple drug resistance (the expulsion of therapeutics out of cancer cells within the tumor) [107]. The EPR effect relies on the permeability of blood vasculature in a particular tumor type, and permeability can be very heterogeneous even within a single tumor tissue [108]. One viable approach to overcome such limitations of passive targeting is "active targeting," via the surface decoration of targeting ligands on nanoparticles to engage receptors overexpressed on cancerous cells within the tumor. In Chapter 3, we will provide a mechanistic analysis of the in vivo fate of actively targeted nanoparticles as a function of ligand density and receptor density.

Here, we examine the mechanistic aspects of passive targeting in tumor bearing mice as a function of particle size. In particular, we investigate the in vivo distribution of PEGylated gold nanoparticles (used as model probes) in the tumor, liver, and kidney. Biological structures are filled with fenestrations, allowing for the transport of nutrients and metabolic prodicts into and out of tissues, cells, and even subcellular compartments. These gaps assume a submicron length scale ($\sim 10^0$ (pores of outer mitochondrial membrane) - 10^2 nm (endothelial linings of tumor vasculature)). Thus, submicron-sized nanoparticles, once injected in vivo, are expected to reach various destinations based on their relative sizes to those of pore in different organs. Besides transport patterns, size can also affect cellular responses. Here, we will underscore the effect of size on phagocytosis of nanoparticles by hepatic macrophages. In Chapter 4, we will observe a unique size range in which intake of nanoparticles by kidney mesangial cells is maximal. Results are valuable for optimizing the design of nanoparticles for tumor targeting.

2.3 Results and Discussion

Characterization of Au$_x$-PEG$_{5000}$ NPs

We prepare an array of PEGylated gold nanoparticles of different sizes (Fig. 1.3) as model probes. Dynamic light scattering (DLS) measurements confirmed the initial hydrodynamic sizes of all citrate-stabilized gold nanoparticles (Au$_x$ NPs) in deionized water ($20 \leq x \leq 150$), where x denotes the core size of the gold core (in nm). At their unmodified forms, Au$_x$ NPs are stable against aggregation in deionized water due to repulsion of surface negative charges. Upon the addition of physiological levels of salt (e.g., 1× PBS), unmodified Au$_x$ NPs experienced rapid and pronounced aggregation. The long error bars associated with the mean sizes of the unmodified Au$_x$ NPs in 1× PBS reflected the stochastic nature of particle aggregation.

The addition of excess methoxy-PEG$_{5000}$-thiol (mPEG$_{5000}$-SH) to AuNPs in deionized water led to the formation of PEGylated gold nanoparticles (Au$_x$-PEG$_{5000}$ NPs). The mean diameter of Au$_x$-PEG$_{5000}$ NPs in 1× PBS was roughly identical to that of the same particles in water. Thus, Au$_x$-PEG$_{5000}$ NPs of all sizes were stable against salt-induced aggregation (Fig. 2.2A).

In general, PEGylation led to an increase in the hydrodynamic size of an AuNP by ∼20-30 nm, implying that the PEG$_{5000}$ layer grafted on the gold surface amounted to 10-15 nm. Polymers tethered on surfaces experience forces due to entropy (leading to a random-walk configuration) as well as solvent-monomer interactions (favoring a swollen configuration). The first scaling models originated from free energy balance arguments to ascertain chain dynamics on planar surfaces [109] [110], and these results were subsequently extended to curved surfaces [111] [112]. The average brush height ($\overline{L}$) of the grafted polymer corona on a spherical particle (e.g., collidal nanoparticles, micelles, star polymers) of radius R takes the following form:

$$\overline{L} \sim bN^{3/5}\sigma^{1/5}\left(R/b\right)^{2/5}$$

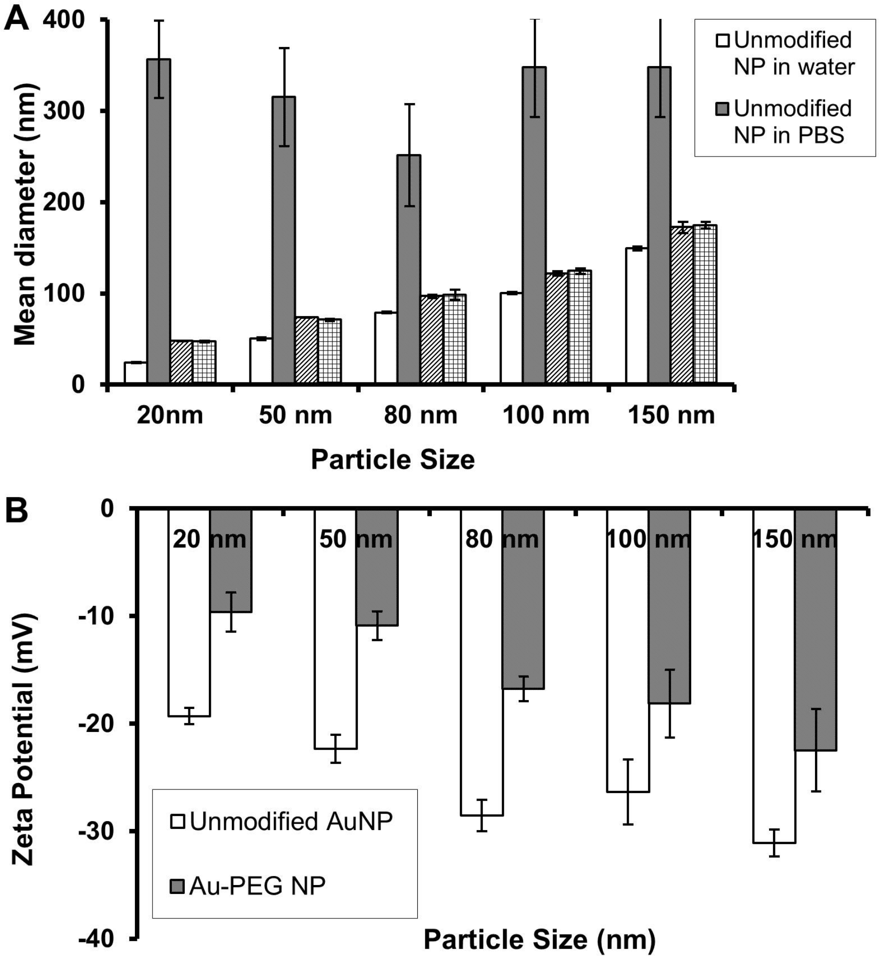

Figure 2.2: Physicochemical characterization of Au_x-PEG_{5000} NPs. (A) Colloidal stability. PEGylation provides AuNPs with steric stability against salt-induced aggregation. (B) Charge shielding. PEGylation of unmodified Au_x NPs gave less negative particles. Error bars bracket one s.d. from five measurements.

The PEG monomer, (CH_2CH_2O), bears a molecular weight of 44 g/mol a bond length of 0.44 nm (from one C-C bond of length 0.15 nm and two C-O bonds of length 0.145 nm each). So PEG_{5000} has $5000 \div 44 \approx 114$ monomers, and the total contour length of PEG_{5000} is 0.44 nm $\times$ 114 = 50 nm. Assuming a Kuhn length b of 0.8 nm for PEG (twice its persistent length [113]), the number of Kuhn segments in each polymer chain, N, is 50 nm $\div$ 0.8 nm = 62.5. Suppose that $\sigma = 0.1$ [114], then $\overline{L}$ for Au_x-PEG_{5000} NPs (x = 20, 50, and 80) lies in the range of 15-30 nm. DLS measurements match reasonably well with predictions from polymer physics.

Another consequence of PEGylation is charge screening. Unmodified Au_x NPs of all dimen-

	HD_W (nm)	ζ (mV)
Au_{20}-PEG_{5000}	43.1 ± 0.2	-9.62 ± 1.83
Au_{50}-PEG_{5000}	78.8 ± 0.2	-10.91 ± 1.33
Au_{80}-PEG_{5000}	97.1 ± 1.9	-16.77 ± 1.14
Au_{100}-PEG_{5000}	121.9 ± 2.6	-18.14 ± 3.16
Au_{120}-PEG_{5000}	172.5 ± 6.1	-22.5 ± 3.83

Table 2.1: Physiochemical properties of Au_x-PEG_{5000} NPs. HD_W = hydrodynamic diameter in deionized water; ζ = zeta potential in 1 mM KCl. The standard deviation originate from values due to five measurements.

sions are negatively charged due to the surface capping of citrate groups. This magnitude of negative charge increases with x. The covalent grafting of PEG_{5000} gave rise to less negative Au_x-PEG_{5000} NPs (Fig. 2.2B). To understand charge screening in quantitative terms, we can calculate the Debye length (κ^{-1}) of the electrolyte in which the ζ-potential measurements were made. For a binary electrolyte, κ^{-1} takes the following form:

$$\kappa^{-1} = \left(\frac{\epsilon k_B T}{2z^2 e^2 c_0} \right)^{1/2}$$

e, z, c_0, ϵ, k_B, and T depict the elementary charge, ionic valency, ionic concentration, permittivity of water, Boltzmann's constant, and temperature, respectively. For 1 mM KCl at RT, $\kappa^{-1} \sim 10$ nm. For unmodified Au_x NPs (20 nm $< x <$ 150 nm), $\kappa x/2 \sim$ 1-7.5, indicating that the charges are neither diffuse or concentrated near the particle surface. From above, the addition of PEG_{5000} increases the total size by 10-15 nm. The new $\kappa x/2$ of Au_x-PEG_{5000} NPs $\sim$ 2-10. PEGylation slightly increased $\kappa x/2$ and somewhat provided charge screening, but did not completely screen the negative charges of the unmodified AuNPs (Table 2.1).

Systemic administration

Armed with this set of Au_x-PEG_{5000} NPs, we proceed to inject them i.v. into mice bearing subcutaneous Neuro2A tumors (mouse neuroblastoma) at the same particle concentration. This concentration (4.5×10^{11} particles/mL) represents a careful balance between signal detectability and ease of administration. In a typical intravenous (i.v.) injection, only ~1 of every 100,000 molecules of monoclonal antibodies reaches their parenchymal targets in vivo [115][116]. An overloaded injection of concentrated particles may lead to the formation of a highly viscous formulation, not favorable for the tolerance of the animals (see Appendix B).

After 24 h, mice were sacrificed for the collection of the tumor, liver, and kidney. In subsequent chapters, most in vivo distribution measurements originate from the same time point (24 h after injection) to allow for sufficient time for the onset of the EPR effect in the tumor.

Below are results from imaging studies that elucidate the in vivo distribution of the Au_x-PEG_{5000} NPs (x = 20, 50, and 80) at the tissue and cellular levels, as a function of particle size 24 h after injection. Animal experiments did not include the largest two particle sizes (x = 100 and 150) due to the emphasis on the in vivo behavior of sub-100 nm nanoparticles. (For completeness, Chapter 4 contains data regarding the in vivo blood pharmacokinetics and organ-level distribution of Au_x-PEG_y NPs in non-tumor bearing mice as a function of size.)

Tumoral distribution

In agreement with most neoplastic tissues, Neuro2A tumor (mouse neuroblastoma) contains three compartments (vascular, interstitial, and cellular). The tumor comprises three cell types, subcutaneously implanted Neuro2A cancerous cells, leukocytes (or tumor associated macrophages (TAM)), and blood endothelial cells, all dispersed in a collagen-rich matrix. Due to its defective lymphatic drainage system, continuous fluid intake from the blood capillaries into the intersititial space gives rise to a high interstitial fluid pressure and velocity [117].

Like normal neurons, Neuro2A cells possess a large, round, and euchromatic nucleus with a single prominent nucleolus. Such nuclei are sometimes termed *owl-eye* or *fried-egg*. Unlike normal neurons, Neuro2A cells do not possess basophilic masses of endoplasmic reticulum in their cytoplasm. They lack the large and extended cytoplasm characteristic of normal neurons.

Neuro2A cells are regularly packed in the absence of connective tissues (Fig. 2.3A-C2).

Au_x-PEG_{5000} NPs of all dimensions agglomerated in the vicinity of leukocytes, due to the leakiness and irregularity of the tumor blood vessels (Fig. 2.3A-C1). While PEGylation was shown to reduce non-specific uptake, the injection of nanoparticles, foreign to the mouse, triggered an inflammatory response and led to their entrapment among connective tissues and leukocytes. During an inflammation, activated immune cells secrete cytokines that attract more cells to destroy the invading nanoparticles. Cationic particles are more likely to induce inflammatory reactions than anionic and neutral species [118].

Very rarely did these particles enter the Neuro2A cells, as seen by the clarity of their cytoplasm. Yet, smaller particles can localize between cancerous cells. Au_{20}-PEG_{5000} NPs could slide into the thin capillary vessels separating neighboring Neuro2A cells as well as localize into the cell cytoplasm, but not 70 and 100 nm particles. The size of pores of the tumor vasculature may affect whether particles can enter the Neuro2A cells. Yuan et al. reported a cutoff size of 400-600 nm for fluorescently labeled liposomes (25-160 kDa) to cross the pores of vasculature of LS174T (human colon adenocarcinoma) [119]. Hobbs et al. demonstrated the tumor dependence of vasculature pore cutoff sizes spanning from 100 to 800 nm by injecting latex microspheres i.v. to mice bearing subcutaneous carcinoma, hepatoma, glioma, and sarcoma tumors [120].

Based on the histological images, stereology (see supporting information) can provide semi-quantitative estimates of the tissue level particle distribution in the tumor. More particles concentrated near the leukocytes than Neuro2A cells for all particle sizes (Table 2.2). Given that each mouse received the same dosage of particles, these results illustrates the independence of the degree of inflammation as a function of particle size.

TEM reveals the subcellular localization of Au_x-PEG_{5000} NPs following the inflammatory response triggered by their i.v. injection. The Au_{20}-PEG_{5000} NPs lied near the fenestrated endothelium of the Neuro2A cells, implying their entry to the cytosol through the pores. Evidently,

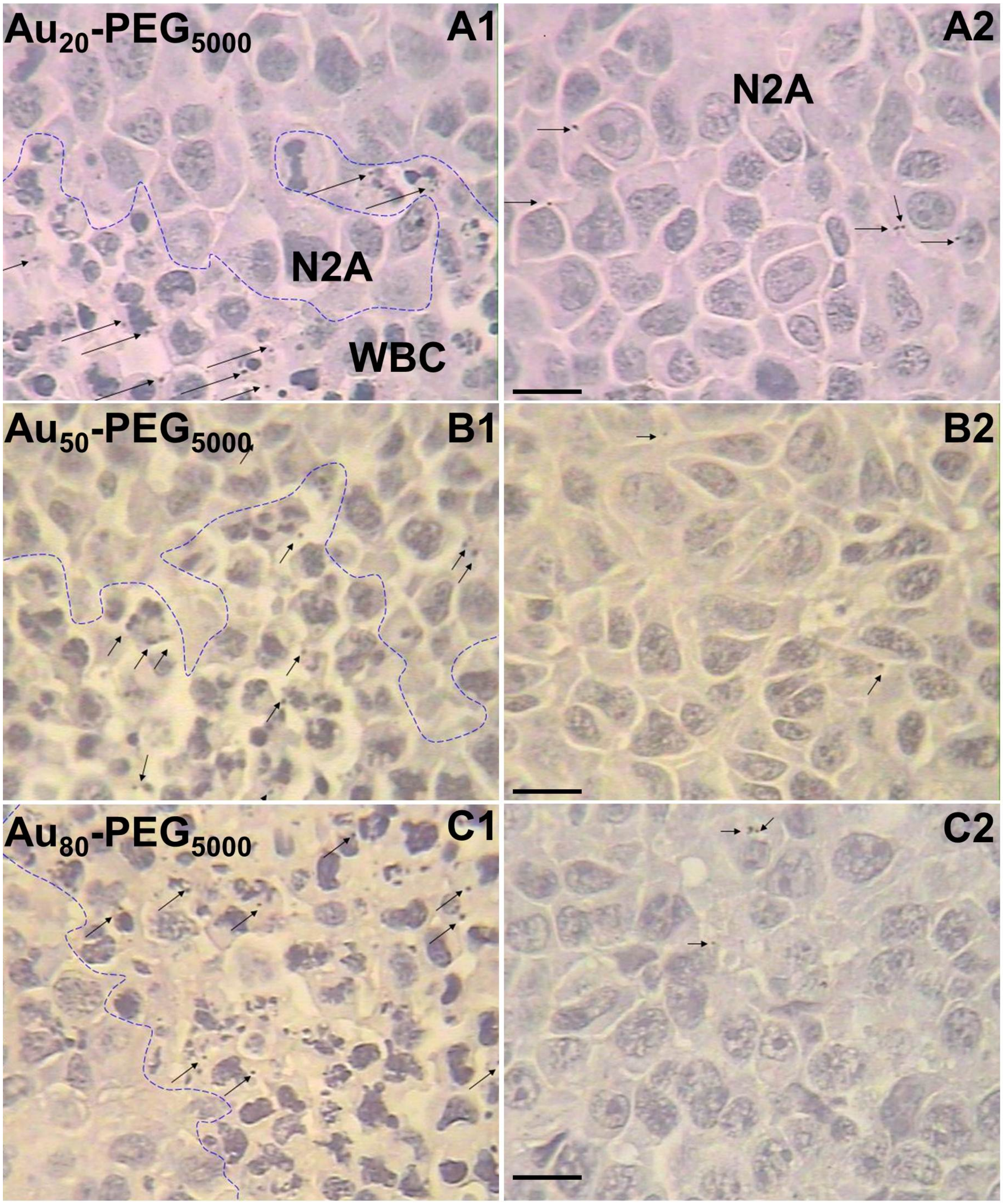

Figure 2.3: Intratumoral tissue level distribution of Au$_x$-PEG$_{5000}$ NPs. (A) Au$_{20}$-PEG$_{5000}$ NPs; (B) Au$_{50}$-PEG$_{5000}$ NPs; (C) Au$_{80}$-PEG$_{5000}$ NPs. Column 1: Neuro2A cells (N2A) and leukocytes (WBC); Column 2: Neuro2A cells. Black arrows indicate Au$_x$-PEG$_{5000}$ NPs deposited with silver. The blue dotted line separates WBCs and N2A cells. Scale bar = 10 µm for light micrographs.

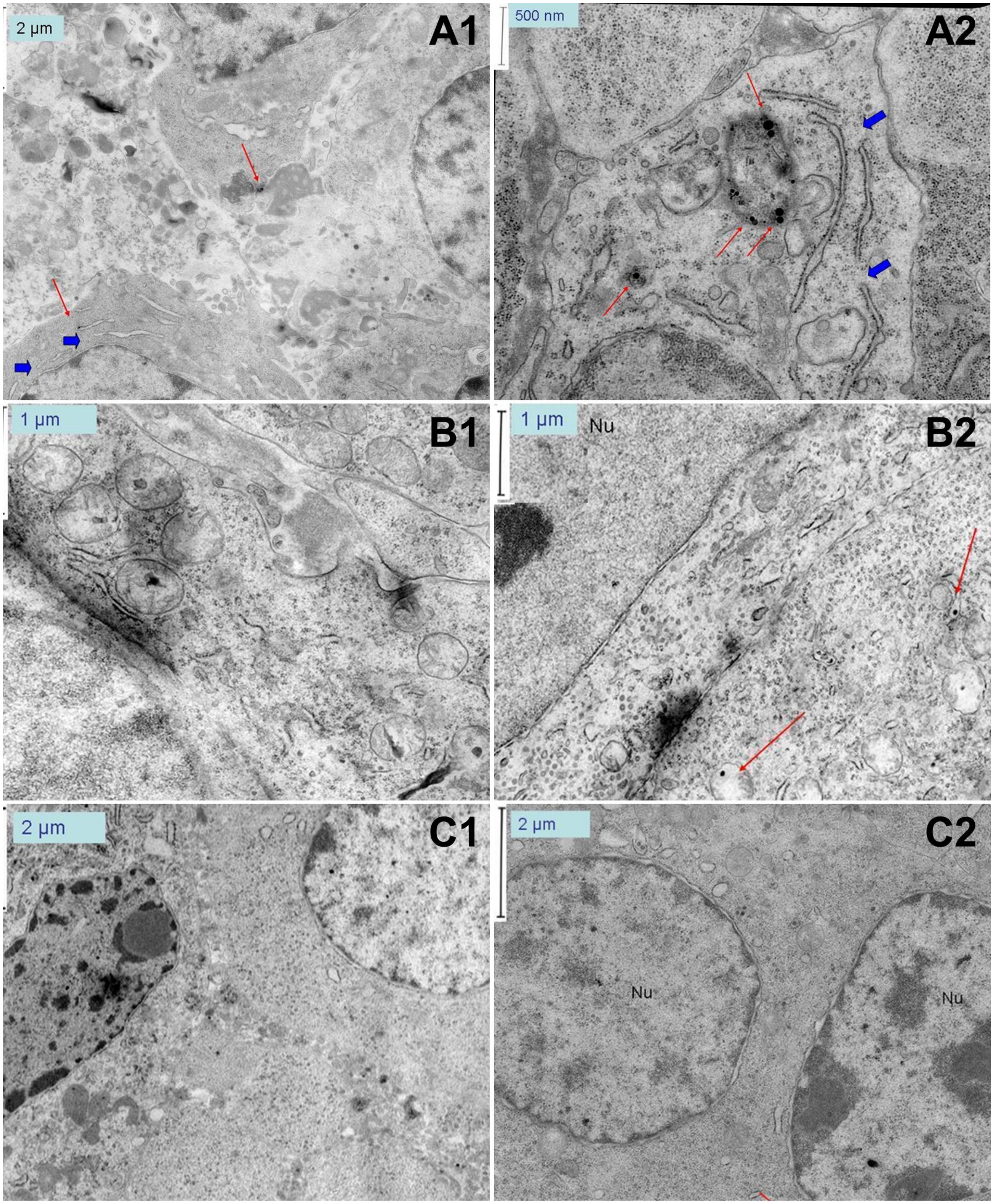

Figure 2.4: Intratumoral cellular level distribution of Au$_x$-PEG$_{5000}$ NPs. (A) Au$_{20}$-PEG$_{5000}$ NPs; (B) Au$_{50}$-PEG$_{5000}$ NPs; (C) Au$_{80}$-PEG$_{5000}$ NPs. Column 1: Neuro2A cells (N2A) and leukocytes (WBC); Column 2: Neuro2A cells. Red arrows point to actual Au$_x$-PEG$_{5000}$ NPs. Legend: Nu = nucleus.

	L	N2A	L/N2A
Au_{20}-PEG_{5000}	4.76	1.21	3.93
Au_{50}-PEG_{5000}	38.17	3.44	11.10
Au_{80}-PEG_{5000}	46.05	17.44	2.64

Table 2.2: Areal density of Au_x-PEG_{5000} NPs inside the tumor (# particles/mm^2). Legend: N2A = Neuro2A cells; L = leukocytes. Examples of "leukocytes" include basophils, neutrophils, basophils, lymphocytes, monocytes, and macrophages.

the pore width is larger than the particle size. Fig. 2.4A2 demonstrates the encapsulation of Au_{20}-PEG_{5000} NPs into a vesicle inside the cytoplasm. Both electron micrographs allow an estimate of the heterogeneous pore widths of fenestrated endothelia. While the labeled pores in Fig. 2.4A1 had approximate dimensions of 500 and 640 nm, the two indicated pores in Fig. 2.4 A2 measured roughly 370 and 250 nm. Thus, the average width of a pore in the endothelial cell of Neuro2A vasculature is **440 nm**.

Fig. 2.4B1-2 illustrate the cytoplasmic region of Neuro2A cells. The presence of Au_{50}-PEG_{5000} NPs in these regions was significantly lower than that of Au_{20}-PEG_{5000} NPs. When particles were visible, they usually resided inside vesicles in the cytoplasm. The same observation prevailed in the Neuro2A cytoplasm when the mice received injections of Au_{80}-PEG_{5000} NPs. Fig. 2.4C1-2 portray a low density of particles. These four images collectively suggest a bias in distribution of Au_x-PEG_y NPs away from the Neuro2A cells, consistent with the predominant localization of particles near the leukocytes, as observed from histological studies.

Hepatic distribution

Upon administration, considerable amounts of nanoparticles often accumulate in the liver. Thus, it is instructive to investigate the distribution of nanoparticles in the liver.

"Phagocytosis" describes the uptake of particles (traditionally larger than 0.5 µm) into cells, via mannose receptor-, complement receptor-, Fcγ receptor, and scavenger receptor-mediated pathways [121]. It entails the elimination of pathogens, cell debris, or foreign objects by cells known as macrophages. They engulf foreign material with their plasma membranes to form phagosomes. After the content becomes degraded in a lysosome, it either departs the cell by exocytosis or remains in the cell for further processing. For lower organisms, phagocytosis is critical for the uptake of nutrients and degradation of infectious agents. It participates in development, tissue remodeling, and immune response. Multiple macrophages of the "reticuloendothelial system" (RES) exist in the body, such as monocytes in lymph nodes and the spleen [122].

In the liver, the corresponding macrophages are Kupffer cells. By means of phagocytosis, these cells recycle erythrocytes by splitting hemoglobin for bile secretion. Kupffer cells (KCs) partially occlude the sinusoid lumen but have no functional attachments to the endothelial cells or to the underlying hepatocytes. Their location, primarily at the periportal end of the sinusoids, confirms that they monitor arriving blood, looking for particles to remove from blood flow.

Larger particles elicited more severe phagocytic responses. While few Au_{20}-PEG_{5000} NPs were observed near KCs, many Au_{50}-PEG_{5000} and Au_{80}-PEG_{5000} NPs agglomerated in their vicinity. Moreover, larger particles were predominantly localized in the vicinity of KCs, whereas smaller particles were more evenly distributed. While Au_{20}-PEG_{5000} NPs assumed a rather even spread among hepatocytes and KCs, Au_{50}-PEG_{5000} and Au_{80}-PEG_{5000} NPs resided near the KCs (Fig. 2.5A-B). Also, according to stereological measurements, more Au_x-PEG_y NPs localized in the vicinity of KCs than hepatocytes or other cell types with larger particle dimensions, confirming the presence of a phagocytic response. This response is size-dependent and increases by 6-fold as the particle size increases from 40 to 100 nm (Table 2.3).

TEM elucidated the phagocytosis phenomenon at the cellular level. Au_{20}-PEG_{5000} NPs sporadically dispersed in the vicinity of hepatocytes, without any particular tendency to agglomerate near KCs (Fig. 2.6A1-2). Fig. 2.6B1 captures the phagocytosis of small clusters (3-5 particles per cluster) of Au_{50}-PEG_{5000} NPs of numerous lyzosomes inside a Kupffer cell, located between a hepatic sinusoid (populated by an erythrocyte) and the Space of Disse. The Space of Disse

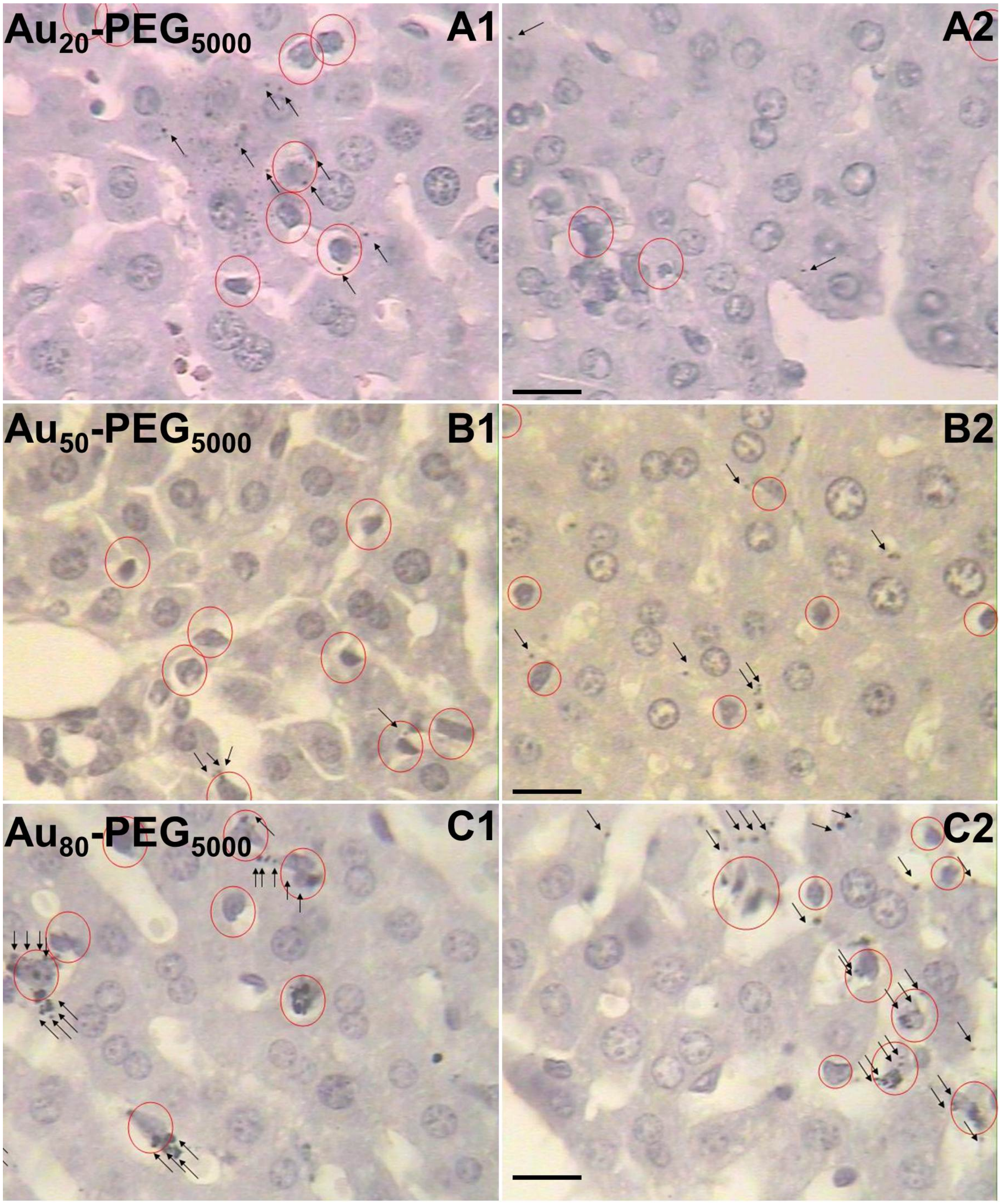

Figure 2.5: Intrahepatic tissue level distribution of Au$_x$-PEG$_{5000}$ NPs. Phagocytosis is positively correlated with particle size. (A) Au$_{20}$-PEG$_{5000}$ NPs; (B) Au$_{50}$-PEG$_{5000}$ NPs; (C) Au$_{80}$-PEG$_{5000}$ NPs. Black arrows indicate Au$_x$-PEG$_{5000}$ NPs deposited with silver. Red circles indicate Kupffer cells (KCs). Scale bar = 10 µm.

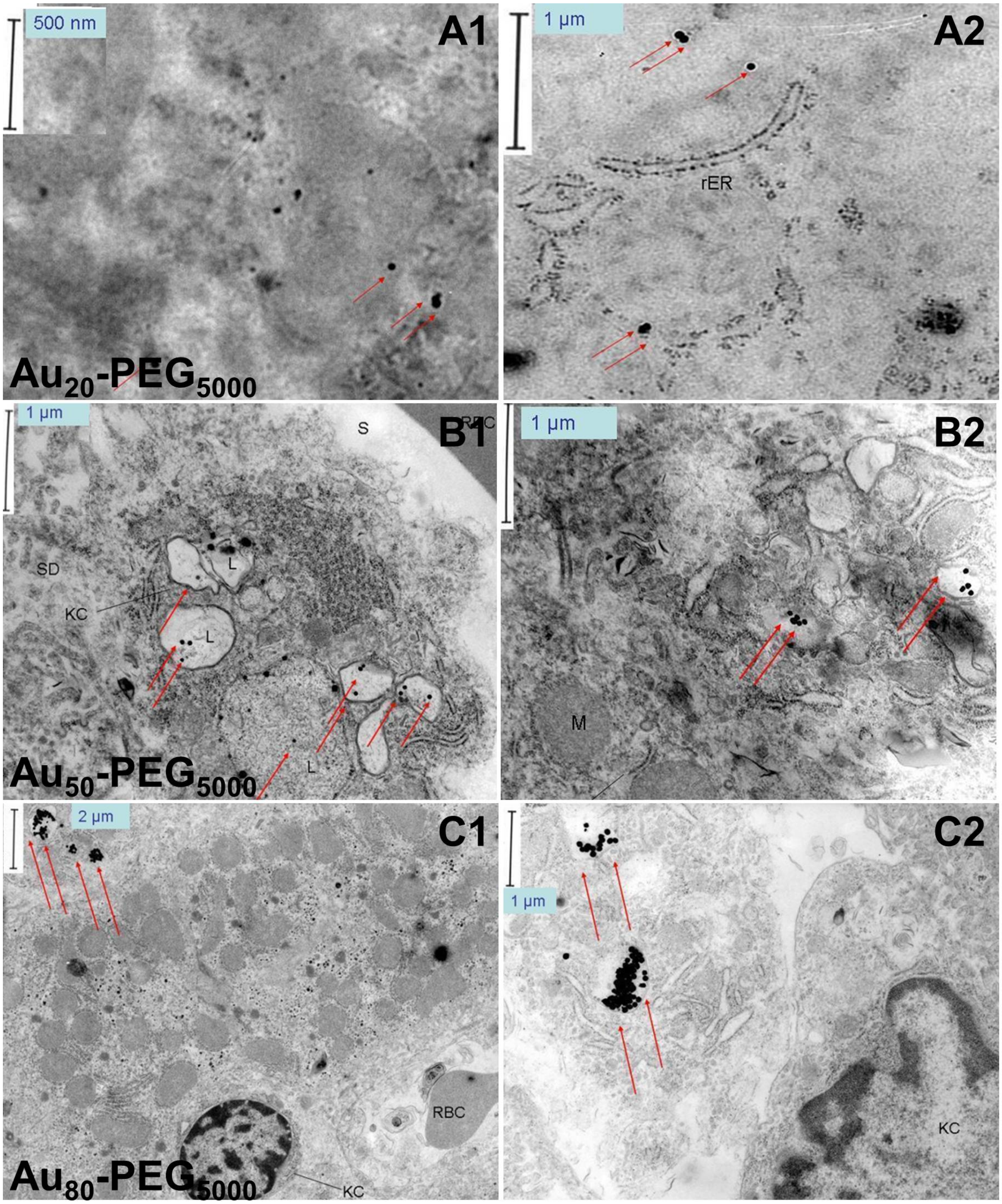

Figure 2.6: Intrahepatic cellular level distribution of Au$_x$-PEG$_{5000}$ NPs. Phagocytosis is positively correlated with particle size. (A) Au$_{20}$-PEG$_{5000}$ NPs; (B) Au$_{50}$-PEG$_{5000}$ NPs; (C) Au$_{80}$-PEG$_{5000}$ NPs. Red arrows point to actual Au$_x$-PEG$_{5000}$ NPs. Legend: RBC = red blood cells; S = sinusoidal space; L = lyzozymes; M = mitochondrion.

	H	KC	OC	KC/(H+OC)
Au_{20}-PEG_{5000}	0.14	1.44	0.38	2.77
Au_{50}-PEG_{5000}	1.45	29.11	2.35	7.76
Au_{80}-PEG_{5000}	3.59	142.16	3.40	17.79

Table 2.3: Areal density of Au_x-PEG_{5000} NPs inside the liver (# particles/mm^2). Legend: H = hepatocytes; KC = Kupffer cells; OC = other cell types. Examples of “other cell types” include, but not limited to, endothelial cells, sinusoids, erythrocytes, and lymph vessels.

is the perisinusoidal space interposed between the endothelium of the sinusoid and hepatocytes (not shown). Fig. 2.6B2 shows the hepatocytes in close proximity to KCs, as seen by the dense network of mitochondria, endoplasmic reticulum, and free ribosomes. These subcellular features are indicative of heavy hepatic metabolic activities in hepatocytes. Although not physically located within the KC, the Au_{50}-PEG_{5000} NPs were still entrapped inside lyzosomes as a direct consequence of phagocytosis. The Au_{80}-PEG_{5000} NPs led to the highest level of phagocytic response, with large particle clusters (∼10-30 particles per cluster) congregated near or within a KC (Fig. 2.6C1-2). Following the increase in particle size, higher densities of gold particles, if not already phagocytosed, localized in shorter distances away from the KCs.

Despite the high particle density in these clusters, the same electron micrograph shows that all PEGylated particles remained as individual entities even in the confined geometry of lyzosomes in KCs or hepatocytes, implying steric stability conferred by PEGylation to the Au_x-PEG_y NPs. Fig. 2.5C4 offers a close-up view of the particles encapsulated inside a lyzosome within a KC.

Renal distribution

Therapeutic nanoparticles, once injected into the bloodstream, must eventually exit the body to minimize toxicity due to their prolonged residency. Their individual components (drug payload and delivery vehicle) are small enough to pass through the kidney tubules and depart the body via urine excretion (a process known as “renal filtration” [123]). Whereas inulin the polysaccharides (hydrodynamic diameter = 3 nm) can completely filter through to urine with a whole-body $t_{1/2}$

of 1.9 h [124], only 9% of the Fab' antibody fragment can be renally filtered with a while-body $t_{1/2}$ of 4 h [125] [126]. In contrast, IgG, with a hydrodynamic diameter of 11 nm, has a much longer $t_{1/2}$ of 730 h with less than 0.1 urine/blood filterability [127] [126].

Au_x-PEG_{5000} NPs are non-decomposable objects. Given their hydrodynamic size ($\geq$ 40 nm), they should remain in blood circulation for a prolonged time and not experience renal clearance via urine excretion. It is of interest to see their accumulation patterns in the kidney, because particles can still freely access the tissue regions adjacent to the "renal filtration" apparatus from the bloodstream. The in vivo distribution patterns may reveal insights for the in vivo fater of intact polymeric or lipophilic therapeutic nanoparticles prior to their disassembly.

At the tissue level, Au_x-PEG_{5000} NPs display size-dependent accumulation in the kidney. Au_{50}-PEG_{5000} NPs demonstrated the highest areal density in the renal corpuscles (Fig. 2.7B1-2), whereas Au_{20}-PEG_{5000} and Au_{80}-PEG_{5000} NPs were found in minute quantities throughout the kidney in both medullary tubules and cortical renal corpuscles (Fig. 2.7A,C1-2). Stereological estimates also support these observations (Table 2.4), highlighting the superior ability of Au_{50}-PEG_{5000} to localize in renal corpuscles compared to other particle sizes.

TEM provides more morphological information to ascertain the in vivo particle distribution of the kidney at the cellular level. Consistent with stereological estimates, TEM images reflect the general dearth of Au_x-PEG_{5000} NPs in proximal tubule cells (Fig. 2.8B-C2). A tiny portion of the Au_{20}-PEG_{5000} NPs became clogged up in the renal tubules (Fig. 2.7A3) or were found near the mitochondria of tubule cells (Fig. 2.8A2). Such particles are too large to be pass through the renal filtration apparatus (with a size cutoff of 5-10 nm). At very rare instances, Au_{50}-PEG_{5000} NPs localized near vesicles adjacent to the basal laminar of a proximal tubule cell (Fig. 2.8B2). In brief, particle accumulation in renal tubules was an infrequent occurrence.

At this point, the reasons for the high retention of Au_{50}-PEG_{5000} NPs in the renal corpuscles remain unclear. TEM can provide additional ultrastructural details to address this issue. Inside

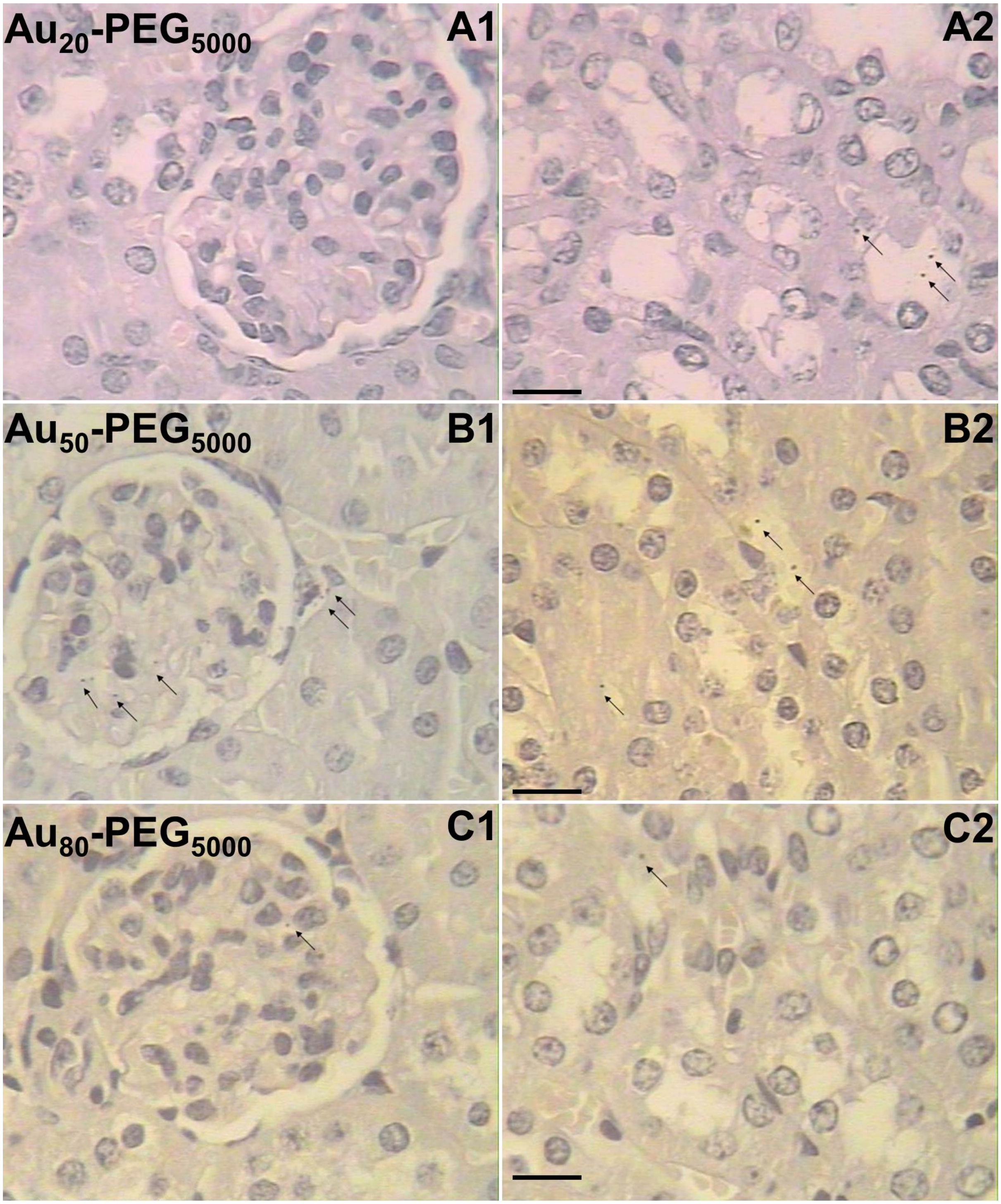

Figure 2.7: Intrarenal tissue level distribution of Au_x-PEG_{5000} NPs. Au_{50}-PEG_{5000} NPs resulted in the maximal deposition in renal corpuscles among all particle sizes. (A) Au_{20}-PEG_{5000} NPs; (B) Au_{50}-PEG_{5000} NPs; (C) Au_{80}-PEG_{5000} NPs. Column 1: Renal corpuscles; Column 2: Renal tubules. Black arrows indicate Au_x-PEG_{5000} NPs deposited with silver. Scale bar = 10 µm.

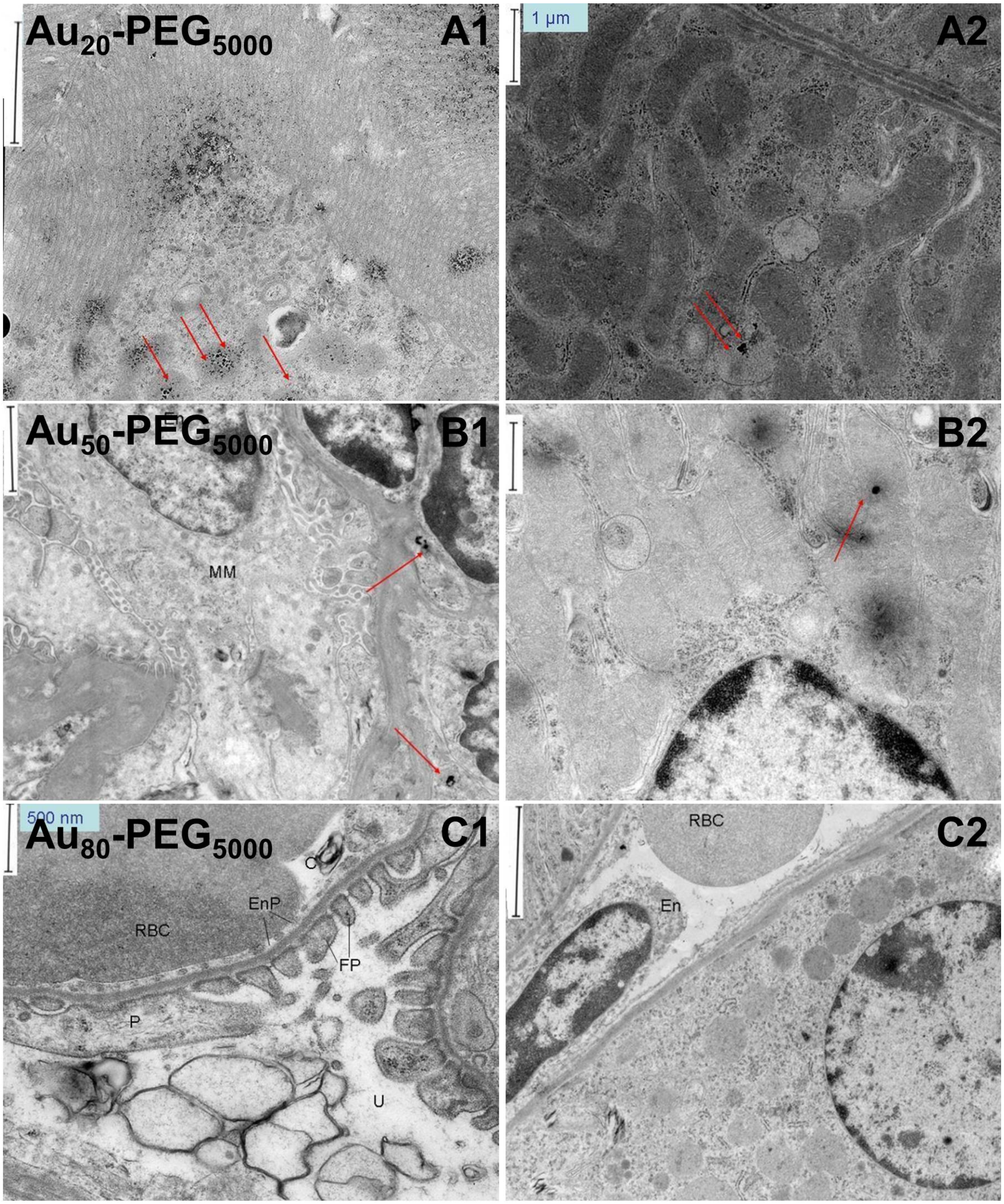

Figure 2.8: Intrarenal cellular level distribution of Au$_x$-PEG$_{5000}$ NPs. Au$_{50}$-PEG$_{5000}$ NPs resulted in the maximal deposition in renal corpuscles among all particle sizes. (A) Au$_{20}$-PEG$_{5000}$ NPs; (B) Au$_{50}$-PEG$_{5000}$ NPs; (C) Au$_{80}$-PEG$_{5000}$ NPs. Column 1: Renal corpuscles; Column 2: Renal tubules. Red arrows point to actual Au$_x$-PEG$_{5000}$ NPs. Legend: RBC = red blood cell; MM = mesangial matrix; FP = foot processes; U = urinary space; P = podocytes; En = endothelial cells.

	RC	T	O	RC/(T+O)
Au_{20}-PEG_{5000}	0.35	0.75	0.17	0.38
Au_{50}-PEG_{5000}	12.88	4.68	3.11	1.66
Au_{80}-PEG_{5000}	2.29	2.24	1.23	0.66

Table 2.4: Areal density of Au_x-PEG_{5000} NPs inside the kidney (# particles/mm^2). Legend: RC = renal corpuscles; T = assorted renal tubules (e.g., proximal convoluted tubules, distal convoluted tubules, collecting tubules); O = other tissues (e.g., blood vessels, endothelial cells).

the renal corpuscles, immersed in a mesh of matrix are mesangial cells, phagocytic cells that can remove trapped residues and aggregated proteins from the basal lamina [128]. For our present system, Au_{50}-PEG_{5000} NPs were entrapped by these mesangial cells (Fig. 2.8B1).

For Au_x-PEG_{5000} NPs in the renal bloodstream to come into contact with these mesangial cells, they need to first exit the blood capillaries (known as glomerular tufts) through their porous endothelial membrane. Incidentally, this membrane separates the mesangium matrix (where mesangial cells lie) from the glomerular capillary bloodstream. Thus, Au_x-PEG_{5000} NPs must be sufficiently small to penetrate through these pores of the glomerular membranes into the mesangium. Based on TEM measurements, such fenestrations have pore widths spanning from 71.4 to 95.2 nm (Fig. 2.8C1). The mean diameter cutoff is **83.3 nm**. The gap between foot processes of podocytes is 59.5 nm by inspection (measured at the mean-height of the foot processes), in good agreement with previously reported values [129] [130] [131]. These size estimates support the notion that Au_{50}-PEG_{5000} NPs (or smaller) are sufficiently small to pass through the pores and enter the mesangium.

2.4 Conclusion

There is ever increasing research momentum to apply nanotechnology on the diagnosis and treatment of cancer. On the treatment front, the safe, substained, and targeted delivery of nanoparticle-based therapeutic and contrast agents to tissue and cellular destinations (e.g, cancer cells within the tumor) are recurrent objectives for creating more efficacious cancer therapies.

This chapter seeks to optimize the delivery of submicron-sized nanoparticles used for cancer applications. To generate a viable strategy to maximize tumor targeting, mechanistic understanding in the effect of each design parameter (e.g, particle size, surface charge, polymer coating) on the in vivo behavior of nanoparticles (e.g., pharmacokinetics, distribution, toxicity) is crucial. Here, we investigate the effect of particle size on the in vivo distribution in mice bearing solid tumors, using PEGylated gold nanoparticles as model probes.

All gold nanoparticles contain of PEG_{5000} chains on their periphery, and are stable against salt-induced aggregation at physiological conditions. Changes in hydrodynamic size and ζ-potential of the particles before and after PEGylation match reasonably well with theoretical predictions. The PEG chain length of 5000 represent a careful balance between circulation time and diffusion. Particles coated with shorter PEGs may experience rapid binding by serum proteins and subsequent clearance by macrophages, failing to reach to the tumor in adequate amounts despite the EPR effect. Longer PEG coatings can prevent premature clearance by opsonization, but can add tremendous hydrodynamic drag to the nanoparticle in the tumor interstitium en route to its traversal to cancer cells within the tumor.

Passive tumor targeting

Au_x-PEG_{5000} NPs do not contain any targeting ligands, but still reached the tumor after 24 h after their i.v. injection due to the EPR effect. From results given in Chapter 3, a threshold targeting ligand content is necessary for nanoparticles in the tumor interstitium to enter cancerous cells. Thus, passively targeted Au_x-PEG_{5000} NPs predominantly accumulated in the tumor interstitium and in the vicinity of leukocytes, and only entered Neuro2A cells at infrequent instances, independent of particle size. The only exception is the smallest particles (Au_{20}-PEG_{5000} NPs), which localized inside vesicles within Neuro2A cells. This is consistent with observations made by Perrault et al. [132], who reported two size-dependent migration patterns of Au_x-PEG_y NPs inside the tumor. 24 h after dosing, Au_{16}-PEG_{2000} moved further away from blood vessels and accumulated in intracellular regions more frequently, when compared to their larger counterparts, Au_{33}-PEG_{5000} and Au_{84}-PEG_{10000} NPs. Moreover, based on pharmacokinetics measurements on submicron-sized Au_x-PEG_y NPs (see Chapter 4), larger particles have shorter blood circulation times than smaller particles. Thus, passive targeting is optimal when using nanoparticles smaller than 100 nm, for their deeper tumor penetration and longer circulation in blood.

Avoidance of RES clearance

Targeted delivery to biological destinations also requires the minimization of premature clearance. The RES can serve as immunological barriers to the effective tumor targeting, with macrophages or monocytes sequestering injected nanoparticles. Kupffer cells (KCs) are an important RES cell type responsible for nanoparticle clearance. Tissue and cellular level data from this chapter show that KCs engulfed Au_x-PEG_{5000} NPs in a size-dependent fashion. These data agree with the in vivo distribiution at the organ level, characterized by positive correlation between bulk nanoparticle uptake by the RES organs (liver and spleen) and particle size (see Chapter 4). Ogawara et al. [133] reported biodistribution data of polystyrene microspheres of 50 and 500 nm in the liver. 59% of the 50 nm particles reached KCs, whereas 71% of the 500 nm particles arrived at KCs. Bogers et al. [134] discovered an elevated clearance for larger IgA polymers or aggregates compared to monomeric IgA, and showed the association of IgA (hydrodynamic size $\sim$ 11.36 nm) to KCs and encapsulation of IgA within vesicles in KCs. The degree of phagocytic response then translates into the speed of clearance. Sadauskas et al. [135] reported tremendous phagocytic activity at KCs even for 2 and 40 nm AuNPs, injected i.v. at similar concentrations to mice, although their AuNPs were not PEGylated to prevent salt-induced aggregation. Taking our data and existing literature into cosideration, the avoidance of RES clearance by KCs sets an upper limit of 100 nm for the nanoparticle size to optimize tumor targeting.

Renal accumulation

Unlike the tumor and liver, few studies in the nanomedicine field have reported submicron-sized particle accumulation in the kidney following an i.v. injection, because the kidney is regarded merely as a blood filtration organ that removes excess salts and metabolic wastes in the form of urine. Here, we observe size-dependent accumulation of Au_x-PEG_{5000} NPs in the kidney, in which Au_{50}-PEG_{5000} and Au_{80}-PEG_{5000} NPs resided within renal corpuscles in more appreciable amounts than Au_{20}-PEG_{5000} NPs. Foglieni et al. [136] reported the retention of locally injected lipopolyplexes (diameter $\sim$ 160 nm) in the renal corpuscles but not polyplexes (diameter $\sim$ 93 nm), suggesting the presence of a filtration mechanism that retains nanoparticles of 100 ± 25 nm in size within renal corpuscles (to be explained in Chapter 4).

In summary, passive targeting and avoidance of RES clearance dictate that the particle size for optimal tumor delivery should not exceed 100 nm. Armed with these results, the next step is to promote the engagement of nanoparticles accumulated in the tumor interstitium to cancerous cells in the tumor. In Chapter 3, we will explore the ability of Au_{50}-PEG_{5000} NPs (size $\sim$ 70 nm) to internalize into cancerous cells via the surface attachment of targeting ligands (active targeting). Based on the kidney imaging data, an inevitable consequence of delivering Au_{50}-PEG_{5000} NPs (with targeting ligands attached) to tumor bearing mice is their accumulation within renal corpuscles in the kidney.

2.5 Supporting Information

In Greek, “stereo” means “a geometric object.” Stereology recreates or estimates the geometrical properties of objects. Here, we employ basic stereology to semi-quantitatively describe the distribution of Au_x-PEG_{5000} NPs in different tissue compartments of the kidney, liver, and tumor. Stereology consists of two major components, “sampling” and “measuring.”

Sampling

While a larger number of sections are desired to achieve statistical significance, time is often insufficient to examine each section in detail. The generation of "representative samples" is imperative. A sample is representative if all components possess the same probability to contribute to the sample. Random sampling can satisfy this requirement. By the "Law of large numbers," the average of a large number of estimates will converge to the true value of the mean estimate.

While random sampling guarantees an equal probability of each segment of the section to be captured, it does not preclude the likelihood of repeated sampling of the same segment. One can employ "uniform random sampling" (URS) in which one chooses a random starting point on the section and obtains all subsequent samples at a fixed interval. While the random starting point ensures equal representation, the fixed intervals avoid the occurrence of "clustered sampling."

Measuring

Simple counting methods can effectively reproduce the spatial relationships of particles. This study focuses on the two-dimensional (areal density) distribution, but the method outlined below is open for extension to obtain three-dimensional measurements (volume density) by taking the section thickness into account. This is a direct application of the "Cavalieri Principle," and is similar to counting a population of cells using a hemacytometer.

The calculation of the areal density begins with the construction of a rectangular grid. One then places points at each of the intersections of the grid lines and associates one of the rectangular areas formed by the grid with each point. The association of one area with a point located at each intersection allows the coverage of the entire area of the grid.

With the uniformly representative images, the next step is to introduce approximate boundaries to establish functional or morphological compartments in tissues captured by these images. The experimental objectives in question will dictate the exact nature of these compartments.

Hypothesis I: Particle injection triggers immune responses, leading to engulment by cells of the self-defense apparatus (e.g., Kupffer cells and leukocytes). (**Liver**: *1. Hepatocytes*; *2. Kupffer cells*; *3. Endothelial cells, erythrocytes*; **Tumor**: *1. Leukocytes*; *2. Cancerous Cells*)

Hypothesis II: Size affects the particle distribution in the kidney, a natural blood filter (**Kidney**: *1. Glomerulus*; *2. Renal tubules*; *3. Blood vessels and endothelial cells*).

2.6 Materials and Methods

Assembly of Au_x-PEG_{5000} NPs

Methoxy-PEG_{5000}-thiol (Laysan Bio.), dissolved in deionized water, was added to 3 mL of aqueous suspension of unconjugated gold colloids (Ted Pella) of a designated core size (20, 50, 80, 100, and 150 nm) at an excess concentration of $\sim$9 PEG strands per nm^2 of gold surface. e.g. To ensure complete coverage, PEGylation of Au_{50} NPs required the addition of 10 µL of 1 mM mPEG$_{5000}$-thiol (in deionized water) to 0.5 mL of aqueous suspension of 2.25×10^{10} particles. All PEGylation reactions proceeded at RT for 30 min with constant stirring. To remove any unbound PEG_{5000}, the reaction mixture was dialyzed against deionized water using a 30 kDa Amicon MWCO membrane (Millipore) for three times.

Tumor formation and systemic delivery

Neuro2A cells were cultured in complete growth medium (DMEM supplemented with 10% FBS, 100 units/mL penicillin, and 100 units/mL streptomycin). In the right hind flank, A/J mice (Jackson Laboratory) received subcutaneous implantation of Neuro2A cells (at 10^6 cells per mouse per 0.1 mL of DMEM). Before injection, tumors reached 100-200 mm^3 in size, as determined by caliper measurements ($0.5 \times l \times w^2$). For each particle size (x = 20, 50, and 80 nm), three A/J mice received i.v. administration of Au_x-PEG_{5000} NPs at a concentration of 4.5 $\times 10^{11}$ particles per animal (formulated in 0.1 mL of D5W) via the tail vein. Animal sacrifice by CO_2 overdose took place 24 h after injection to collect the tumor, liver, and kidney.

Stereological sampling

Observed with a 100× objective under a light microscope, each silver-enhanced tissue slide was shifted laterally and across the entire sample by the same distance to obtain uniformly random photographs, captured by a built-in digital camera connected to the light microscope. The same camera, also connected to a computer monitor, enabled the visual inspection required to ensure a consistent degree of a lateral shift from one point on the tissue slide to another. This collection scheme yielded a total of 456 light microscopic images for later quantification of the in vivo biodistribution of Au_x-PEG_{5000} NPs.

Stereological measuring

Depending on the tissue, each light microscopic image was visually inspected to see whether the compartmentalization scheme could be applied. If so, an arbitrary border was drawn to decompose the image into multiple compartments. Otherwise, the entire tissue was taken as a single compartment.

In each microscopic image, for each particle size i and each tissue compartment j, the number of Au_x-PEG_{5000} NPs was counted as n_{ij}. Meanwhile, the area of this tissue compartment, a_{ij}, was recorded. The same procedure was repeated for all m_{ij} microscopic images that captured the particles of the same dimension i in the same tissue compartment j. Such a counting exercise enabled the calculation of the sum of particles of a certain dimension, i, residing in a certain tissue compartment, j, denoted as N_{ij}. Likewise, it also yielded the sum of area of a certain tissue compartment j that contained particles of dimension i, A_{ij}. The normalization of N_{ij} by A_{ij} led to Π_{ij}, the **areal density** of particles of the dimension i per unit area of the tissue compartment j.

$$\Pi_{ij} \equiv \frac{N_{ij}}{A_{ij}} \equiv \frac{\sum^{m_{ij}} n_{ij}}{\sum^{m_{ij}} a_{ij}}$$

Chapter 3

Mechanism of Active Targeting in Solid Tumors with Transferrin Containing Gold Nanoparticles

3.1 Abstract

PEGylated gold nanoparticles are decorated with various amounts of human transferrin (Tf) to give a series of Tf-targeted particles with near-constant size and ζ-potential. The effects of Tf content on nanoparticle tumor targeting are investigated in mice bearing subcutaneous Neuro2A tumors. Quantitative biodistributions of the nanoparticles 24 hours after tail vein, intravenous (i.v.) injections show that the nanoparticle accumulations in the tumors and other organs are independent of Tf. However, the nanoparticle localizations within a particular organ are influenced by the Tf content. In tumor tissue, the content of targeting ligands significantly influences the number of nanoparticles localized within the cancer cells. In liver tissue, high Tf content leads to small amounts of the nanoparticles residing in hepatocytes, while most nanoparticles remain in non-parenchymal cells. These results suggest that targeted nanoparticles can provide greater intracellular delivery of therapeutic agents to the cancer cells within solid tumors than their non-targeted analogs. A competitive binding model from classical kinetics,

---

Excerpts of this chapter are reproduced with permission from "Mechanism of active targeting in solid tumors with transferrin containing gold nanoparticles." Chung Hang J. Choi, Christopher A. Alabi, Paul Webster, and Mark E. Davis. *Proc. Natl. Acad. Sci. USA*. **107**, 3, 1235-1240 (2010).

when used in conjunction with in vitro binding studies, provides extra insights to the mechanism of multivalent ligand-receptor interactions.

3.2 Introduction

Targeted nanoparticle delivery of therapeutic molecules has the potential to provide safer and more effective therapies for cancer applications [137]. Recent work has focused on understanding the parameters that influence targeted nanoparticle behavior and the development of design rules for creating nanoparticle-based therapeutics and imaging agents. Passive tumor targeting takes advantage of the irregularity and leakiness of tumor vasculature to allow nanoparticle accumulation in the tumor (due to the enhanced permeability and retention (EPR) effect [104] [138]). Active targeting exploits the overexpression of surface receptors on cancer cells by providing targeting ligands that can engage these receptors.

Active targeting

Previous studies on active targeting have utilized an assortment of ligands ranging from proteins (antibodies [139] and their molecular fragments [140]), nucleic acids (aptamers [141]) and small molecules (vitamins [142], peptides [143], or carbohydrates [144]). Ligand incorporation facilitates the entry of nanoparticles to cancer cells via receptor-mediated endocytosis, after which they can release their drug payloads to provide a therapeutic action. Perrault et al. convincingly illustrated that PEGylated gold nanoparticles require sizes below 100 nm in diameter for movement away from the vasculature and throughout the tumor [132]. This is a necessary condition for engaging cancer cell surface receptors and attacking molecular targets within cancer cells. Park et al. showed that antibody-targeted liposomes revealed enhanced anti-tumor effects over their untargeted counterparts [99]. The same investigators later concluded that the antibody targeting does not increase tumor accumulation of liposomes over untargeted controls but rather elevates particle localization within cancer cells [145]. Using multimodal in vivo imaging techniques, Bartlett et al. demonstrated that untargeted and transferrin-targeted polymeric nanoparticles containing siRNA have the same whole body distribution (and kinetics) and tumor accumulation, but the targeted particles lead to more pronounced gene inhibition within cancer cells [146]. Very recently, with the aid of computer simulations, Schmidt and Wittrup predicted similar tumor uptake of both targeted and untargeted liposomes of ~50 nm in size [147].

From the above examples, the targeting ligand does not influence organ distribution, e.g., bulk tumor localization, but rather tissue distribution, i.e., cancer cells versus non-cancer cells (such as leukocytes and blood endothelial cells) within the tumor. These findings suggest that active targeting of nanoparticles occurs via a different mechanism than individual targeting ligands, e.g., antibodies. Thus, further examination of active targeting with nanoparticles is merited.

We prepared a series of gold nanoparticles with transferrin contents spanning two orders of magnitude for comparison to untargeted particles, in order to test the mechanistic effects of the active targeting of nanoparticles in solid tumors, as well as to delineate particle distribution patterns due to ligand targeting at the cellular level, a level not investigated in previous organ and tissue distribution studies.

Transferrin as a targeting ligand

Human holo-transferrin (Tf) is the targeting ligand used here to probe the effects of active targeting. Because of rapid cell division and stringent demand for iron (for heme synthesis), many cancer cell types have abundant expression of transferrin receptors (TfRs) [148]. Tf is a 79 kDa endogenous glycoprotein that binds to TfRs at extracellular pH (K_d = 1-100 nM [149] [150]) and trigger receptor-mediated endocytosis [151].

Tf has a history of use as a targeting agent for cancer cells. For example, Tf-targeted, siRNA-containing nanoparticles give pronounced inhibition of tumor growth in metastatic Ewing's sar-

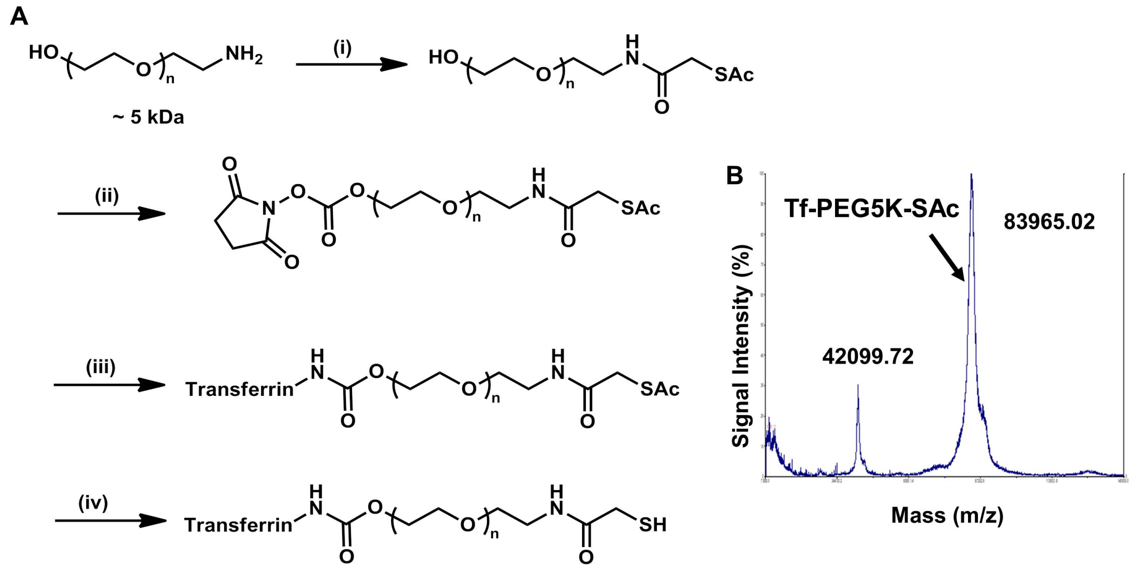

Figure 3.1: Synthesis of Tf-PEG$_{5000}$-SAc. (A) Reaction conditions: (i) SATA, 4 h, DMF, RT. (ii) DSC, DMF/dioxane, 4 h, RT. (iii) Holo-Tf, 2 h, RT, 50 mM sodium phosphate, pH = 7.4 (iv) hydroxylamine, 2 h, RT, 50 mM sodium phosphate, 25 mM EDTA, pH = 7.5. Step (iv) renders free -SH groups for conjugation onto AuNPs to form Au$_{50}$-PEG$_{5000}$-Tf$_x$ NPs. (B) The sharp peak of the MALDI-TOF spectrum at 84 kDa confirms the identity of the expected product, mono-PEGylated Tf (Tf-PEG$_{5000}$-SAc).

coma, whereas their untargeted counterparts do not [152]. The covalent conjugation of Tf onto PEG-AuNPs at varying amounts to form transferrin-targeted, PEGylated gold nanoparticles (Au$_{50}$-PEG$_{5000}$-Tf$_x$ NPs) and the i.v. injection of these particles into mice bearing subcutaneous Neuro2A tumors provide the model system to investigate the effects of targeting ligand content on in vivo particle distribution on organ, tissue, and cellular levels.

3.3 Results and Discussion

Synthesis and characterization of Tf-PEG$_{5000}$-SAc

Fig. 3.1 illustrates the synthesis scheme for Tf-PEG$_{5000}$-SAc, a PEG conjugate (MW: 5000) that contains the targeting ligand (Tf) and an acetyl-protected sulfur group (SAc). This conjugate decorates the surface of the gold nanoparticles to extend Tf away from the gold surface to the nanoparticle periphery, as well as to facilitate the engagement of Tf with surface TfRs of cancer cells within the tumor. Purification of the crude reaction mixture using hydrophobic interaction

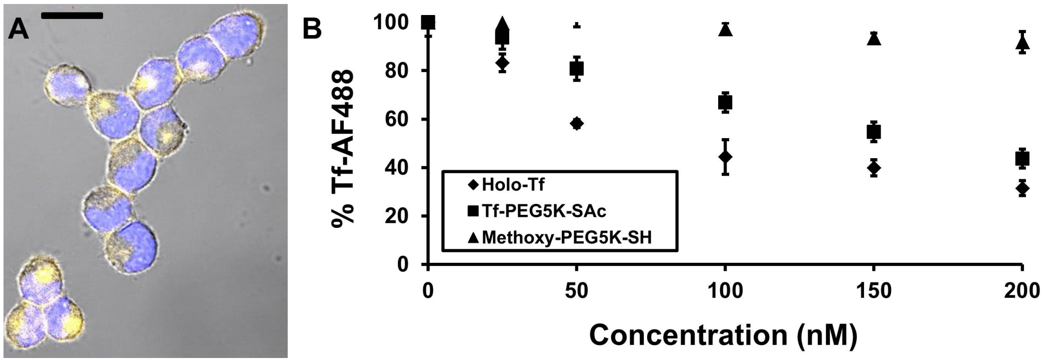

Figure 3.2: (A) A confocal micrograph shows the surface and internalized TfRs of Neuro2A cells stained by antiTfR-AF555 (orange), counter-stained by DAPI (blue) (Scale bar = 20 µm). (B) Competitive binding assay. PEGylation to form Tf-PEG$_{5000}$-SAc did not drastically reduce the binding affinity of Tf. Reported data are expressed as percent of fluorescence of cells incubated with only Tf-AF488.

chromatography (HIC) gave pure, mono-PEGylated, Tf-PEG$_{5000}$-SAc, with an apparent molecular weight of 84 kDa. This PEGylation method is not site specific on the Tf, so excessive protein PEGylation may block the active sites of Tf for binding to TfRs. Therefore, we used here only the mono-PEGylated fraction for nanoparticle assembly.

The competitive binding of Tf-PEG$_{5000}$-SAc against fluorescently tagged Tf (Tf-AF488) was used to estimate the effects of mono-PEGylation on Tf binding affinity (Fig. 3.2), with holo-transferrin (holo-Tf) and mPEG-SH (methoxy-PEG-thiol; MW: 5000) as positive and negative controls. A 1:1 ratio of Tf-AF488 to free holo-Tf gives ~45% reduction in fluorescence, implying almost equal binding affinity of Tf-AF488 and free holo-Tf. Tf-PEG$_{5000}$-SAc shows reduction in fluorescence following the escalation in Tf-PEG$_{5000}$-SAc concentration, although the magnitude is less than that of free holo-Tf. A 1:1 ratio of Tf-AF488 to Tf-PEG$_{5000}$-SAc gives ~20% decline in fluorescence. Thus, mono-PEGylation does alter the affinity of Tf to TfRs on Neuro2A cells, but not to a large extent.

Furthermore, a saturation binding experiment of Tf-AF488 to TfRs of Neuro2A cells was used to measure the affinity of Tf-PEG$_{5000}$-SAc (Fig. 3.3). A Scatchard analysis of these data yields a K_d for Tf-AF488 of 64 nM, and hence a K_d of 64 nM for free holo-Tf (based on the competitive binding study). The estimated K_d for Tf-PEG$_{5000}$-SAc is 144 nM, because Tf-PEG$_{5000}$-SAc

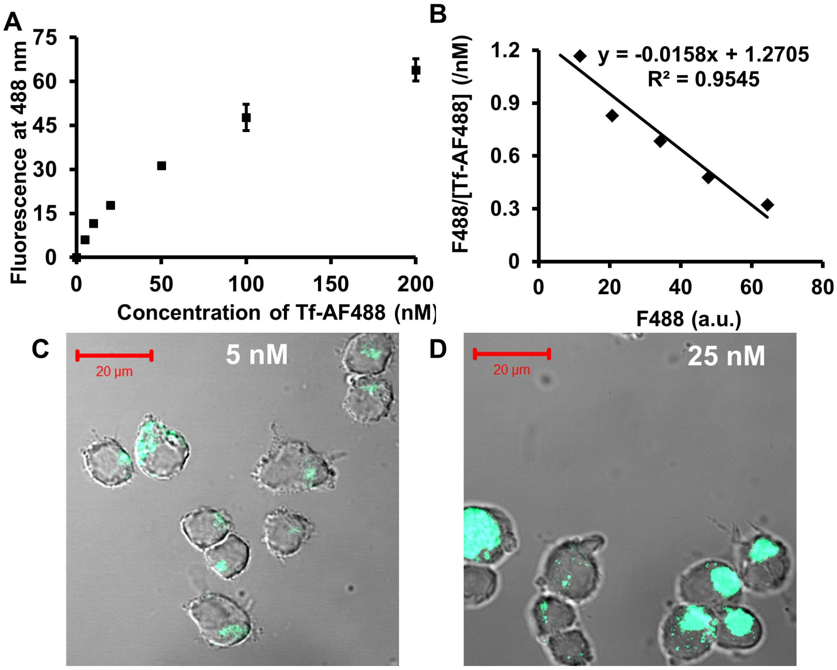

Figure 3.3: (A) Saturation binding of Tf-AF488 to Neuro2A cells. Error bars represent one s.d. from duplicate experiments. (B) The slope of a Scatchard plot gives the inverse of the binding dissociation constant, K_d^{-1}. Linear regression gives $K_d^{-1} = 0.0157$ nM^{-1}, and K_d (Tf-AF488) = 64 nM. K_d (Tf) $\sim K_d$ (Tf-AF488) = 64 nM. Confocal micrographs show the dose-dependent binding and internalization of free Tf-AF488 ligands (green) into Neuro2A cells at (C) 5 nM and (D) 25 nM. Scale bar = 20 µm.

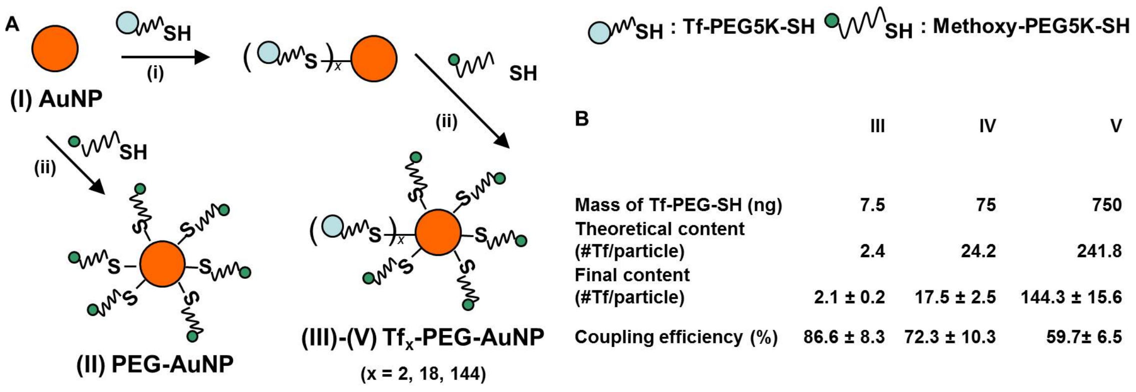

	III	IV	V
Mass of Tf-PEG-SH (ng)	7.5	75	750
Theoretical content (#Tf/particle)	2.4	24.2	241.8
Final content (#Tf/particle)	2.1 ± 0.2	17.5 ± 2.5	144.3 ± 15.6
Coupling efficiency (%)	86.6 ± 8.3	72.3 ± 10.3	59.7± 6.5

Figure 3.4: (A) Assembly scheme of Au_{50}-PEG_{5000}-Tf_x NPs. Unmodified 50nm AuNPs (**I**) were either reacted with excess $mPEG_{5000}$-SH to form Au_{50}-PEG_{5000} NPs (**II**) as untargeted particles, or first reacted with various amounts of Tf-PEG_{5000}-SH and later excess mPEG-SH to form Au_{50}-PEG_{5000}-Tf_x NPs (**III**: 2 Tf/particle; **IV**: 18 Tf/particle; **V**: 144 Tf/particle). (B) Coupling efficiency of Au_{50}-PEG_{5000}-Tf_x NPs. This table presents estimates of Tf content of Au_{50}-PEG_{5000}-Tf_x NPs from the reaction of various amounts of Tf-PEG_{5000}-SH and 2.25×10^{10} unmodified 50 nm AuNPs in a 0.5 mL aqueous solution. The theoretical Tf content assumes perfect conjugation of Tf-PEG_{5000}-SH added to the reaction mixture. An ELISA assay was used to determine the amount of free Tf-PEG_{5000}-SH, which in turn was used to deduce the amount of Tf-PEG_{5000}-SH bound onto Au_{50} NPs (by assuming a perfect mass balance). A division of the final Tf content by the theoretical Tf content and multiplication by 100% gives the coupling efficiency.

displays a 2.25-fold less binding affinity to TfRs when compared to free holo-Tfs.

Synthesis and characterization of Au_{50}-PEG_{5000}-Tf_x NPs

The addition of Tf-PEG_{5000}-SH (deprotected Tf conjugate) into an aqueous suspension of 50 nm unmodified AuNPs (**I**) initiates the assembly of Au_{50}-PEG_{5000}-Tf_x NPs (Fig. 3.4A). We selected this gold particle size to mimic the size our siRNA-containing therapeutic nanoparticles (∼70 nm) [146] [152] and to achieve optimal receptor-mediated endocytosis in cells amidst other particle sizes in the 10-100 nm range [153]. Adjustment of ligand concentration during the assembly process gave targeted nanoparticles with Tf contents spanning two orders of magnitude (**III**: 2 Tf/particle; **IV**: 18 Tf/particle; and **V**: 144 Tf/particle), with a coupling efficiency that decreases with input Tf concentration from 87% (**III**) to 60% (**V**) (Fig. 3.4B). Complete PEGylation with excess mPEG-SH followed to mask any unreacted gold surface of the nanoparticles. PEGylated nanoparticles (**II**) were prepared for use as an untargeted control.

Table 3.1 lists the physicochemical properties of the nanoparticles. Hydrodynamic diameters of Au_{50}-PEG_{5000}-Tf_x NPs are near-constant in water and 1× PBS independent of Tf content (∼80 nm). Their ζ-potentials in 1 mM KCl are also the same and independent of Tf content (~-10 mV). With an isoelectric point of 5.9 [151], Tf is negatively charged in 1× PBS (pH = 7.4), but do not significantly change the overall particle ζ-potential. Thus, this set of nanoparticles is well-suited to ascertain the effects of targeting ligand content on nanoparticle distribution at relatively constant nanoparticle diameter and ζ-potential.

Stability and binding affinity of Au_{50}-PEG_{5000}-Tf_x NPs

Particle stability in physiological conditions is a prerequisite for effective active targeting. **I** aggregates rapidly in 1× PBS (Fig. 3.5). PEGylation imparts steric stability to **II**-**V** in salt solutions, as can be seen from their near constant hydrodynamic diameter (HD) when exposed to

NP	HD$_{water}$ (nm)	HD$_{PBS}$ (nm)	ZP (mV)	σ (#Tf/NP)
I	49.4 ± 0.6	755.4 ± 8.3	-18.3 ± 1.2	N/A
II	73.2 ± 1.3	74.9 ± 0.9	-10.9 ± 1.3	N/A
III	77.0 ± 0.9	77.7 ± 1.5	-10.8 ± 0.9	2.1 ± 0.2
IV	78.5 ± 1.7	81.3 ± 2.9	-9.0 ± 1.7	17.5 ± 2.5
V	81.0 ± 2.5	87.5 ± 3.4	-9.9 ± 1.7	144.3 ± 15.6

Table 3.1: Physicochemical properties of Au$_{50}$-PEG$_{5000}$-Tf$_x$ NPs. **I** = Unmodified Au$_{50}$ NP; **II** = Au$_{50}$-PEG$_{5000}$ NP; **III-V** = Tf-PEG$_{5000}$-Au$_{50}$ NP of 2, 18, and 144 Tf per particle, respectively. HD = hydrodynamic diameter; ZP = ζ-potential; σ = Tf content; N/A = not applicable. Reported data are reported as average ± s.d. from triplicates of experiments.

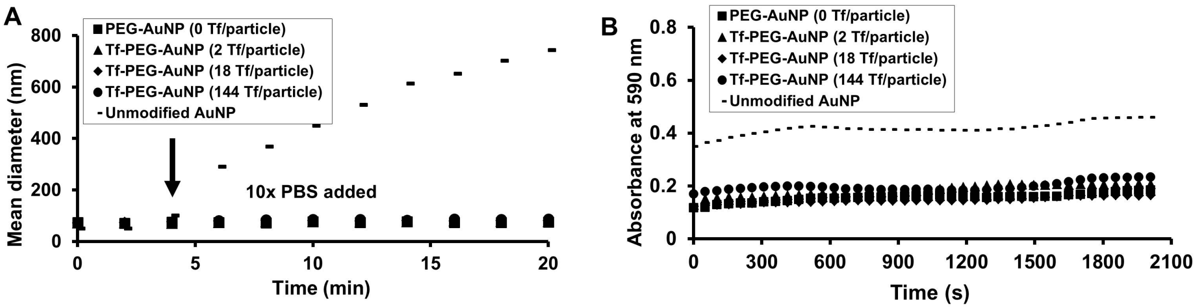

Figure 3.5: Particle stability. (A) In vitro stability against salt. **I** showed instant aggregation after the addition of 10× PBS at the 4th minute, yet **II-V** remained stable. (B) In vitro stability against serum. PEGylation attenuated particle aggregation in 90% mouse serum.

1× PBS. Moreover, **II-V** do not flocculate in 90% fresh mouse serum in 1× PBS. These results suggest that the PEGylated nanoparticles will not aggregate in vivo.

From the saturation binding experiment of Au$_{50}$-PEG$_{5000}$-Tf$_x$ NPs, **IV-V** bind to Neuro2A cells in a fashion that depends on both Tf content and nanoparticle concentration (Fig. 3.6), validating the successful conjugation of Tf-PEG$_{5000}$-SH onto the particle surface. A Scatchard analysis was used to estimate the K_d's of Au$_{50}$-PEG$_{5000}$-Tf$_x$ NPs, assuming a homogeneous distribution of Tf on the nanoparticle surface. The measured values of **IV** and **V** were 1.06 and 0.13 nM, respectively. If 21.33% of Tf on the particle surface are in actual contact with TfRs on the surface of Neuro2A cells due to geometric scaling arguments (see Supporting Information), the resultant K_d's of **IV** and **V** are 0.23 and 0.03 nM, respectively, representing approximately 600-fold and 4800-fold enhancement in binding affinity, respectively, compared to free Tf-PEG$_{5000}$-SAc (K_d = 144 nM). The magnitude of binding affinity enhancement also increases with the

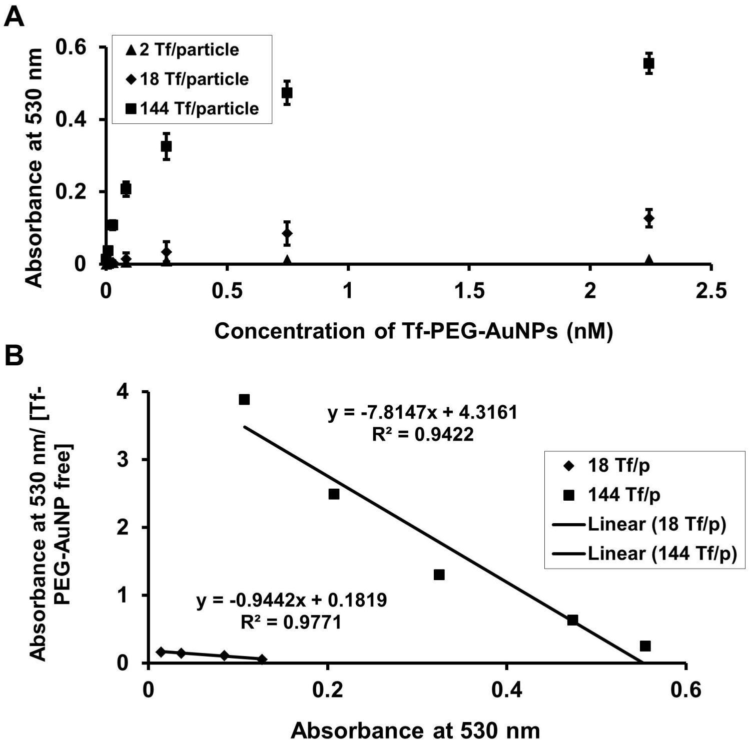

Figure 3.6: (A) Saturation binding of Au_{50}-PEG_{5000}-Tf_x NPs to Neuro2A cells. Au_{50}-PEG_{5000}-Tf_x NPs bound in a Tf content dependent manner (**III-V**). Error bars indicate one s.d. from duplicate experiments. (B) Scatchard plots yield a K_d of 1.06 and 0.13 nM for **IV** (left curve) and **V** (right curve), respectively. The Scatchard analysis assumes 100% contact of all Tfs mounted on the surface of PEG-AuNPs.

ligand content on the particle surface. Such enhancement underscores the "multivalent effect," when particle curvature permits a localized surface of multiple Tfs for simultaneous interactions with surface TfRs to trigger endocytosis. Furthermore, given the low binding affinity, the poor signal-to-noise ratio from the binding data of **III** does not warrant a meaningful estimation of the K_d for **III**. Provided such dilute Tf content (2 Tf per particle), in theory, the binding affinity of **III** should approach that of the monovalent ligand, Tf-PEG_{5000}-SAc ($K_d = 144$ nM).

In vivo tumor distribution of Au_{50}-PEG_{5000}-Tf_x NPs

Mice bearing subcutaneous Neuro2A tumors received i.v. administrations of **II-V** via the tail vein, and were sacrificed 24 hours later to collect organs for analyses. Despite the overexpression of surface TfRs by Neuro2A cells (Fig. 3.2), at the organ level, the tumor merely amasses 2-3%

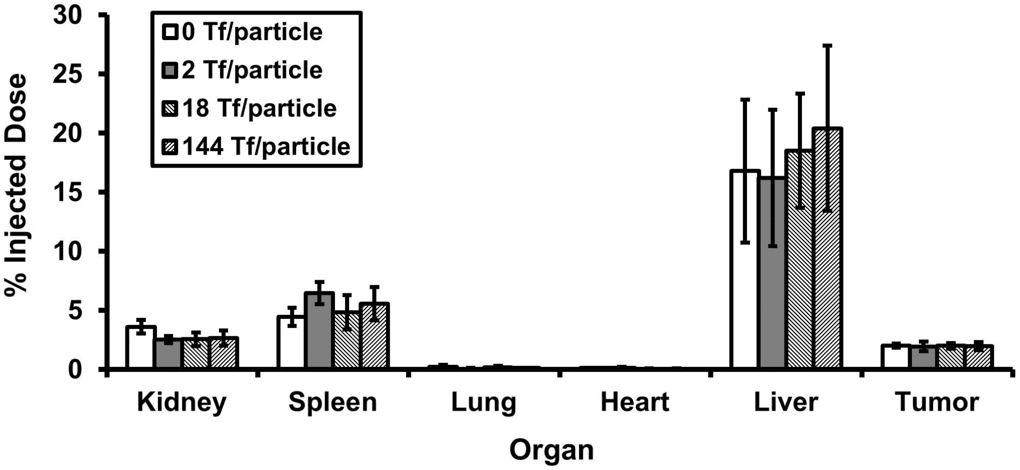

Figure 3.7: In vivo organ level distribution. Bulk particle localization in all organs was independent of Tf content. Gold contents are normalized to percent injected dose (% ID). Error bars indicate one s.d. from each class of Au_{50}-PEG_{5000}-Tf_x NP (N = 3).

ID of particles, independent of Tf content (Fig. 3.7).

At the tissue level, histological data reveals predominant localization of AuNPs in the vicinity of leukocytes for all Tf contents (Fig. 3.8A-B1). Intracellular accumulation of nanoparticles inside Neuro2A cells is rare (Fig. 3.8B-C1) at low Tf content (**II** - **IV**), but further increase in Tf content to 144 Tf per particle leads to considerable nanoparticle uptake by Neuro2A cells, as seen from isolated nanoparticles of **V** residing near Neuro2A cells (Fig. 3.8D1).

Electron microscopy reveals clear, Tf-content dependent, intracellular nanoparticle localization. While **II-IV** mostly localize inside leukocytes (Fig. 3.8A2) or externally touch the surface of Neuro2A cells (Fig. 3.8B-C2), clusters of **V** reside within large endocytic vesicles of Neuro2A cells (Fig. 3.8D2). The abundance of mitochondria and endoplasmic reticulum (essential for robust cellular metabolic activities) indicates nanoparticle localizations inside target Neuro2A cells but not other leukocytes, endothelial cells, or other non-cancer cells (Fig. 3.8D3). Thus, ligand content does not alter the extent of bulk, nanoparticle content in the tumor. Instead, it biases the tissue and cellular distribution with increasing targeting ligand content favoring the intracellular localization within cancer cells. These results support the work of Kirpotin et al.

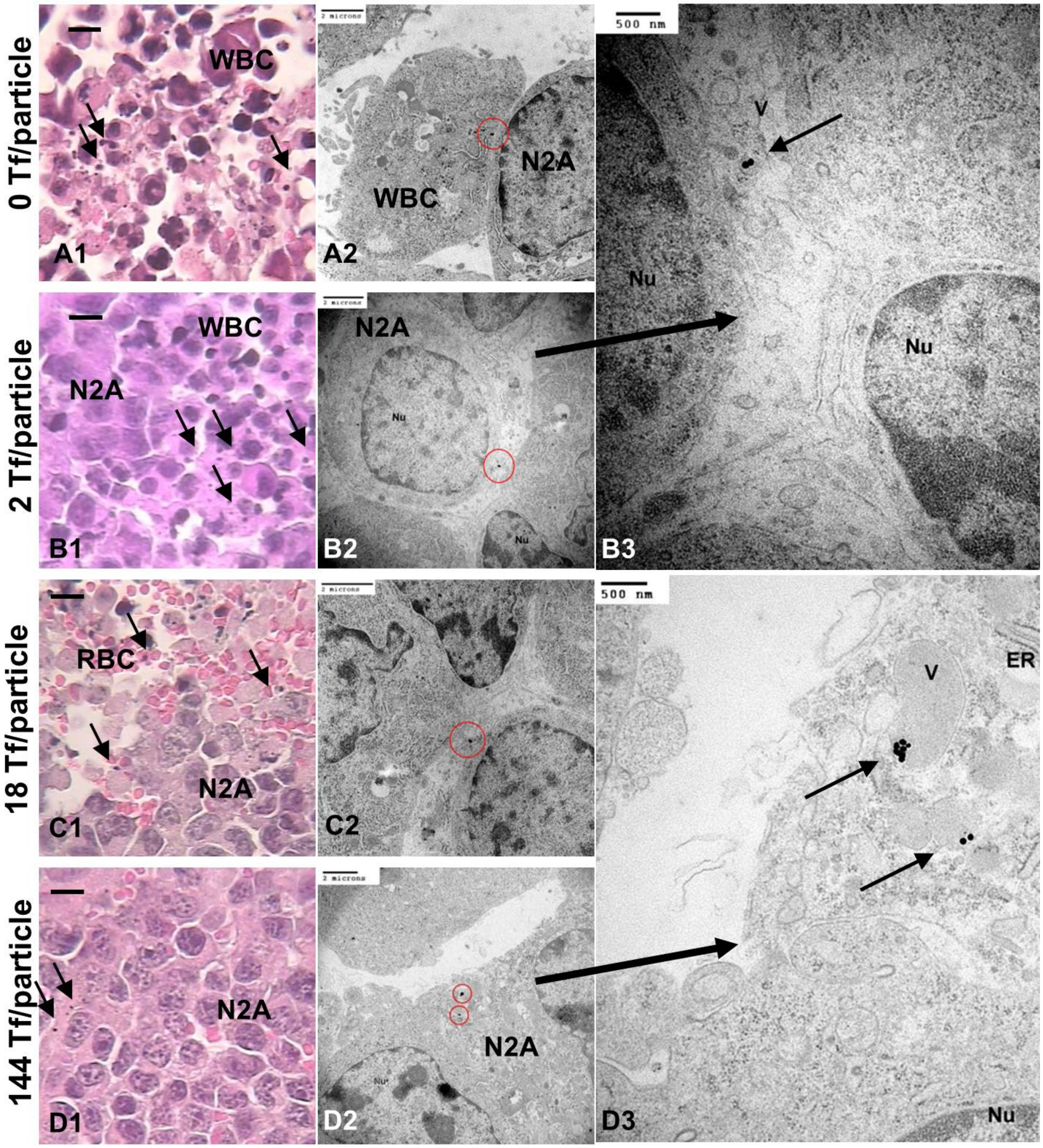

Figure 3.8: In vivo tumor tissue and intracellular distribution. Fig. 3.8A-D1 are light micrographs of "silver-enhanced" tumor sections (scale bar = 10 µm). Independent of Tf content, most particles resided near leukocytes. Electron micrographs show particles either engulfed by leukocytes (Fig. 3.8A2) or touching tangentially Neuro2A cells (Fig. 3.8B-C2, enlarged image: Fig. 3.8B3). Particles of a high Tf content (**V**: 144 Tf/particle) could enter Neuro2A cells (Fig. 3.8D2; enlarged image: Fig. 3.8D3). Enlarged TEM images show a scale bar of 500 nm. All other TEM images display a scale bar of 2 µm. Legend: RBC = red blood cell; M = mitochondrion; Nu = nucleus; ER = endoplasmic reticulum; V = vesicle; WBC = leukocyte; N2A = Neuro2A cell; black arrow = "silver-enhanced" AuNP.

[145] and our previous observations from the targeted delivery of siRNA [146]. Furthermore, **III** and **IV** demonstrate the same in vivo distribution patterns within the tumor as **II**. A critical Tf content is necessary to promote intracellular accumulation of nanoparticles in cancer cells.

In vivo hepatic distribution of $\mathbf{Au_{50}}$-$\mathbf{PEG_{5000}}$-$\mathbf{Tf}_x$ NPs

Since nanoparticles always localize in liver to some extent, we address the fate of Au_{50}-PEG_{5000}-Tf_x NPs in the liver. Compared to Neuro2A cells, hepatocytes have weaker expression of TfRs (data not shown). At the organ level, Tf content does not influence the level of nanoparticle localization in the liver (17-21% ID; Fig. 3.7).

At the tissue level, most particles (independent of Tf content) experience phagocytic uptake by Kupffer cells (Fig. 3.9B2) or reside along hepatic sinusoids (Fig. 3.9A-D1) or in the Space of Disse, a region between hepatocytes and blood endothelial cells that contains reticular fibers, microvilli, and collagen (Fig. 3.9A3). Particles rarely enter hepatocytes (independent of Tf content (Fig. 3.9A2)). Like with the tumor, Tf targeting does not affect bulk particle content in the liver, but yields infrequent instances of accumulation inside hepatocytes given sufficiently high Tf content. From electron micrographs, at the cellular level, **IV** and **V** reside inside vesicles as small clusters near the hepatocyte nucleus, surrounded by mitochondria and endoplasmic reticulum (Fig. 3.9C2-3 and 3.9D2). Yet, below the threshold Tf content, **II** and **III** never permeate through the Space of Disse and enter hepatocytes. Thus, the Tf targeting ligand content does not alter the extent of bulk content in the liver, it only biases particle localization nearby and entry into hepatocytes.

Ligand multivalency

Above we establish the presence of a critical Tf ligand density that imparts nanoparticles the ability to access intracellular locations within the tumor. Yet, Tf is an endogenous protein and

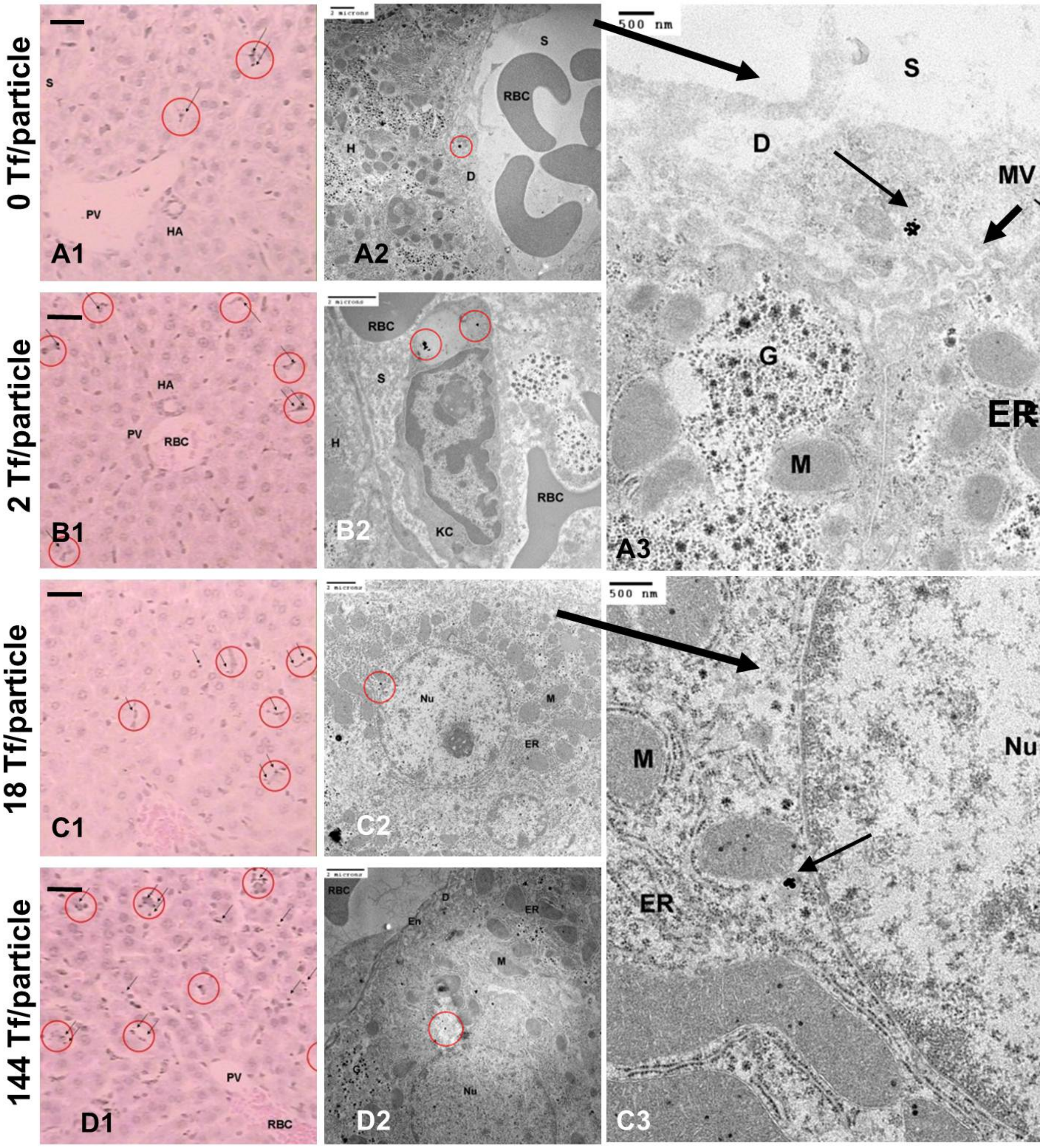

Figure 3.9: In vivo liver tissue and intracellular distribution. Fig. 3.9A-D1 are light micrographs of "silver-enhanced" liver sections (scale bar = 10 µm). Independent of Tf content, particles rarely entered hepatocytes. Electron micrographs show particles either engulfed by Kupffer cells (Fig. 3.9A2) or residing in the Space of Disse (Fig. 3.9A2, enlarged image: Fig. 3.9A3). Hepatocytes could internalize particles of high Tf contents (**IV** and **V**; Fig. 3.9C-D2; enlarged image: Fig. 3.9C3). Enlarged TEM images show a scale bar of 500 nm. All other TEM images display a scale bar of 2 µm. Legend: RBC = red blood cell; D = Space of Disse; KC and red circle = Kupffer cell; S = sinusoid; M = mitochondrion; MV = microvillus; Nu = nucleus; G = Golgi apparatus; ER = endoplasmic reticulum; En = endothelial cell; H = hepatocyte; HA = hepatic artery; PV = hepatic portal vein; black arrow = "silver-enhanced" AuNP.

exists in normal serum. If background Tf can compete against Au$_{50}$-PEG$_{5000}$-Tf$_x$ NPs for Tf receptors, how would this affect the utility of Tf-targeted nanoparticles for clinical applications?

Classical kinetics can provide a reasonable model to address this question. According to the competitive binding model of N different species binding the same site, the equilibrium binding fraction, θ_i, of species i depends on the binding dissociation constants (K_d^i's) and concentrations C^i of all competitors available. The mathematical expression of θ_i is given below:

$$\theta_i = \frac{(K_d^i)^{-1}C^i}{1 + \Sigma_{i=1}^{N}(K_d^i)^{-1}C^i}$$

From Fig. 3.4 and using the geometric assumption of partial interaction with Tf receptors, the effective K_d^i's of Au$_{50}$-PEG$_{5000}$-Tf$_x$ NPs are 0.13 nM and 0.03 nM for $x = 18$ (**IV**) and 144 (**V**), respectively. For our preceding animal models, the Neuro2A tumor grew to an approximate volume of 100 mm^3 (0.1 mL) before i.v. injection. Within the tumor, the blood vasculature volume fraction is 0.15 [138]. Thus, the tumor blood compartment has a volume of 0.015 mL. If 2% ID of Au$_{50}$-PEG$_{5000}$-Tf$_x$ NPs reached the tumor 24 h after injection for all values of x (Fig. 3.7), the approximate number of particles in the tumor is $4.5 \times 10^{11} \times 2\% = 9 \times 10^9$. Thus, the concentration of Au$_{50}$-PEG$_{5000}$-Tf$_x$ NPs in the tumor blood compartment is ~1.5 nM.

The typical Tf concentration in circulating serum is ~12.5 µM [154]. Tf has two distinct iron binding sites. Depending on the number of Fe^{3+} ions bound per Tf molecule, Tf can take the form of apo-Tf, monoferric-Tf, and diferric-Tf (a.k.a. holo-Tf), which signify the binding of zero, one, and two Fe^{3+} ions, respectively. From Fig. 3.3, the K_d of holo-Tf is 64 nM. Prior data from rabbits indicate that the corresponding K_d's of apo-Tf and monoferric-Tf are 4600 nM and 265 nM, respectively [155]. At normal plasma iron concentrations, random distribution of the metal on the available Tf binding sites would give rise to a population of molecules of which 50% were apo-Tf, 40% monoferric-Tf, and 10% diferric-Tf [156].

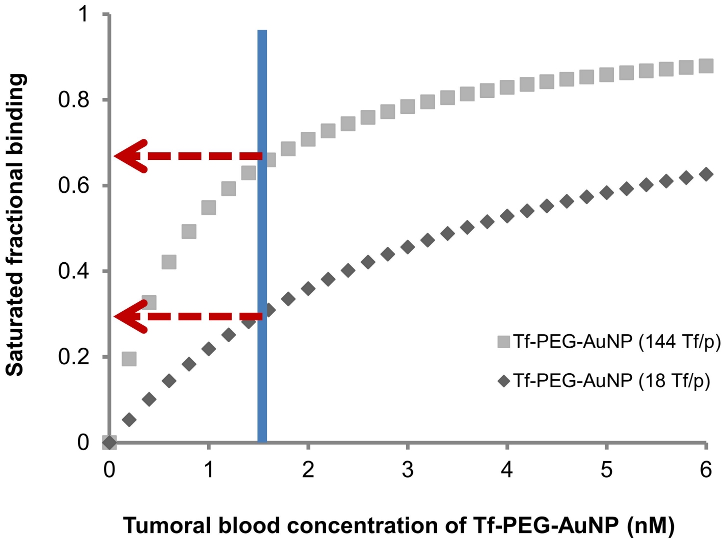

Figure 3.10: Competition with background Tf in serum. Langmuir isotherms of Au_{50}-PEG_{5000}-Tf_x NPs ($x = 18$ (**IV**) or 144 (**V**)) on TfRs of N2A cells. Above the threshold Tf content, **V** can outcompete the background serum apo-Tf, monoferric-Tf, and diferric-Tf in binding 65% of the available TfRs. **IV** can only attach to 30% of the receptors, losing the remaining receptors to the background Tf in serum.

With the K_d^i's and C^i for all pertinent Tf-containing species, we can plot the equilibrium binding curves of Au_{50}-PEG_{5000}-Tf_x NPs ($x = 18$ and 144) over Tf receptors on Neuro2A cells within the mouse tumor (Fig. 3.10). Using the above parameters, the competitive binding model predicts an occupation of 65% of the available Tf receptors on the Neuro2A cell surface by **V** particles, in great excess to those occupied by the competitive serum Tf. In contrast, **IV** particles can only bind to 30% of the Tf receptors, losing the remaining receptors to background serum Tf. From this, the intracellular localization exclusively observed for **V** may stem from their innate ability to outcompete serum Tf molecules in binding to Tf receptors.

Effect of receptor density

Prior analysis till this point involves strictly one cell line, Neuro2A, to engage multivalent binding with Au_{50}-PEG_{5000}-Tf_x NPs. Neuro2A has an upregulated expression of surface Tf receptors (TfRs) (Fig. 3.2A; ~110 TfR/µm^2). This value assumes that the TfR density of Neuro2A is the

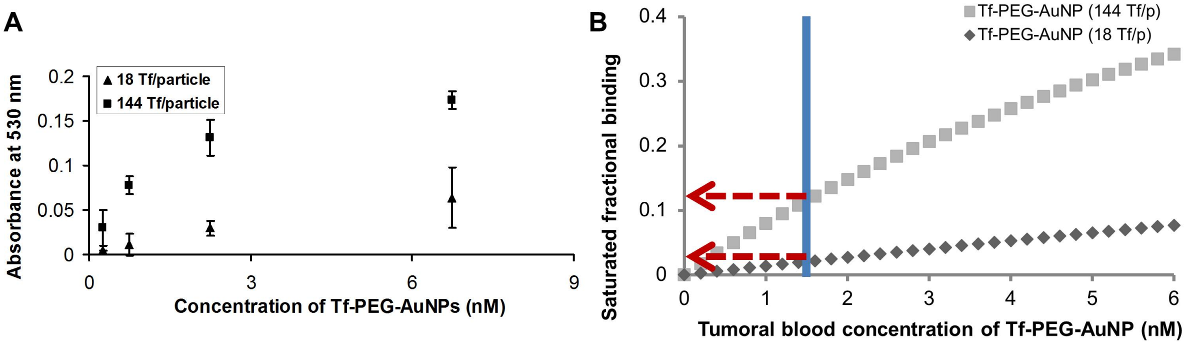

Figure 3.11: Effect of receptor density on multivalency. (A) Binding of Au$_{50}$-PEG$_{5000}$-Tf$_x$ NPs ($x = 18$ (**IV**) or 144 (**V**)) on 3T3 cells. **IV** bound consideraly less cells compared to Neuro2A cells. **V** particles even showed negligible binding. (B) Langmuir isotherms of Au$_{50}$-PEG$_{5000}$-Tf$_x$ NPs ($x = 18$ or 144) on TfRs of 3T3 cells. **IV** and **V** could bind to limited fraction of TfRs (<15%) due to lower TfR densities.

same as HepG2 [157] and that the diameter of a Neuro2A cell is 12 µm. What is the effect of receptor density of tumor cells on multivalent binding by liganded nanoparticles?

We repeated in vitro binding experiments using 3T3 cells (mouse fibroblast), which have much weaker surface TfR expression (~21 TfR/µm^2 [158]) compared to Neuro2A cells. The binding of Tf-AF488 onto 3T3 cells revealed less overall fluorescent retention compared to Neuro2A cells, as well as a K_d of 36 nM (data not shown). Neuro2A and 3T3 cells have similar K_d's (64 nM vs. 36 nM), implying that the degree of binding between monovalent Tf-AF488 and each TfR (1:1 interaction) is consistent across cell lines and independent of TfR expression.

In vitro binding experiments using 3T3 cells with **IV** and **V** particles followed. **III** particles barely bound to Neuro2A cells (Fig. 3.6), and hence were not included in the binding study with 3T3 cells (with even lower TfR densities). Due to reduced level of TfR expression, both particle types bound to significantly less 3T3 cells compared to Neuro2A cells of the same population (Fig. 3.11A). The increase in absorbance readings due to binding of **IV** was almost beyond the detection limit of the UV-Vis spectrometer. The interaction was so weak that the binding curve appears linear rather than hyperbolic (expected shape for a typical isotherm). Scatchard analysis based on the binding data indicate that the K_d's of **IV** and **V** are 9.94 nM (by extrapolation from the linear portion of the binding curve) and 1.60 nM, respectively (data not shown). A comparison of the K_d's of **IV** and **V** between the Neuro2A and 3T3 cells underscores that the multivalent interactions for tumor targeting depends on both the ligand density on the nanoparticles as well as the receptor density of the tumor cells. Binding enhancement due to multivalency is highest when both ligand and receptor densities are elevated.

Another approach to evaluate the effect of receptor density on tumor targeting is to employ the competitive binding model. By inserting the K_d's of **IV** and **V** obtained for 3T3 cells and applying the geometric assumption that only 21.33% of the ligands bound to TfRs, the Langmuir isotherms demonstrated considerably an attenuated equilibrium binding fraction for these particles compared to its counterpart curve for Neuro2A cells (Fig. 3.11B). From this model, even **V**, with the highest density of Tf ligands, could only bind to <15% of the receptors, suggesting the futility of intracellular localization of **V** within a 3T3 tumor (with weak TfR expression, and assuming that it is tumorigenic).

3.4 Conclusion

In summary, our results demonstrate the use of Au_{50}-PEG_{5000}-Tf_x NPs as imaging agents to understand targeted nanoparticle behavior in vivo. With similar sizes and ζ-potentials, targeted particles of different Tf contents (**II-V**) permit the investigation of the effect of targeting ligand content on nanoparticle distribution in vivo. PEGylation confers steric stability against salt- and serum-induced aggregation in vitro. Because **II-V** localize in cellular structures of the tumor and liver as individual entities, it is implied that the steric stabilization occurs in vivo as well. Despite complete nanoparticle PEGylation, the RES organs (liver and spleen) still show significant localization (17-21% ID and 5-6% ID, respectively) in excess to that of the tumor (2-3% ID), irrespective of Tf content. Active targeting with Au_{50}-PEG_{5000}-Tf_x NPs leads to nanoparticle internalization into cancer cells with abundant TfR expression (Neuro2A cells).

These data when taken together with past tumor permeation work conducted with other targeted nanoparticle delivery systems (dextran [99], immunoliposomes [145], and Tf-targeted cyclodextrin [146]), support the conclusion that targeted nanoparticles in the sub-100 nm size range will always deliver a higher payload (drug, imaging agent, or combination) into cancer cells of the tumor than their untargeted counterparts.

Moreover, from the present study, there is a minimum targeting ligand content on the nanoparticle that provides the sufficient condition for effective active targeting. Below this threshold content, targeted nanoparticles manifest similar in vivo distribution patterns as untargeted particles on organ, tissue, and cellular levels. Rather than simplistically switching nanoparticles from an "off" state to an "on" state, i.e., untargeted vs. targeted, our results underscore the importance of optimizing the ligand content on the nanoparticle surface in order to achieve effective intracellular targeting of cancer cells in solid tumors.

A competitive binding model from classical kinetics can provide additional insights into understanding the basis of multivalent interactions for tumor targeting. From this model, there are two key criteria that govern multivalency. To start with, nanoparticles must contain sufficient ligands on their periphery to compete with endogeneous ligands in background serum for the same tumor surface receptors. From in vitro binding studies and in vivo imaging of animal models, one can deduce the threshold surface ligand content to achieve tumor intracellular accumulation. Besides this threshold ligand content, the model also predicts that nanoparticles must interact with tumor cells with up-regulated expression of surface receptors. Further binding and imaging data from different tumor models can ascertain the critical receptor density.

Taking this model with all other data together, multivalent interactions may be the essence of intracellular localization of nanoparticles within the tumor, and can only happen in systems with sufficiently high ligand content and receptor density. In other words, with sufficient amounts of ligands, nanoparticles will target tumor cells more selectively than normal cells, and hence

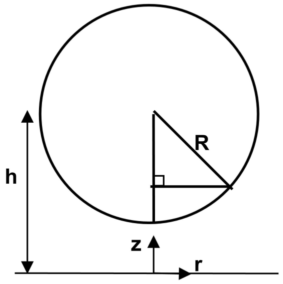

Figure 3.12: Definition sketch of a sphere of radius R levitating on top of a flat surface.

can direct the drug payload to the targeted site without harming normal cells due to off-target effects. This selection process stems from the multivalent interactions as described above.

3.5 Supporting Information

The K_d's obtained from the Scatchard analysis assumes that all Tf moieties immobilized on $\mathrm{Au_{50}}$-$\mathrm{PEG_{5000}}$-Tf_x NPs interact with the TfRs on the cellular surface. Due to particle curvature, this assumption does not make much physical sense. Is there an approximation that evaluates the actual fraction of Tf in contact with the cell surface?

Consider a sphere of radius R whose center is of a distance h away from a flat surface. The spherical curvature dictates the appropriate length scaling (Fig. 3.12). The sphere represents a PEGylated gold nanoparticle (**II**), whereas the flat surface depicts a cellular surface that have an overexpression of TfRs. The distance between the sphere and the flat surface reflects the approximate height of Tf. By the Pythagoras theorem, $(z-h)^2 + r^2 = R^2$.

For the bottom of sphere, and performing a Taylor expansion about the origin assuming $r \ll R$, we derive the following mathematical relationship:

$$z = h - R\sqrt{1-\left(\frac{r}{R}\right)^2} \approx h - R\left[1 - \frac{1}{2}\left(\frac{r}{R}\right)^2 + O\left(\frac{r}{R}\right)^4\right] \qquad \frac{z}{\epsilon R} \sim 1 + \frac{1}{2\epsilon}\left(\frac{r}{R}\right)^2$$

In these expressions, $\epsilon = (h-R)/R = d/R$ and d is the distance of the thin gap between the

NP	$K_d^{100\%}$	$K_d^{21.33\%}$	Binding enhancement
IV	1.06	0.23	$\sim$ 600 fold
V	0.13	0.03	$\sim$ 4800 fold

Table 3.2: Multivalency of Au_{50}-PEG_{5000}-Tf_x NPs. Enhancement in binding affinity (from effective K_d's) by three orders of magnitude for **IV** ($x = 18$) and **V** ($x = 144$) highlights the effect of multivalency.

bottom of sphere and flat surface. If $r \sim R$, $z/\epsilon R$ is huge and does not converge because $1/\epsilon$ is huge. If $r \ll R$, $z/\epsilon R$ is small and the second term of the expansion vanishes. To account for the curvature of the sphere, set the second term of the expansion to the same size as the first term (i.e., order 1). This gives the relevant length scale in the radial direction that indicates contact of the sphere with the flat surface: $r = 2R\epsilon^{1/2} = 2(dR)^{1/2}$. With the assumption of homogeneous Tf distribution on the entire spherical surface of PEG-AuNPs ($4\pi R^2$), the fraction of contact is:

$$\frac{\pi[2(dR)^{1/2}]^2}{4\pi R^2} = \frac{d}{R} \equiv \epsilon$$

From Table 3.1, the hydrodynamic size of **II** in 1× PBS is 75 nm. Tf has a Stokes-Einstein diameter of 8 nm [159]. These two measurements ($R = 37.5$ nm and $d = 8$ nm) collectively imply a fraction of ~21.33% of Tf attached on each Au_{50}-PEG_{5000}-Tf_x NP in contact with TfRs. Because ($\epsilon \equiv d/R = 0.2 < 1$), the thin gap lubrication approximation is valid.

Table 3.2 displays the effective K_d's with and without the geometric assumption. From Fig. 3.3, the K_d of a single Tf-PEG_{5000}-SAc ligand is 144 nM. With the geometric assumption, the multivalent enhancement in binding is up to ~600 and ~4800-fold for **IV** and **V**, respectively.

3.6 Materials and Methods

Synthesis of Tf-PEG_{5000}-SAc

HO-PEG-NH_2 (MW: 5000; Laysan Bio) was reacted with excess N-succinimidyl-S-acetylthio acetate (SATA; Pierce Biotechnology, Rockford, IL) in dimethylformamide (DMF) at RT for 4 h. The product was reacted with excess N, N-disuccinimidyl carbonate (DSC; Pierce Biotechnology) in DMF/dioxane at room temperature for 4 h to give NHS-PEG$_{5000}$-SAc. Upon solvent removal and drying under vacuuo, NHS-PEG$_{5000}$-SAc was reacted with human holo-transferrin (Tf; Sigma) at a 2:5 molar ratio in 50 mM sodium phosphate at RT for 2.5 h to form Tf-PEG$_{5000}$-SAc. Purification involved passing the reaction mixture through a 5 mL HiTrap Phenyl HIC column in AKTA FPLC (GE Healthcare), with 1 M ammonium sulfate as the high salt and 50 mM sodium phosphate as the low salt.

Competitive binding assay

Plated in a 24-well plate at a population of 5×10^4 2 d in advance, Neuro2A cells were incubated in 0.45 mL of OptiMEM I containing 50 nM Tf-AF488 and different amounts of Tf-PEG$_{5000}$-SAc at 37 °C and 5% CO_2 for 1 h. After rinses with 1× PBS to remove unbound Tf conjugates, cells were analyzed with FACSCalibur (Becton Dickinson Biosciences) to quantify the mean fluorescence at 488 nm. The Tf on both Tf-PEG$_{5000}$-SAc and Tf-AF488 (Tf conjugated to AlexaFluor488) bind to and compete for surface transferrin receptors (TfRs) of Neuro2A cells. Reported data show percent of mean fluorescence of cells incubated with Tf-AF488 only. Analogous experiments were conducted with holo-Tf and methoxy-PEG$_{5000}$-SH (mPEG-SH; MW: 5000; Sigma-Aldrich) for comparison.

Binding of Tf-AF488 to cells

Plated in a 24-well plate at a population of 5×10^4 cells per well 2 d in advance, Neuro2A and 3T3 (mouse fibroblast) cells were incubated in 0.45 mL of OptiMEM I (Invitrogen) containing various concentrations of Tf-AF488 at 37 °C and 5% CO_2 for 1 h. After rinses with 1× PBS to remove unbound Tf-AF488, cells were analyzed with FACSCalibur to quantify the mean fluorescence at 488 nm. A Scatchard analysis gave the dissociation constant (K_d) of Tf-AF488 from TfRs of cells.

Assembly of transferrin-targeted, PEGylated gold nanoparticles

The deprotection of 6 µL of 1 µg/L Tf-PEG$_{5000}$-SAc in 1× PBS was performed with the addition of 54 µL of 50 mM NH_2OH (in 50 mM sodium phosphate and 25 mM EDTA; pH = 7.5) at RT for 2 h. Adding deionized water to Tf-PEG$_{5000}$-SH, the deprotected Tf conjugate, yielded a 0.3 mL volume for salt removal by a 0.5 mL Zeba Desalt Spin Column (Thermo Scientific). Salt removal prevents salt-induced aggregation of gold particles, yet it led to 25% loss of Tf content due to entrapment in the column.

To prepare AuNPs with increasing Tf contents, 0.5, 5, or 50 µL of desalted Tf-PEG$_{5000}$-SH (15 ng/µL) was added into 0.5 mL of 50 nm unconjugated AuNPs (Ted Pella) at a concentration of 4.5×10^{10} particles/mL. The reaction proceeded at RT with shaking for 1 h. Complete PEGylation of the unreacted gold surface required the introduction of 10 µL of 1 mM mPEG$_{5000}$-SH into the reaction mixture, and proceeded at RT with shaking for 30 min. The reaction mixture was centrifuged at 14,000 × g for 10 min, followed by removal of the supernatant fraction that contained unreacted or dimerized Tf- and methoxy-PEG$_{5000}$s. Au$_{50}$-PEG$_{5000}$-Tf$_x$ NPs sank to the bottom of the reaction vial as a brick-red pellet. The pellet was rinsed twice with 0.45 mL of 1× PBS for 10 min in a shaker.

0.5 mL of 50 nm AuNPs were PEGylated with 10 µL of 1 mM mPEG$_{5000}$-SH at RT with shaking for 30 min. The removal of excess mPEG$_{5000}$-SH yielded Au$_{50}$-PEG$_{5000}$ NPs as untargeted control particles.

Estimation of Tf content

A human transferrin ELISA quantitation kit (Bethyl Laboratories) was used to determine the amount of unbound Tf-PEG$_{5000}$-SH in the supernatant fractions collected from the synthesis and PBS rinse steps. Given the initial amount of Tf-PEG$_{5000}$-SH added, a mass balance indirectly yields the Tf content of Au$_{50}$-PEG$_{5000}$-Tf$_x$ NPs. All reported contents are from triplicate experiments.

Particle stability in salt and serum containing solutions

To monitor particle stability in salt solutions, a pellet containing 2.25×10^{10} unmodified AuNPs, Au$_{50}$-PEG$_{5000}$ NPs, or Au$_{50}$-PEG$_{5000}$-Tf$_x$ NPs of different Tf contents ($x = 2$, 18, and 144 Tf per particle) were resuspended in 1.26 mL of deionized water in a cuvette placed inside the ZetaPals instrument. 4 min through HD measurements, 0.14 mL of 10× PBS was added to the cuvette. Size measurements continued for 16 min. The assessment of particle stability in serum entailed the resuspension of a pellet containing 2.25×10^{10} particles in 200 µL of 90% fresh mouse serum (collected by saphenous vein extraction from A/J mice) in 1× PBS. A Safire^2 Microplate Reader (Tecan) was used to measure the absorbance of the AuNP-serum mixture at 37 °C for 1 h at 590 nm, a wavelength indicative of gold flocculation.

Binding of Au_{50}-PEG_{5000}-Tf_x NPs to cells

Plated in a 24-well plate at a population of 8×10^5 cells per well 2 d in advance, Neuro2A and 3T3 cells were incubated in 0.2 mL of OptiMEM I containing different concentrations of Au_{50}-PEG_{5000}-Tf_x NPs ($x = 2$, 18, and 144) at 37 °C and 5% CO_2 for 1 h. After rinses with 1× PBS, a Safire^2 Microplate Reader (Tecan) was used to measure the cell absorbance at 530 nm, the plasmon peak of Au_{50}-PEG_{5000} NPs. To account for non-specific adsorption, cells were incubated with identical concentrations of Au_{50}-PEG_{5000} NPs. For Scatchard analyses to deduce the effective K_d's of Au_{50}-PEG_{5000}-Tf_x NPs, the free gold concentration was quantified by Safire^2 based on a calibration curve of known concentrations of Au_{50}-PEG_{5000} NPs. Reported values, after deduction of non-specific gold signals, are from duplicate experiments.

Cell lines

Neuro2A and 3T3 cells were cultured at 37 °C and 5% CO_2 in DMEM, supplemented with 10% FBS, 100 units/mL penicillin, and 100 units/mL streptomycin. Before tumor implantation, Neuro2A cells were washed with 1× PBS, trypsinized, and resuspended in serum-free, antibiotic-free DMEM.

Animal models

In the right hind flank, each 8-week, female A/J mice (Jackson Laboratory) received subcutaneous implantation of 10^6 Neuro2A cells in 0.1 mL of DMEM.

Systemic administration

2 weeks after tumor implantation, four mouse groups (N = 3) received administration of Au_{50}-PEG_{5000}-Tf_x NPs ($x = 0$, 2, 18, and 144) via the tail vein (4.5×10^{11} particles in 0.1 mL of D5W). Animal sacrifice by CO_2 overdose took place 24 h after injection, followed by collection and immersion-fixation of the tumor, liver, kidney, heart, spleen, and lung in 4% PFA in 1× PBS at 4 °C for 2 weeks.

Chapter 4

Targeting Kidney Mesangium by Nanoparticles of Defined Sizes

4.1 Abstract

Nanoparticles are being investigated for numerous medical applications, and are showing potential as an emerging class of carriers for drug delivery [137] [106]. Investigations on how physicochemical properties (e.g., size, surface charge, shape, and density of targeting ligands) of nanoparticles enable their ability to overcome biological barriers and reach designated cellular destinations in sufficient amounts to elicit biological efficacy are of interest. Despite proven success in nanoparticle accumulation at cellular locations and occurrence of downstream therapeutic effects (e.g., target gene inhibition) in a selected few organs such as tumor [160] and liver [161], reports on effective delivery of engineered nanoparticles to other organs remain scarce. We show that nanoparticles of ~75 ± 25 nm diameters target the kidney mesangium. These data are the first to show the effects of particle diameter on targeting the kidney mesangium. Since many diseases originate from this area of the kidney, our findings establish design criteria for constructing nanoparticle-based therapeutics for targeting diseases that involve the kidney mesangium.

Excerpts of this chapter are reproduced with permission from "Targeting kidney mesangium by nanoparticles of defined sizes." Chung Hang J. Choi, Jonathan E. Zuckerman, Paul Webster, and Mark E. Davis. *Proc. Natl. Acad. Sci. USA*. **108**, 16, 6656-6661 (2011).

4.2 Introduction

Constructing nanoparticles for drug delivery requires knowledge in colloidal science and biology, where biological constraints generally dictate the design of nanoparticle therapeutics and imaging agents. A celebrated design criterion is the notion of "renal clearance" [123] [162]. That is, nanoparticles will experience rapid clearance by the kidney if they are smaller than ∼10 nm in diameter. Such clearance originates from the innate function of the kidney as a blood filter.

Renal physiology in brief

The structural and functional unit of the kidney, the nephron, consists of the renal corpuscle and tubule system. The renal corpuscle contains a tuft of blood capillaries and support tissue (the mesangium: Fig. 4.1A-C) called the glomerulus. A fraction of blood plasma entering the glomerulus will pass through the "glomerular filtration apparatus" to produce an ultrafiltrate, which will be collected by the tubule system and ultimately be processed into urine. The first component is the glomerular endothelium with pores that have been reported to be in the range of 80-100 nm in diameter [163]. Next, the glomerular basement membrane (GBM), a 300-350 nm thick basal lamina rich in heparan sulfate [164] and charged proteoglycans with an average pore size of 3 nm [165], filters small molecules by size and charge. Behind the GBM lies podocytes, cells with interdigitating foot processes that form "filtration slits" of 32 nm in width [166]. The glomerular filtration apparatus, taken in its entirety, possesses an effective size cutoff of 10 nm, and is responsible for the rapid "renal clearance" of small nanoparticles.

Kidney targeting using nanoparticles

Many nanoparticle-based contrasting agents for in vivo imaging were designed to be smaller than this size cutoff [167] [168]. Prolonged residency of nanoparticles in the kidney has been shown to induce toxicity in the form of cell shrinkage, due to excessive nanoparticle uptake by

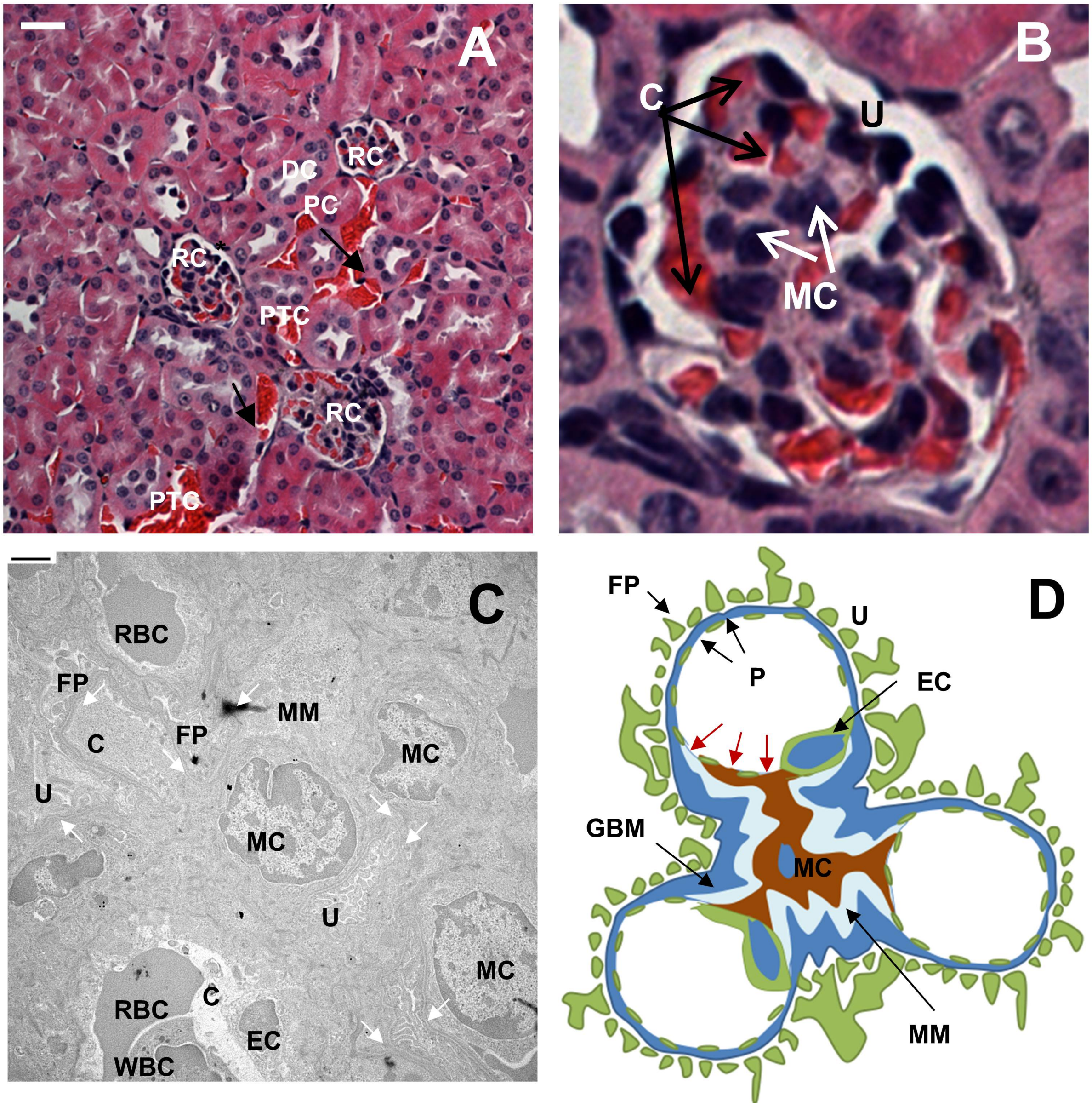

Figure 4.1: Illustrations of the renal corpuscle and the mesangium. (A) This light micrograph reveals the typical morphology of the renal cortex. Scale bar = 10 μm. (B) This close-up reveals the inner structure of a renal corpuscle. (C) This transmission electron micrograph shows the internal structures of the renal corpuscles. Scale bar = 10 μm. (D) This schematic diagram shows the relationship between mesangial cells and glomerular capillaries. Legend: renal corpuscles (RC), distal convoluted tubules (DC), proximal convoluted tubules (PC), peritubular capillaries (PTC), red blood cells (RBC), leukocytes (WBC), mesangial matrix (MM), mesangial cells (MC), foot processes of podocytes (FP), urinary space (U), glomerular capillary space (C), endothelial cell (EC), glomerular basement membrane (GBM), and pores (P) of the fenestrated endothelium of glomerular capillaries. In panel C, white arrows trace the glomerular basement membrane. In panel D, red arrows indicate the pores between the glomerular capillaries and mesangium. If smaller than the pore width, particles can enter the mesangium from the glomerular capillaries in the absence of GBM and podocytes as structural barriers.

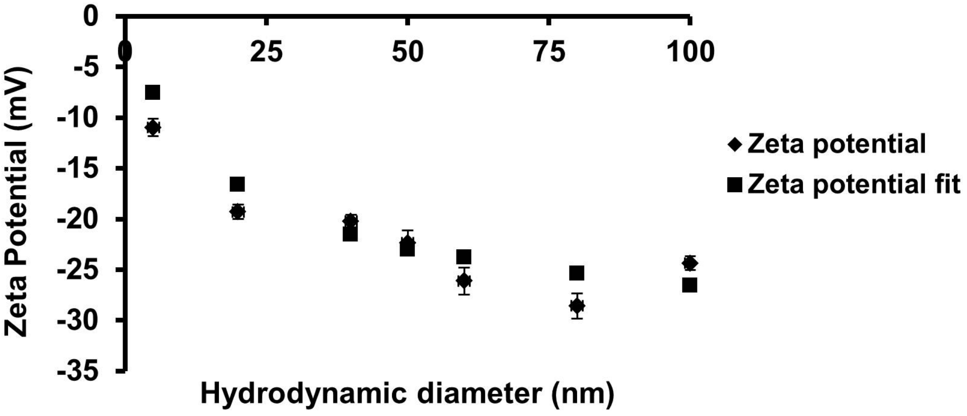

unmodified Au$_x$ NPs	water HD (nm)	s.d. (nm)	1 mM KCl ZP (mV)	s.d. (mV)	Predictions (electrokinetics) ZP (mV)
5	6.2	0.8	-10.98	0.56	-7.57252
10	10.2	0.4	-11.98	1.26	-10.8079
20	21.6	0.2	-19.31	0.76	-16.6154
40	41.2	0.2	-20.21	1.54	-21.5425
50	51.4	0.2	-22.34	1.31	-23.0364
60	58.1	0.5	-26.12	0.91	-23.8054
80	76.5	0.3	-28.56	1.45	-25.3679
100	98.3	0.5	-24.36	1.19	-26.5900

Figure 4.2: Physicochemical characterization of unmodified gold nanoparticles (Au$_x$ NPs). Precise values of hydrodynamic diameter (HD) and ζ-potential (ZP) of Au$_x$ NPs are listed, with the predicted ζ-potential due to Debye-Hückel electrokinetic theory.

renal cells [169][170]. Closer examination of the renal corpuscle reveals the existence of another intriguing size cutoff that would affect the distribution pattern. Within the renal corpuscle, in the absence of GBM and podocytes, the sole dividing barrier between the mesangium (mesangial cells and extracellular matrix) and the glomerulus is the fenestrated endothelium (Fig. 4.1D, modified from Sakai and Kriz [171]). Submicron-sized nanoparticles may diffuse and accumulate indefinitely in the mesangium once they depart from the glomerulus through these pores.

Here, we illustrate the size-dependent delivery of PEGylated gold nanoparticles to the kidney mesangium. Gold nanoparticles (AuNPs) were used here for the following reasons. They are compatible with multiple imaging methods. As rigid and non-decomposable objects, submicron-sized AuNPs larger than ∼10 nm cannot escape the kidney by renal clearance.

NP	x (nm)	y (Da)	HD$_{water}$ (nm)	HD$_{PBS}$ (nm)	ZP (mV)
Au$_5$-PEG$_{5000}$	5.3 ± 0.5	5000	26.2 ± 0.3	24.8 ± 0.5	-8.44 ± 0.85
Au$_{20}$-PEG$_{5000}$	21.6 ± 0.2	5000	43.1 ± 0.2	41.4 ± 0.4	-9.62 ± 0.62
Au$_{40}$-PEG$_{4000}$	41.2 ± 0.2	4130	59.1 ± 0.3	58.6 ± 0.5	-12.34 ± 1.21
Au$_{50}$-PEG$_{5000}$	51.4 ± 0.2	5000	78.8 ± 0.2	76.5 ± 0.4	-10.91 ± 1.33
Au$_{60}$-PEG$_{7000}$	58.1 ± 0.5	7359	94.6 ± 0.5	96.2 ± 0.2	-12.51 ± 1.24
Au$_{80}$-PEG$_{10000}$	76.5 ± 0.3	10000	127.6 ± 2.1	128.9 ± 0.9	-8.93 ± 0.67
Au$_{100}$-PEG$_{20000}$	98.3 ± 0.3	20000	167.4 ± 9.6	164.3 ± 8.6	-9.67 ± 0.31

Table 4.1: Physicochemical properties of Au$_x$-PEG$_y$ NPs. x = core diameter of AuNP; y = chain length of grafted PEG; HD = hydrodynamic diameter; ZP = ζ-potential. The table presents data as average ± s.d. from triplicate runs. All particle types have near-constant ZPs despite their size differences.

4.3 Results and Discussion

Assembly of Au$_x$-PEG$_y$ NPs

Unmodified AuNPs of different sizes have zeta potentials (ζ) ranging from -11 to -28 mV (Fig. 4.2). For any charged sphere of radius R in an electrolyte, its ζ is given below, where σ, ϵ, and κ^{-1} are the surface charge density, permittivity constant, and Debye length.

$$\zeta = \frac{\sigma}{\epsilon} \frac{R}{1 + \kappa R}$$

From this equation, ζ of charged gold spheres becomes more negative as R increases, consistent with data shown in Fig. 4.2. For typical ζ measurements in 1 mM KCl at room temperature, κ^{-1} is roughly 9.8 nm, a constant independent of R. By curve fitting of the measured ζ as a function of R, the dimensionless charge density (σ/ϵ) is approximately 3. The measured ζ values are consistent with predictions due to classical electrokinetic theory, and suggest that unmodified AuNPs of all sizes share the same surface charge density (σ). In other words, the larger the unmodified AuNPs, the more negative the surface charge.

To create an array of nanoparticles with variable size and relatively constant surface charge, we exploit the charge screening effect of poly (ethylene glycol) (PEG). This would require the engraftment of longer PEG chains onto the larger nanoparticles. This concept prompted us to

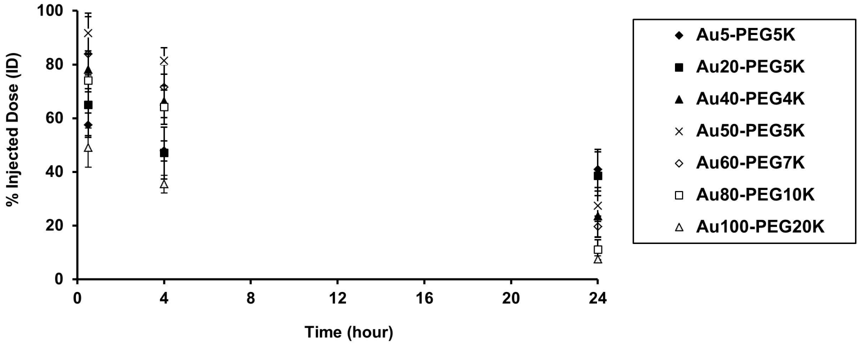

t (h)	Au_5-PEG_{5K}	Au_{20}-PEG_{5K}	Au_{40}-PEG_{4K}	Au_{50}-PEG_{5K}	Au_{60}-PEG_{7K}	Au_{80}-PEG_{10K}	Au_{100}-PEG_{20K}
0.5	57.36 ± 4.53	64.84 ± 11.30	78.04 ± 7.04	91.61 ± 7.53	83.83 ± 13.96	73.96 ± 9.85	49.04 ± 7.31
4	47.83 ± 3.74	46.97 ± 9.67	66.14 ± 5.89	81.31 ± 4.98	71.42 ± 8.46	64.12 ± 6.39	35.44 ± 3.27
24	40.83 ± 6.60	38.43 ± 9.91	23.45 ± 7.73	27.22 ± 5.71	19.54 ± 3.94	10.97 ± 3.80	7.48 ± 1.26

Figure 4.3: Blood pharmacokinetics. All Au_x-PEG_y NPs revealed extended circulation times in blood. Gold contents are normalized to percent injected dose (% ID). Error bars indicate one s.d. from each Au_x-PEG_y NP class (N = 3). Exact values of blood particle concentration at 0.5, 4, and 24 h are provided.

use an assortment of PEGylated gold nanoparticles (Au_x-PEG_y NPs) of different core diameters (x) and PEGs of different chain lengths (y) (Table 4.1). The engraftment procedure entailed the use of methoxy-PEG-thiol (mPEG-SH) molecules, whose terminal thiol group can react with the gold surface via the formation of gold-thiol covalent bonds. Careful choice of x and y gave rise to a near-constant ζ (roughly -10 mV) for Au_x-PEG_y NPs of various final hydrodynamic sizes (Table 4.1). In general, the engraftment of each additional 2000 molecular weight of PEG onto the gold surface translates to an increase in 5 nm of the hydrodynamic diameter of Au_x-PEG_y NPs. This approximate linearity between the PEG corona thickness and chain length is consistent with previous predictions for tethered polymer brushes on spherical interfaces without pronounced curvature [114] (see supporting information). All Au_x-PEG_y NPs showed colloidal stability in 1× PBS after 24 h, with hydrodynamic sizes roughly equal to those in water.

Blood pharmacokinetics

Balb/c mice (N = 3) received single i.v. injections of each type of Au_x-PEG_y NPs at the same particle concentration. From each mouse, blood was withdrawn via the saphenous vein at various

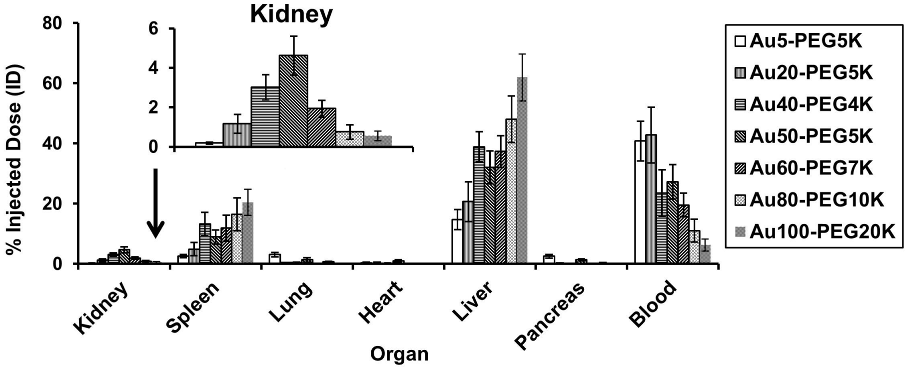

Organ	Au_5-PEG_{5K}	Au_{20}-PEG_{5K}	Au_{40}-PEG_{4K}	Au_{50}-PEG_{5K}	Au_{60}-PEG_{7K}	Au_{80}-PEG_{10K}	Au_{100}-PEG_{20K}
Kidney	0.19 ± 0.05	1.16 ± 0.48	3.01 ± 0.64	4.62 ± 0.98	1.92 ± 0.43	0.74 ± 0.37	0.55 ± 0.25
Spleen	2.55 ± 0.56	4.86 ± 2.21	13.23 ± 3.89	8.94 ± 2.31	11.82 ± 4.31	16.42 ± 5.42	20.41 ± 4.31
Lung	3.06 ± 0.77	0.36 ± 0.14	0.36 ± 0.23	1.31 ± 0.72	0.16 ± 0.06	0.68 ± 0.14	0.19 ± 0.03
Heart	0.36 ± 0.18	0.31 ± 0.23	0.26 ± 0.10	0.91 ± 0.42	0.07 ± 0.01	0.21 ± 0.02	0.07 ± 0.01
Liver	14.71 ± 3.36	20.64 ± 6.66	38.86 ± 5.06	31.99 ± 5.48	37.31 ± 5.23	48.02 ± 7.73	61.94 ± 7.81
Pancreas	2.52 ± 0.64	0.23 ± 0.07	0.15 ± 0.04	1.29 ± 0.38	0.05 ± 0.02	0.26 ± 0.02	0.06 ± 0.03
Blood	40.83 ± 6.60	38.43 ± 9.91	23.45 ± 7.73	27.22 ± 5.71	19.54 ± 3.94	10.97 ± 3.80	7.48 ± 1.26

Figure 4.4: Organ level biodistribution. Bulk particle localization in the liver, spleen, and kidney was size dependent. Gold contents are normalized to percent injected dose (% ID). For all particle sizes, the five organs plus blood accounted for ≥70% ID of the injected dose. Error bars indicate one s.d. from each Au_x-PEG_y NP class (N = 3). The inset shows the magnification of the particle retention in the kidney. Exact values of blood particle concentration in all organs at 24 h are provided for added clarity.

time points to evaluate for gold content using inductively coupled plasma mass spectrometry (ICP-MS). With extensive surface engraftment of PEG ($y \geq 4000$), all particles manifested extended blood circulation with a half-life ($t_{1/2}$) that spans from 7 to 38 h (Fig. 4.3). Particle size and $t_{1/2}$ were inversely correlated (Table 4.2). The simultaneous increase in x and y led to reduction in $t_{1/2}$, indicating that size-dependent internal clearance, not colloidal stability conferred by PEGylation, played a dominant role in determining particle blood circulation.

Organ level distribution

Mice were then euthanized 24 h after injection to extract organs for detection of bulk gold content using ICP-MS. For all particle sizes, gold content of the six organs plus the blood samples collected at three time points summed up to ≥70% ID, thus constituting a mass balance that accounts for the destinations of most injected Au_x-PEG_y NPs. Overall, the liver, spleen, and kidney were the main sites of particle accumulation, whereas the lung, pancreas, and heart

NP	$t_{1/2}$ (h)	Ω (% ID)	GTE (%)	SI
Au$_5$-PEG$_{5K}$	48.9	0.2 ± 0.1	0	0
Au$_{20}$-PEG$_{5K}$	31.8	1.2 ± 0.5	50	+
Au$_{40}$-PEG$_{4K}$	13.8	3.0 ± 0.6	80	++
Au$_{50}$-PEG$_{5K}$	13.7	4.6 ± 0.9	100	+++
Au$_{60}$-PEG$_{7K}$	11.4	1.9 ± 0.4	90	+++
Au$_{80}$-PEG$_{10K}$	8.7	0.7 ± 0.4	70	++
Au$_{100}$-PEG$_{20K}$	6.8	0.5 ± 0.3	60	+

Table 4.2: In vivo characteristics of Au$_x$-PEG$_y$ NPs. $t_{1/2}$ = blood half-life; Ω = kidney bulk particle content; GTE = glomerular targeting efficiency; SI = staining index (an arbitrary score that ranks both the intensity and spread of the silver stain, whereby +++ and 0 are the maximum and minimum values, respectively). The table presents in vivo data as average s.d. from three animals per particle type.

showed negligible (<0.5% ID) particle retention (Fig. 4.4). At 24 h after dosing, the liver and spleen both showed a positive correlation between particle size and degree of particle uptake, in agreement with previous reports that the degree of particle phagocytosis by Kupffer cells and spleen macrophages is largely size-dependent (the larger the nanoparticles the greater the uptake in the reticuloendothelial system (RES)) [135]. From the data shown in Fig. 4.1-4.3, the blood nanoparticle content at 24 h appears to correlate with uptake by the RES (increased uptake by the RES is accompanied by lower content in the blood (leading to shorter circulation half-life)). Lastly and most importantly, the kidney revealed an unexpected size-dependent nanoparticle retention pattern: there exists a particle size (Au$_{50}$-PEG$_{5000}$) at which renal accumulation was maximal (Fig. 4.4).

Tissue level renal distribution

To understand the size-dependent accumulation in the kidney, we prepared "silver enhanced" kidney sections to reveal the distribution of Au$_x$-PEG$_y$ NPs at the tissue level. Gold selectively catalyzes the reduction of silver ions and deposition of metallic silver, making nanosized objects visible under light microscopy. Within the cortex, most particles accumulated either near resident phagocytes within peritubular capillaries, which intertwine the cortical tubules (proximal convoluted tubules and distal convoluted tubules), or inside renal corpuscles. Particle accumulation at peritubular capillaries did not show clear size correlation (Fig. 4.5).

Particle accumulation inside renal corpuscles reveals a strong function of size. The smallest particles (Au_5-PEG_{5000} NPs) were virtually undetectable in the renal corpuscles, but were found in peritubular capillaries (Fig. 4.6A). Au_{20}-PEG_{5000} NPs accumulated in the renal corpuscles and rarely in the peritubular capillaries (Fig. 4.6B). Only ~50% of the renal corpuscles contained Au_{20}-PEG_{5000} NPs, and the staining scattered all over the extracellular space (mesangium) outside the mesangial cells. The staining intensity appeared mild. For Au_{40}-PEG_{4000} NPs, staining within renal corpuscles became more intense. ~80% of the renal corpuscles were stained positive for particles and staining was closer to mesangial cells (not shown).

Similar accumulation patterns were apparent for Au_{50}-PEG_{5000} NPs, except that 100% of the renal corpuscles examined under the light microscope were stained positive for particles. Closer inspection of each individiual renal corpuscle reveals the most intense silver staining near mesangial cells in the largest areal fraction of the renal corpuscles among all particle sizes (Fig. 4.6C). Incidentally, this complete glomerular targeting efficiency (GTE) matches strongly with the maximal bulk particle content in the kidney observed for Au_{50}-PEG_{5000} NPs (Fig. 4.4). Likewise, the GTE for Au_{60}-PEG_{7000} NPs were close to complete (~90%), and such particles elicited very intense silver staining near the mesangial cells (Fig. 4.7A).

Au_{80}-PEG_{10000} and Au_{100}-PEG_{20000} NPs gave a GTE of 60-70%. Due to the catalytic nature of staining, larger Au_x-PEG_y NPs are expected to produce more surface silver deposition. While silver staining can confirm the presence of Au_x-PEG_y NPs, the intensity alone does not provide quantitation of actual particle content. Besides intensity, the spread of staining (areal fraction covered by silver) within the renal corpuscles is also an important measure.

We report in Table 4.2 what we denote as the "staining index (SI)," an arbitrary measure that accounts for both intensity and spread of staining. For the highest score (i.e., +++), particles (like Au_{50}-PEG_{5000} NPs) accumulated in the highest areal fraction of the renal corpuscles, and

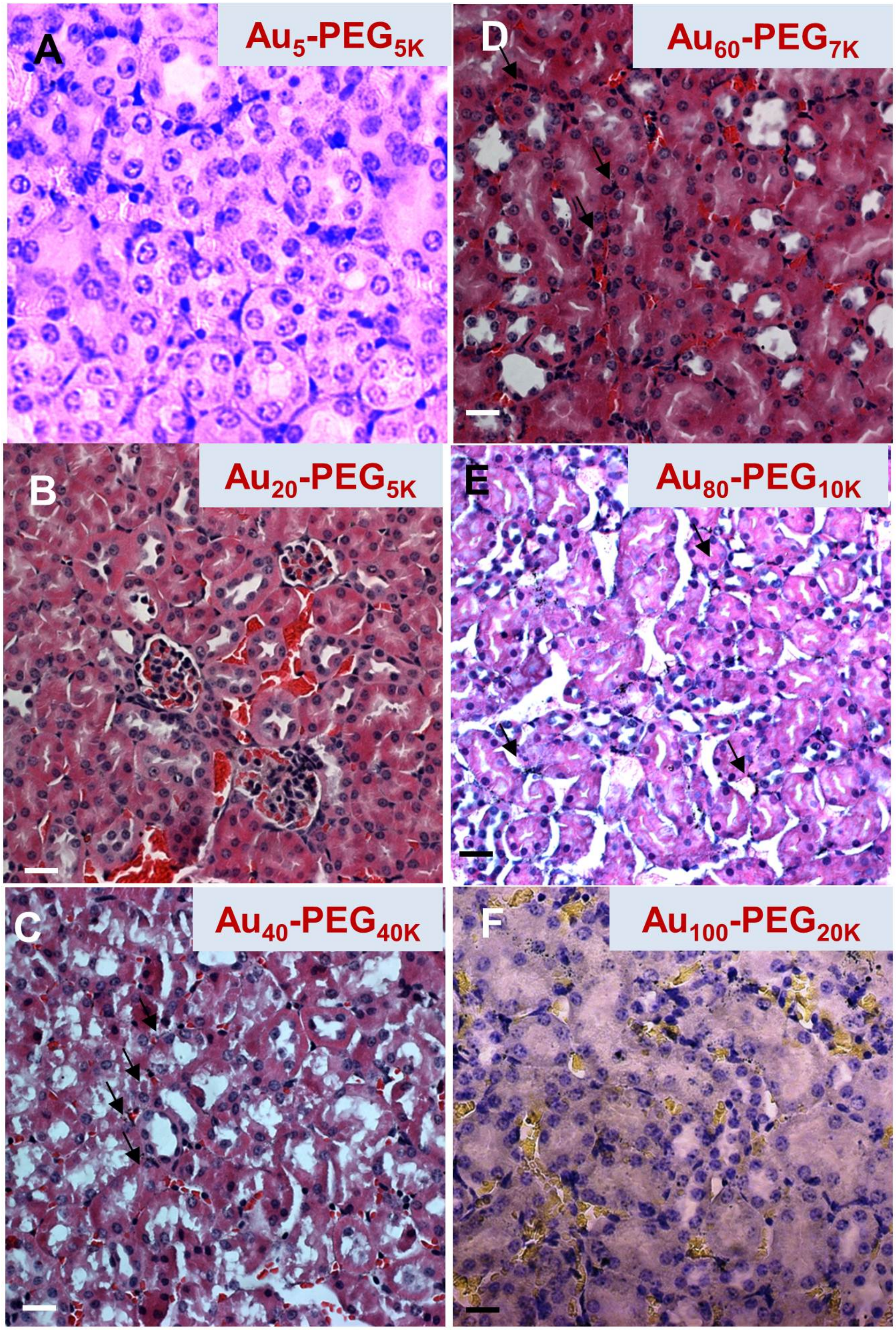

Figure 4.5: Tissue level distribution in peritubular tubules. The deposition of Au$_x$-PEG$_y$ NPs in the cortex excluding renal corpuscles is not a function of particle size. Particles (black arrows) are located near peritubular capillaries or in the connective tissue space between adjacent convoluted tubule cells. Scale bar = 20 μm.

also at the highest intensity. Typically, the same particles can achieve a high GTE, meaning that they can be found frequently in different renal corpuscles throughout the cortex. For the lowest score (i.e., 0), particles (like Au_5-PEG_{5000} NPs) resided in limited areas of the renal corpuscles, and usually at undetectable densities. Typically, the same particles can achieve a low GTE, implying their low occurrence in different renal corpuscles throughout the cortex.

For Au_{80}-PEG_{10000} NPs, silver staining was found in limited regions of renal corpuscles, despite their intense staining, yielding an SI score of ++. The largest particles, Au_{100}-PEG_{20000} NPs, barely occupied a sizeable areal fraction of the renal corpuscles, and was accompanied by very modest staining, leading to their score of + for the SI. Overall, the staining index of the largest nanoparticles was lower than that of Au_{50}-PEG_{5000} NPs. Taken together, Au_{80}-PEG_{10000} and Au_{100}-PEG_{20000} NPs target 60-70% of the renal corpuscles, and within each corpuscle, a very limited area fraction and moderately intense staining.

The histological data collectively suggest a size-dependent localization of Au_x-PEG_y NPs within renal corpuscles in the kidney cortex. Because such particles do not have a constant PEG chain length, one may question whether the distribution of nanoparticles in renal corpuscles is PEG-dependent. To address this point, we investigated the tissue level in vivo distribution of Au_{80}-PEG_{5000} NPs (hydrodynamic size: 97.1 ± 1.9 nm; zeta potential: -16.77 ± 1.14 mV) in renal corpuscles, noting that such particles possess a very similar hydrodynamic size of Au_{60}-PEG_{7000} NPs. Histological analysis reveals accumulation of Au_{80}-PEG_{5000} NPs in the renal corpuscles in similar intensity and area as that of Au_{60}-PEG_{7000} NPs but not Au_{80}-PEG_{10000} NPs, supporting that the distribution of nanoparticles in renal corpuscles is size-dependent.

Cellular level renal distribution

We employed transmission electron microscopy (TEM) to determine the intracellular localization patterns of the nanoparticles residing in the renal cortex. In agreement with the histological data,

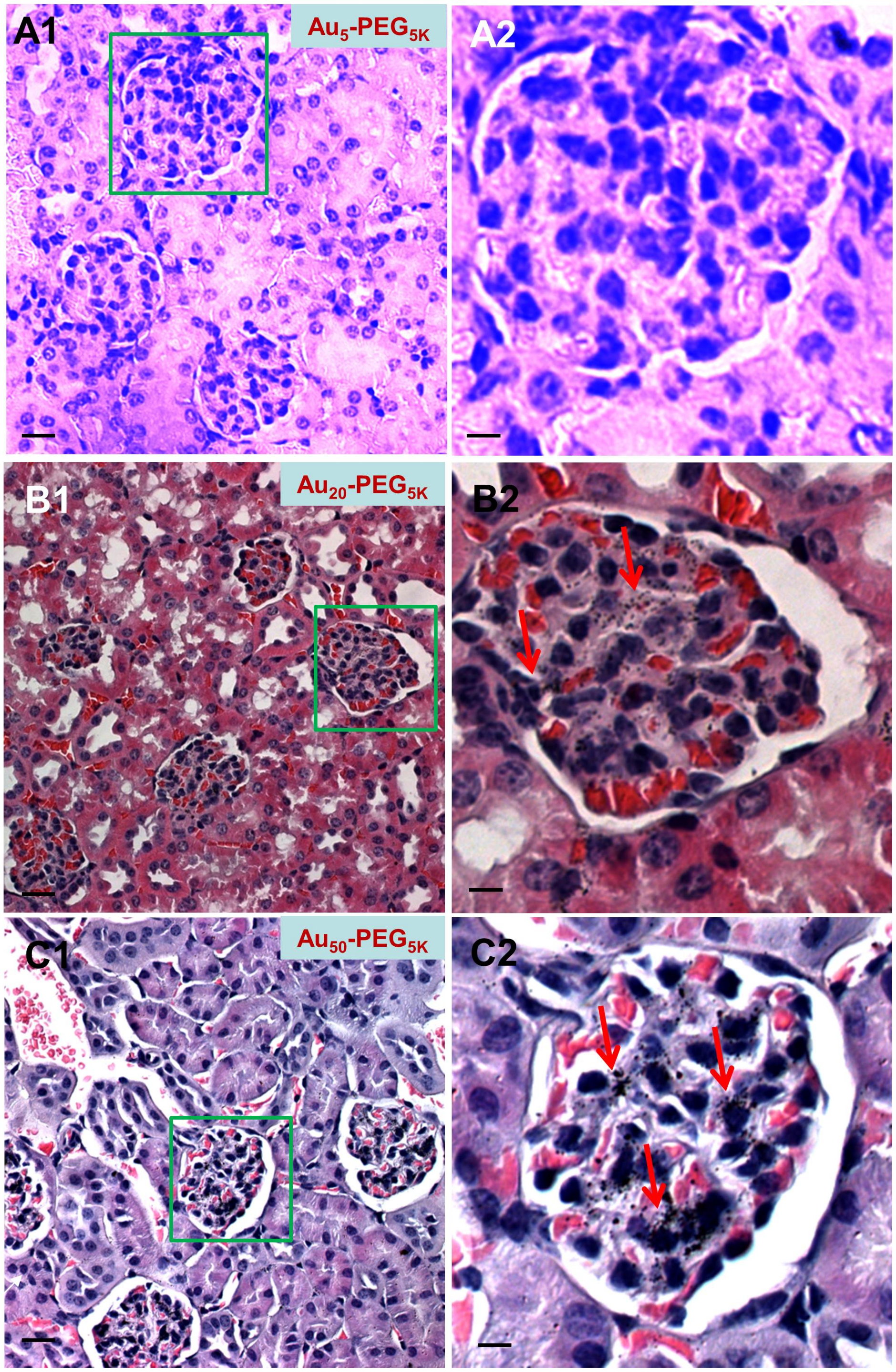

Figure 4.6: Tissue level distribution in renal corpuscles. Representative light micrographs of "silver-enhanced" kidney sections reveal size-dependent particle accumulation. (A) Au$_5$-PEG$_{5000}$ NPs were almost undetectable. (B) Au$_{20}$-PEG$_{5000}$ NPs exhibited weak silver staining in limited areas of the renal corpuscles. (C) Au$_{50}$-PEG$_{5000}$ NPs displayed the most intense staining in the largest area of renal corpuscles among all particle sizes. Silver staining (dark specks indicated by red arrows) was present in almost every renal corpuscle observed under the light microscope, resulting in complete glomerular targeting. The right column (scale bar = 3 µm) illustrates the magnified renal corpuscle (green box) shown in the left column (scale bar = 10 µm).

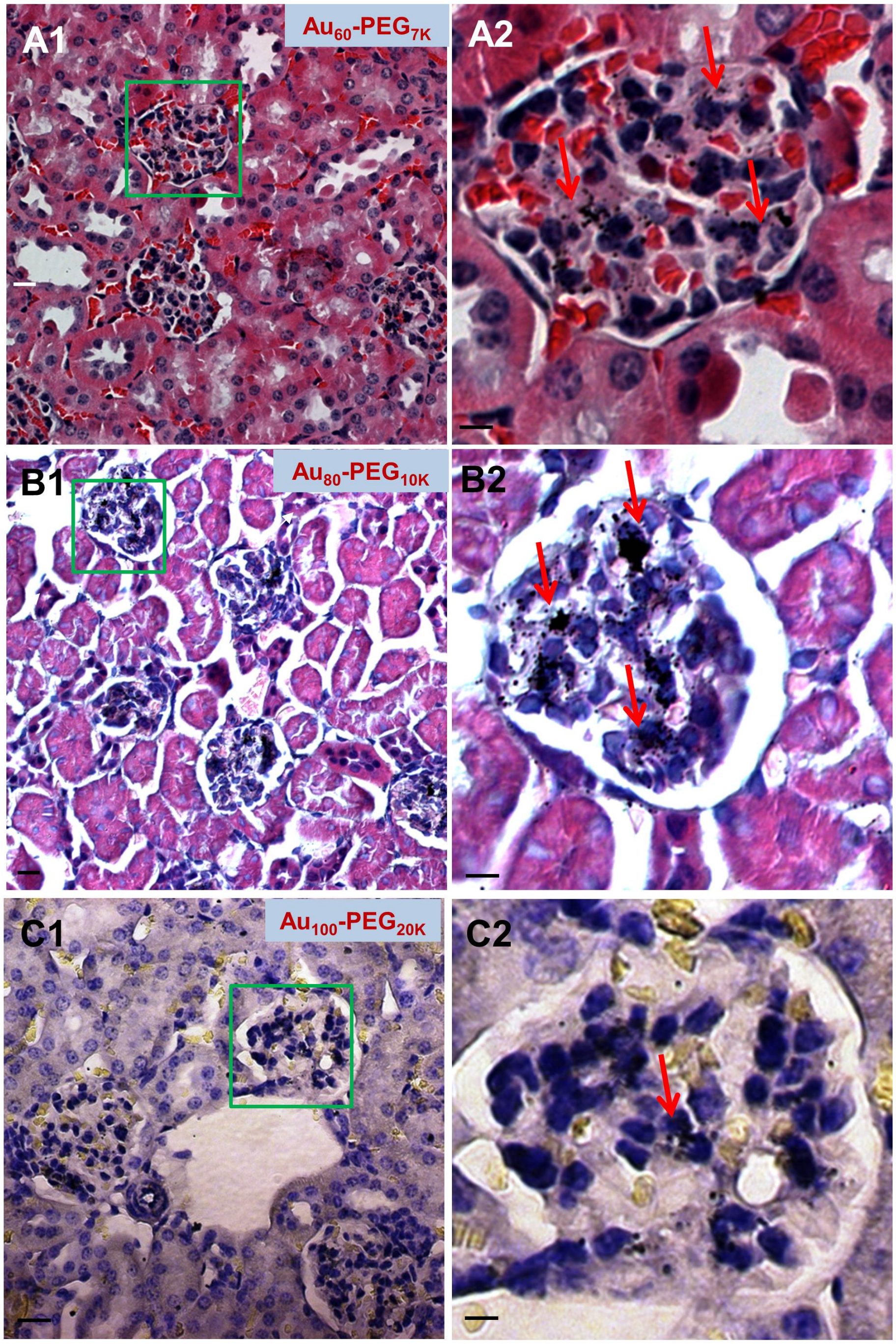

Figure 4.7: Tissue level distribution in renal corpuscles (continued). Representative light micrographs of "silver-enhanced" kidney sections reveal size-dependent particle accumulation. (A) Au_{60}-PEG_{7000} NPs displayed the most intense staining in the largest area of renal corpuscles among all particle sizes. Silver staining (dark specks indicated by red arrows) was present in almost every renal corpuscle observed under the light microscope, resulting in complete glomerular targeting. (B) Au_{80}-PEG_{10000} NPs appeared in reduced amounts with moderate intensity. (C) Au_{100}-PEG_{20000} NPs accumulated in the renal corpuscles in minute amounts and very weak intensity, presumably due to their inability to penetrate through the fenestrated glomerular endothelium. The right column (scale bar = 3 µm) illustrates the magnified renal corpuscle (green box) shown in the left column (scale bar = 10 µm).

particles of all sizes were either engulfed by resident phagocytes or remained as isolated entities in circulation inside pertitubular blood capillaries. Particle accumulation in peritubular blood capillaries was not size-dependent (Fig. 4.8).

Retention of particles in renal corpuscles, however, is a strong function of size (Fig. 4.9). Smaller particles (Au_{20}-PEG_{5000} NPs) entered the mesangium within renal corpuscles in minute quantities (Fig. 4.9A). As size increases, Au_x-PEG_y NPs showed more association with mesangial cells. Au_{50}-PEG_{5000} NPs accumulated in multiple clusters either within mesangial cells or in the extracellular matrix outside mesangial cells. The clustering density was the most pronounced among all particle sizes, consistent with the histological data (Figs. 4.9C and 4.10A). Particles of similar sizes (Au_{40}-PEG_{4000} (Fig. 4.9B) and Au_{60}-PEG_{7000} NPs (Fig. 4.10B)) also demonstrated appreciable particle accumulation in the mesangium. Larger particles (Au_{80}-PEG_{10000} NPs) only resided at the extracellular space in isolated amounts, but never inside the mesangial cells (Fig. 4.10C). The TEM data reveal a size at which particle association with mesangial cells was maximal (Au_{50}-PEG_{5000} NPs). This particular size maximized bulk kidney particle content and glomerular targeting. Thus, **the size of Au_{50}-PEG_{5000} NPs yields maximal kidney targeting at the organ, tissue, and cellular (mesangium) levels**.

Interpretation of maximal kidney targeting

The average pore diameter of the fenestrated glomerular endothelia is reported to be 80-100 nm, roughly the hydrodynamic size of Au_{50}-PEG_{5000} and Au_{60}-PEG_{7000} NPs. Particles larger than this size cutoff (Au_{80}-PEG_{10000} and Au_{100}-PEG_{20000} NPs) may experience steric hindrance when permeating through the pores to enter the mesangium and access the mesangial cells. On the contrary, smaller particles (Au_{20}-PEG_{5000} and Au_{40}-PEG_{4000} NPs) are freely accessible to the mesangium. Thus, the "size exclusion" effect may account for the lower kidney particle content and weaker glomerular targeting of the largest particles.

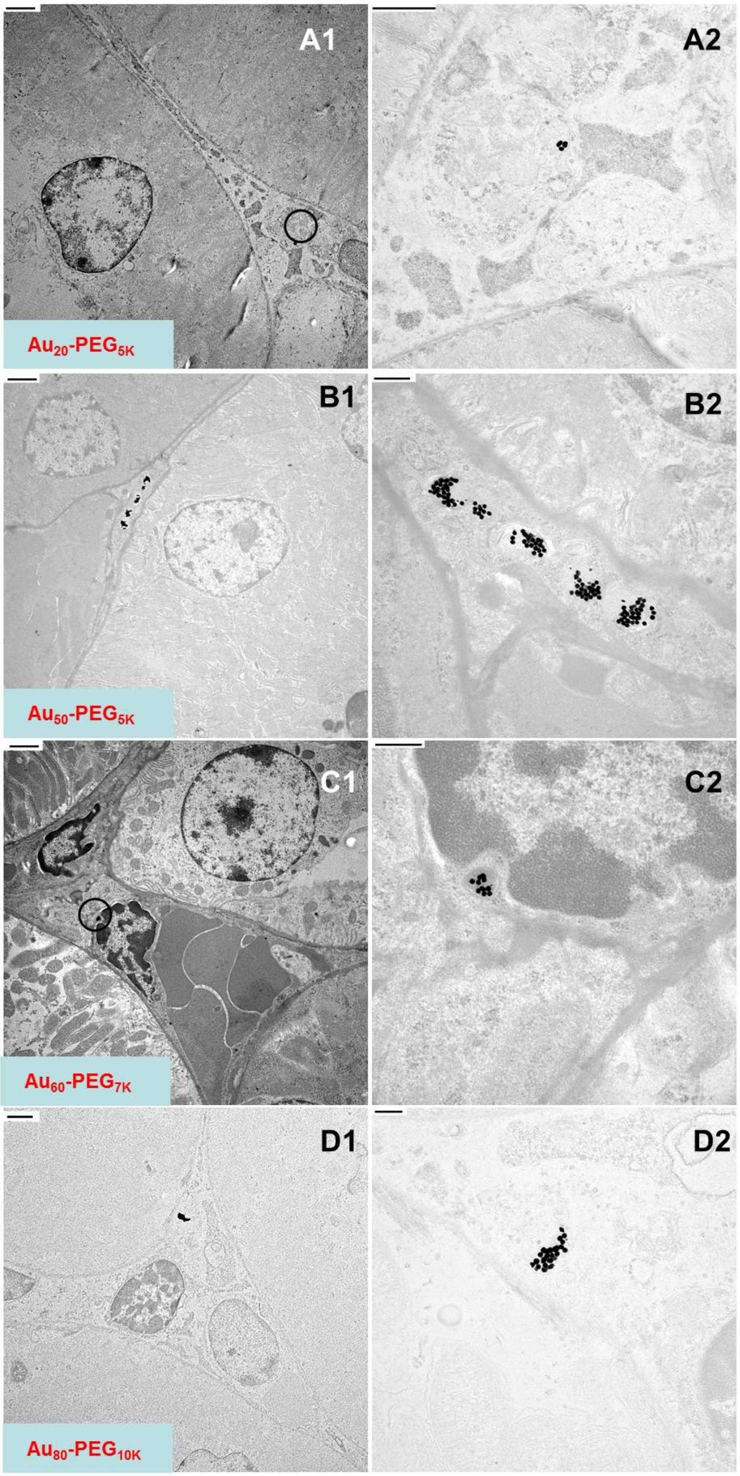

Figure 4.8: Cellular level distribution in peritubular capillaries. Representative TEM micrcraphs show that particle deposition in the cortex excluding renal corpuscles is not a function of particle size. Particles are located near peritubular capillaries or in the connective tissue space between convoluted tubule cells. Images shown in the 2nd column (scale bar = 500 nm) are magnified versions of those shown in the 1st column (scale bar = 2 μm).

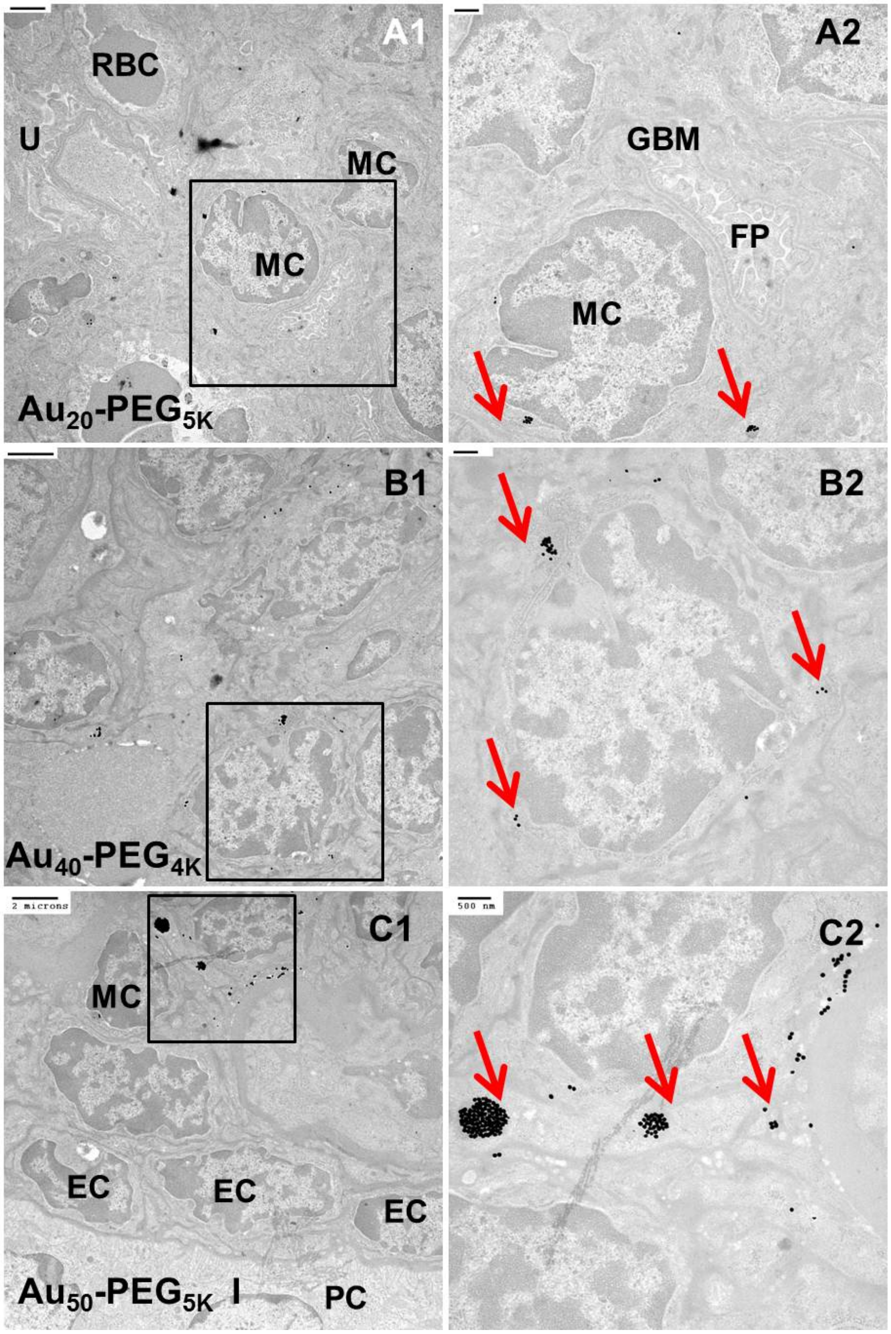

Figure 4.9: Cellular level distribution in renal corpuscles. Representative TEM micrographs show particle accumulation in the mesangium (mesangial cells and extracellular matrix). (A-B) A small portion of Au$_{20}$-PEG$_{5000}$ and Au$_{40}$-PEG$_{4000}$ NPs localized in mesangial cells within the renal corpuscles. (C) Au$_{50}$-PEG$_{5000}$ experienced the most prominent uptake by mesangial cells among all particle sizes. TEM micrographs clearly depict the mesangial location in the vicinity of the glomerular filtration apparatus, including glomerular filtration membrane (GBM) and podocytes. Images shown in the 2nd column (scale bar = 500 nm) illustrates the magnified portion (black box) shown in the 1st column (scale bar = 2 µm). Red arrows in the right column indicate clusters of Au$_x$-PEG$_y$ NPs. Legend: red blood cell (RBC), mesangial cells (MC), foot processes of podocytes (FP), urinary space (U), endothelial cell (EC).

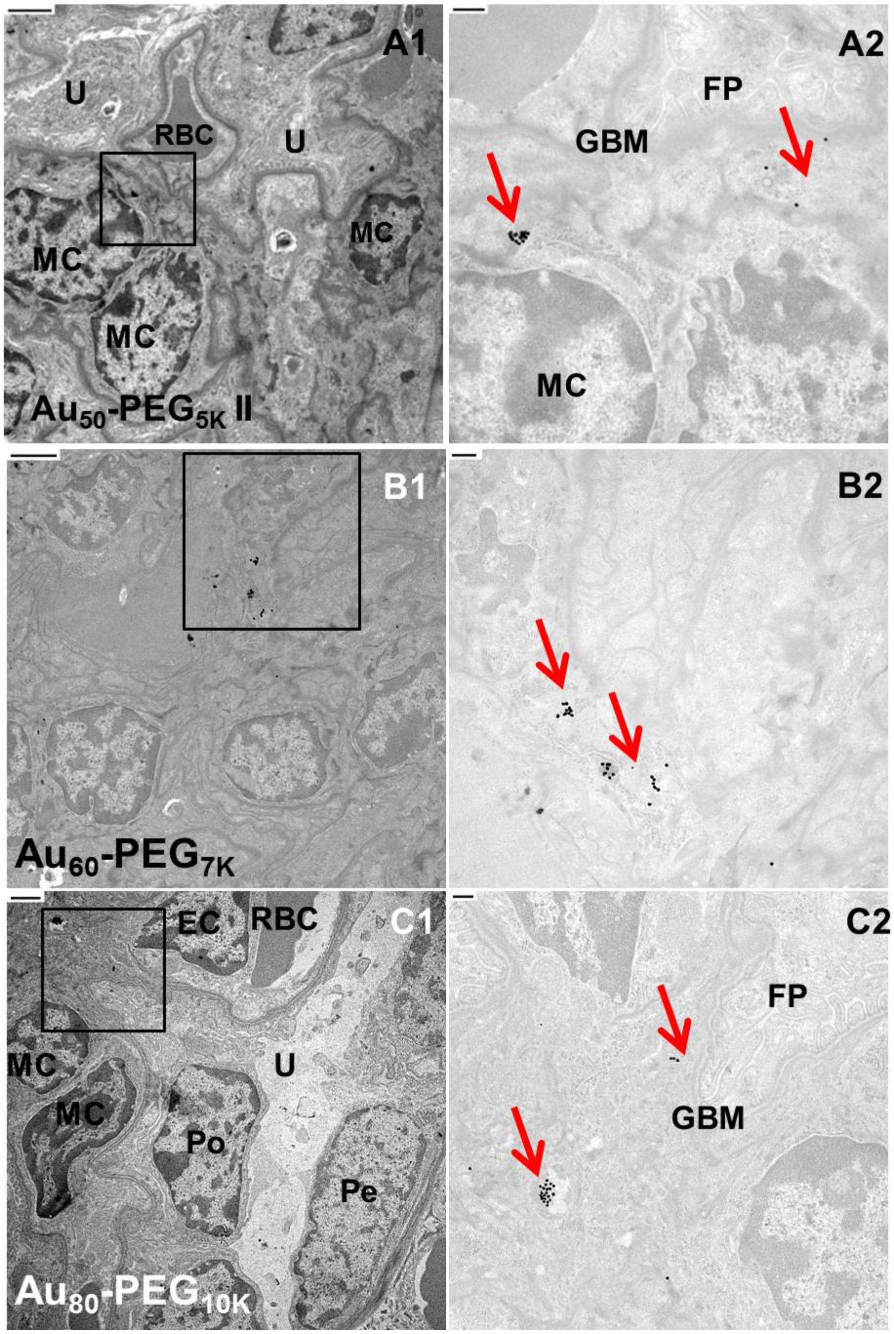

Figure 4.10: Cellular level distribution in renal corpuscles (continued). Representative TEM micrographs show particle accumulation in the mesangium (mesangial cells and extracellular matrix). (A-B) Au_{50}-PEG_{5000} and Au_{60}-PEG_{7000} NPs experienced the most prominent uptake by mesangial cells among all particle sizes. (C) Au_{80}-PEG_{10000} NPs deposited in the mesangium in drastically reduced amounts. TEM micrographs clearly depict the mesangial location in the vicinity of the glomerular filtration apparatus, including glomerular filtration membrane and podocytes. Images shown in the 2nd column (scale bar = 500 nm) illustrates the magnified portion (black box) shown in the 1st column (scale bar = 2 µm). Red arrows in the right column indicate clusters of Au_x-PEG_y NPs. Legend: red blood cell (RBC), mesangial cells (MC), podocyte (Po), foot processes of podocytes (FP), urinary space (U), glomerular basement membrane (GBM), pericyte of Bowman's capsule (Pe), proximal convoluted tubule (PC).

From TEM data, size-dependent uptake occurs solely at mesangial cells, which come in two types. The first type is contractile mesangial cells, which resemble vascular smooth muscle cells and fibroblasts that regulate surface area for glomerular filtration of fluids and mesangial volume. The second type involves mononuclear resident phagocytes derived from the bone marrow [128]. From the ICP-MS data, particle uptake by spleen macrophages and hepatic Kupffer cells (both of bone marrow origin) rise with increasing particle size. Below the size cutoff in the kidney, larger particles (Au_{50}-PEG_{5000} NPs) can penetrate through the endothelial pores, enter the mesangium, and accumulate inside mesangial cells (likely the phagocytic type resident macrophages). Smallest particles (Au_5-PEG_{5000} NPs) may transiently enter the mesangium, but may not favor prolonged retention due to lack of phagocytosis by mesangial cells. The absence of a cellular sink may lead to their low bulk particle content.

4.4 Conclusion

This work is the first study to systematically examine the distribution of 10-150 nm nanoparticles in the kidney from a systemic injection. From measuring blood pharmacokinetics as well as distribution patterns at the organ, tissue, and cellular levels, the results suggest that there is an optimal size range (Au_{50}-PEG_{5000} NPs) that maximizes bulk particle uptake in the kidney, deposition of particles in renal corpuscles within the cortex, and uptake of particles by mesangial cells within renal corpuscles. When using nanoparticles as cancer therapeutics, accumulations in single digit percent ID amounts in the tumor can lead to gene inhibition and tumor reduction [146]. Thus, the accumulation of Au_x-PEG_y NPs (1-5% ID) in the kidney at these amounts may be able to impart efficacy with kidney diseases.

Moreover, the lack of significant localization of residual (0.7% ID) of larger particles (Au_{80}-PEG_{10000} NPs; ~130 nm in diameter) provides an in vivo calibration to the size of the glomerular

x (nm)	β (oligos/nm^2)	Σ (PEG/nm^2)	σ^*
20	1.4×10^{13}	0.400	0.196
40	8.5×10^{12}	0.243	0.119
50	8.1×10^{12}	0.231	0.113
60	7.8×10^{12}	0.223	0.109
80	7.1×10^{12}	0.203	0.099

Table 4.3: Rough estimates of PEG grafting density on Au$_x$-PEG$_y$ NPs. β = oligonucleotide grafting density (all entries referenced from Hill et al.); Σ = PEG grafting density (with the first entry (0.4) by Takae et al. and all remaining entries scaled according to β); $\sigma^* = b^2\Sigma$ = dimensionless PEG grafting density (with the first entry (0.196) determined above and all remaining entries scaled according to Σ.)

endothelial pores. Most reported values for this pore size are derived from direct measurements of TEM and SEM images. Sample processing for microscopy involves repeated dehydration, and may lead to shrinkage of fine cellular features. The pore size reported here (130 nm) depicts the glomerular endothelial morphology at physiologically relevant conditions.

4.5 Supporting Information

PEG corona thickness of Au$_x$-PEG$_y$ NPs

Each Au$_{20}$ NP can anchor 520 PEG chains of 6000 Da each [172]. This translates to a PEG grafting density (Σ) of 0.4 PEG/nm^2. The Kuhn length (b) of PEG is 0.7 nm. The dimensionless PEG grafting density (σ^*) is $\sigma^* = b^2\Sigma = (0.7\text{ nm})^2 \times (0.4\text{ PEG/nm}^2) = 0.196$. Hill et al. [173] evaluated the grafting density of oligonucleotides (β) on submicron-sized AuNPs (10-100 nm). If the oligonucleotide density data due to size curvature are applicable to the study of PEG grafting, a rough estimate of PEG grafting density of Au$_x$-PEG$_y$ NPs can be made (Table 4.3).

σ^* is ~0.1-0.2 (for AuNPs with size >20 nm), which represents a very high grafting density according to Wijman and Zhulina [174]. Physically, how high is this density? According to scaling analysis by de Gennes on grafted polymers, the brush conformation appears if $\sigma^* > N^{-6/5}$, where N is the number of Kuhn polymer segments [110]. How can we estimate N?

Take Au$_{50}$-PEG$_{5000}$ NPs as an example. The MW of each PEG unit is 44 g/mol. The two

	Au_{40}-PEG_{4K}	Au_{50}-PEG_{5K}	Au_{60}-PEG_{7K}	Au_{80}-PEG_{10K}
MW (g/mol)	4000	5000	7000	10000
R_{max} (nm)	40	50	70	100
N	57.14	71.43	100	142.86
$N^{-6/5}$	0.0078	0.0060	0.0040	0.0026
R_F (nm)	7.93	9.07	11.09	13.74
D (nm)	2.29	2.35	2.39	2.50
x (nm)	40	50	60	80
$x/2b$	28.57	35.71	42.86	57.14

Table 4.4: Polymer parameters of grafted PEG. MW = molecular weight of grafted PEG; $R_{max} = bN$ = contour length; N = degree of polymerization (no. of Kuhn segments); $R_F = bN^{3/5}$ = Flory radius in a good solvent; D = separation distance between adjacent PEG monomers

C-O bonds (each 0.145 nm) and C-C bond (0.15 nm) add up to 0.44 nm. The contour length ($R_{max} = Nb$) of a fully stretched PEG5000 coil is 5000 ÷ 44 × 0.44 nm = 50 nm. If $b = 0.7$ nm, then $N = 71.4$. Clearly, σ^* is greater than $N^{-6/5}$. Hence, PEG polymer chains fill are overlapping with each other, with their blobs acting as hard spheres and cover the gold surface densely. The $\sigma^* > N^{-6/5}$ result is also apparent for all other Au_x-PEG_y NPs.

Alternatively, one can calculate the footprint (D) of each PEG chain (separation distance between each adjacent PEG chain) on the gold surface, knowing that $4\pi D^2 = \Sigma$. For Au_{50}-PEG_{5000} NPs, $D = 2.29$ nm, which is shorter than the Flory radius of PEG_{5000} in a good solvent ($R_F = bN^{3/5} = 9.07$ nm). Because the $R_F > D$ result is apparent for all other Au_x-PEG_y NPs, the grafted PEG chains take the "brush conformation" on the gold surface for all particle sizes.

On a planar surface, the brush height of tethered PEG corona (H) should scale linearly with N [110] [109]. Yet, on a spherical interface, $H \sim N^{3/5}$ because the chains extended away from the surface should be more diffuse compared to those densely packed chains near the surface, thus shortening H. Yet, DLS measurements revealed $H \sim N$ (Table 4.1), not $N^{3/5}$, suggesting that the curvature effect on H is not eminent.

For $\sigma^* \sim 0.1$ and using self-consistence-field simulations, Dan and Tirrell [114] showed that the curvature effect becomes less important, and that H will approach the planar limit of ($H \sim N$) when $x/2b > 100$. For Au_x-PEG_y NPs at hand, their values of $x/2b$ mainly lie in the range of

28-57 (Table 4.4), so $H \sim N^{0.9}$ according to simulation results by Dan and Tirrell. This explains the observed approximate "linearity" between H and N even on spherical particles.

4.6 Materials and Methods

General

Unless otherwise mentioned, all poly (ethylene glycol) (PEG) raw materials were purchased from Laysan Bio. All organic solvents were purchased from Sigma.

Synthesis of mPEG$_{4000}$-SH and mPEG$_{7000}$-SH

50 mg of amine-PEG$_{3400}$-SH (14.7 µmol) was reacted with 40.4 mg of methoxy-PEG$_{550}$-(succinimidyl propionate) (73.5 µmol) in 50 µL of triethylamine (TEA) and 1.2 mL of anhydrous dichloromethane (DCM) at RT with stirring for 7 h. The crude mixture was dried under vacuuo, and dialyzed against deionized water using a 3 kDa Amicon MWCO membrane (Millipore) three times. 15 mg of amine-PEG$_{5000}$-SH (3.0 µmol) was reacted with 60 mg of methoxy-PEG$_{2000}$-(succinimidyl valerate) (30.0 µmol) in 50 µL of TEA and 1.2 mL of anhydrous DCM at RT with stirring for 16 h. The crude mixture was dried under vacuuo, and dialyzed against deionized water using a 30 kDa Amicon MWCO membrane (Millipore) three times. The correct fraction (7000 Da) was separated using HPLC using a TSKgel G3000SW column (Tosoh Bioscience). Final molecular weights were confirmed by MALDI-TOF.

Assembly of PEGylated gold nanoparticles (Au$_x$-PEG$_y$ NPs)

Methoxy-PEG-thiol (purchased or synthesized above) of a certain molecular weight (y = 4000, 5000, 7000, 10000, and 20000), dissolved in deionized water was added to 3 mL of aqueous suspension of unconjugated gold colloids (Ted Pella) of a designated core size (x = 5, 20, 40, 50, 60, 80, and 100 nm) at an excess concentration of ∼9 PEG strands per nm^2 of gold surface. E.g., To ensure complete coverage, PEGylation of Au$_{50}$ NPs required the addition of 10 µL of 1 mM mPEG$_{5000}$-thiol (in deionized water) to 0.5 mL of aqueous suspension of 2.25×10^{10} particles. All PEGylation reactions proceeded at RT for 2 h with constant stirring. To remove any unbound PEG, the reaction mixture was dialyzed against deionized water using a 30 or 100 kDa Amicon MWCO membrane (Millipore) three times.

Animal experiments

For each type of Au_x-PEG_y NPs, three 9-week, female Balb/c mice (Jackson Laboratory) received i.v. injections of particles via the tail vein at a concentration of 4.5×10^{11} particles per mL, formulated in 120 µL of filtered D5W. At three consecutive time points after injection (0.5, 4, and 24 h), 30 µL of mouse blood was drawn from each mouse via its saphenous vein using a Microvette CB 300 Capillary Blood Collection Tube with EDTA (Sarstedt). Blood samples were stored at 4 °C until use. After 24 h, mice were euthanized by CO_2 overdose for the collection of the liver, kidney, lung, heart, spleen, and pancreas. Organs were fixed in 4% PFA in 1× PBS for 3 d.

Organ level particle distribution

All excised organs underwent routine ICP-MS procedures for quantification of gold contact (see Appendix A). Each mouse weighed ~20 g at the time of experiment, and had a total blood volume of 1.6 mL (average mouse volume is 77-80 µL/g).

Quantitative tissue level renal particle distribution

Fixed kidney blocks underwent routine histological procedures with silver enhancement (see Appendix A) to generate silver enhanced, H & E counterstained sections. To estimate the glomerular targeting efficiency (GTE) of particles to renal corpuscles from light micrographs, 300 renal corpuscles, selected at random positions from 10 to 15 kidney sections per injected mouse, were inspected visually for the presence of silver stains. For the staining index (SI), both the staining intensity and spread of these 300 renal corpuscles were scored.

Chapter 5

Development of Chemical Stain for Cyclodextrin-based Nanoparticles

5.1 Abstract

Cyclodextrin-polymer (CDP) nanoparticles represent a class of delivery vehicle with widespread biomedical applications, owing to its low toxicity, high aqueous solubility, and superior ability to imbibe hydrophobic moieties (drug payload). Tracking the localization patterns of CDP nanoparticles at the tissue and cellular levels can provide valuable information of their in vivo behavior. Here, we report the creation of a new chemical stain that can specifically recognize CDP nanoparticles embedded in cells, tissue sections, and patient biopsies, ex vivo. Based on an aqueous suspension of monodisperse Au_5-PEG_{1000} nanoparticles, this stain exhibits superior binding to the adamantane cups exposed on the periphery of CDP nanoparticles, fluorescence for detection by confocal microscopy, as well as steric stability against salt-induced aggregation in PBS. This chapter concludes with different applications of this stain to reveal key pharmacological insights (e.g., intratumoral transport and dose response) of two classes of CDP nanoparticles currently under clinical development (IT-101 and CALAA-01).

Excerpts of this chapter are reproduced with permission from "Pharmacokinetics and tumor dynamics of the nanoparticle IT-101 from PET imaging and tumor histological measurements." Thomas Schluep, Jungyeon Hwang, Isabel J. Hildebrandt, Johannes Czernin, Chung Hang J. Choi, Christopher A. Alabi, Brendan C. Mack, and Mark E. Davis. *Proc. Natl. Acad. Sci. USA.* **106**, 27, 11394-11399 (2009). and "Evidence of RNAi in humans from systemically administered siRNA via targeted nanoparticles." Mark E. Davis, Jonathan E. Zuckerman, Chung Hang J. Choi, David Seligson, Anthony Tolcher, Christopher A. Alabi, Yun Yen, Jeremy D. Heidel, and Antoni Ribas. *Nature* **464**, 7291, 1067-1070 (2010).

5.2 Introduction

There are many important measures to ascertain the efficacy of nanoparticle-based therapeutics for cancer applications. After their administration, do the nanoparticles accumulate in the tumor? If so, will they enter the cancer cells within the tumor? Presumably they arrive at the specific cancer cells, can they release the drug payload? And can the payload lead to obvious reduction or stabilization of tumor growth? If so, is such growth reduction due to the mechanism of action originally proposed for the therapeutic?

Efficient delivery of nanoparticles must take place before the encapulated drug can demonstrate its mechanism of action. When experimental data from molecular biological analysis (e.g., knockdown of target gene, attenuation of protein expression) can be subject to interpretation, microscopic evidence that illustrates the presence of the administered nanoparticles within the tumor is more objective, and can often lend confidence to the molecular biological data (especially when the tumor does not show obvious regression). Thus, developing tools that can reveal injected nanoparticles within tumor tissues is of much scientific and clinical merit.

This chapter features the development of a chemical stain for the specific detection of cyclodextrin-based polymer nanoparticles. We elucidate the utility of this stain in revealing key pharmacological insights of nanoparticle-based drug delivery vehicles, such as transport phenomena and dosage. While positron emission tomography or near-infrared imaging can provide live imaging data, they can only provide organ-level distribution data but no information about the spatial relationship between these particles and their surrounding tissues or cells (e.g., intracellular accumulation). The lack in tissue- and cellular-level resolution motivates us to create a new stain for CDP nanoparticles in cells, tissue sections, and patient biopsies, ex vivo.

Cyclodextrin-based pharmaceutics

Cyclodextrins (CDs) represent a series of cyclic oligosaccharides. Each CD molecule adopts an interesting three-dimensional structure that resembles as a cone-shaped cup. The interior of the cup is relatively apolar, but its surface displays multiple hydroxyl groups that render its high water solubility. Also, they lack immunogenicity and are not prone to enzymatic digestion. In light of these properties, CDs can incorporate hydrophobic moieties within their cups and form CD inclusion complexes with high solublility in aqueous media, thus explaining their widespread application as building blocks of macromolecular vehicles for drug delivery [175] [176].

Cyclodextrin-polymer nanoparticles

Davis and co-workers developed two drug delivery platforms by employing linear polymer chains that contain β-CD (with 7 glucose monomers in its cyclic structure) as the backbone. In aqueous environments, both platforms can form nanosized inclusion complexes.

The first type of conjugate consists of repeating units of β-CD and PEG as the polymer backbone, grafted with camptothecin (CPT) as the active ingredient on their pendant chains [177]. CPT, a hydrophobic molecule, can recognize the apolar cups of CDs on the polymer backbone to trigger the self-assembly into a nanoparticle named IT-101. CPT is a potent antineoplastic agent against many different cancer cell types [178], but suffers from poor solubility, severe toxicity, and low clinical activity [179]. Compared to free CPT at equivalent doses, binding CPT with the CDP-based backbone dramatically enhanced the plasma half-life and net retention in the tumor resulting from an i.v. injection in animal models [180]. IT-101 has also demonstrated high tolerability and antitumor activity against a broad range of tumors in mice [181], and is now in clinical development for treatment of cancer [182].

The second type comprises repeating units of β-CD and a short cationic linker as the polymer backbone, non-covalently decorated by PEG-adamantane (for stability against salt-induced aggregation) and Tf-PEG-adamantane (for targeting tumor cells that overexpress Tf receptors) [160]. The cationic polymer serves to condense strands of small interfering ribonucleic acid (siRNA) molecules (effectors of the natural post-transcriptional gene silencing mechanism called RNA interference (RNAi)), the main therapeutic agent, and to protect siRNA from serum degradation. These nanoparticles contain siRNAs that target the M2 subunit of ribonucleotide reductase (RRM2), a crucial enzyme involved in preparing nucleotides for DNA replication. The specific sequence (denoted as siR2B+5) [183] can reduce the expression of RRM2, an anti-cancer target protein [184]. In aqueous medium, the combination of electrostatic (between the cationic CDP and siRNA) as well as hydrophobic foces (between adamantane and CD cups on CDP backbone) drives the self-assembly of these ingredients into stable nanoparticles of $\sim$70 nm in diameter (denoted as CALAA-01) [185]. Well tolerated in multi-dosing studies in non-human primates [186], CALAA-01 is now in use as part of the first ever human clinical trial to systemically deliver siRNA with a targeted delivery system to patients with solid cancer [187].

5.3 Results and Discussion

Design of chemical stain

To identify the presence of cyclodextrin-containing nanoparticles in tissues, the desirable stain should possess two properties. It should be detectable by conventional imaging modalities, and specifically bind to cyclodextrin-containing nanoparticles (or their fragments). To satisfy both properties, we coated AuNPs of 5 nm in diameter with thiolated PEG chains (methoxy-PEG$_{1000}$-SH). Some PEG chains contain adamantane (AD) moieties at their distal ends (Fig. 5.1).

Surface modification with gold-sulfur covalent linkages (Au-S) has been shown to yield the most significant enhancement in fluorescence signals of 5 nm AuNPs compared to their uncapped counterparts [188]. Surface Au(I) atoms and their coordinated ligands can engage in metal-

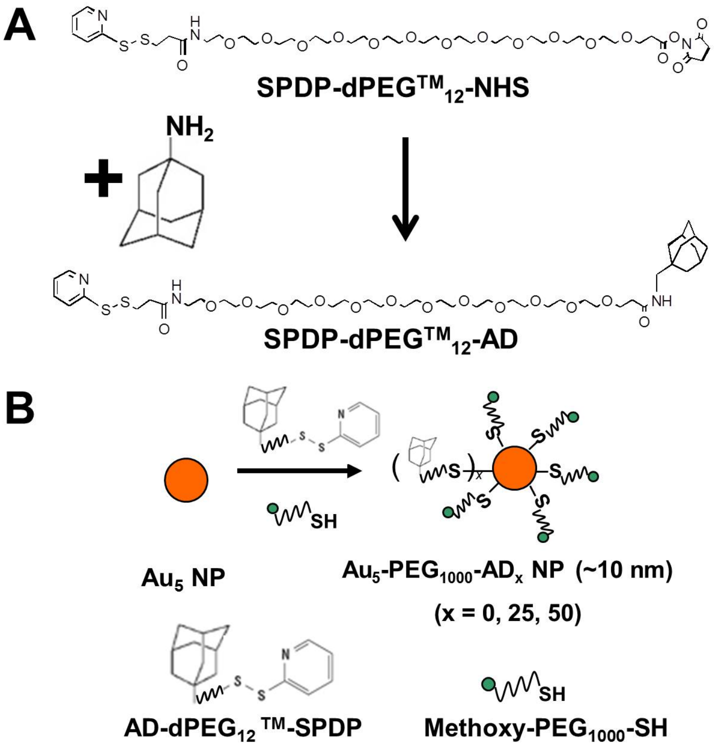

Figure 5.1: Synthesis of chemical stain. (A) Synthesis of AD-dPEG$_{12}^{TM}$-SPDP (MW: 1000). The adamantane (AD) residue was inserted to one end of a short, heterofunctional PEG linker. (B) Assembly of Au-PEG-AD. Different molar ratios of methoxy-PEG$_{1000}$-SH and AD-dPEG$_{12}^{TM}$-SPDP are added to an aqueous suspension of 5 nm Au NPs to create Au$_5$-PEG$_{1000}$-AD$_x$ NPs ($\sim$10 nm). x indicates the relative level of hydrophobicity of the stain to bind to cyclodextrin-containing nanoparticles.

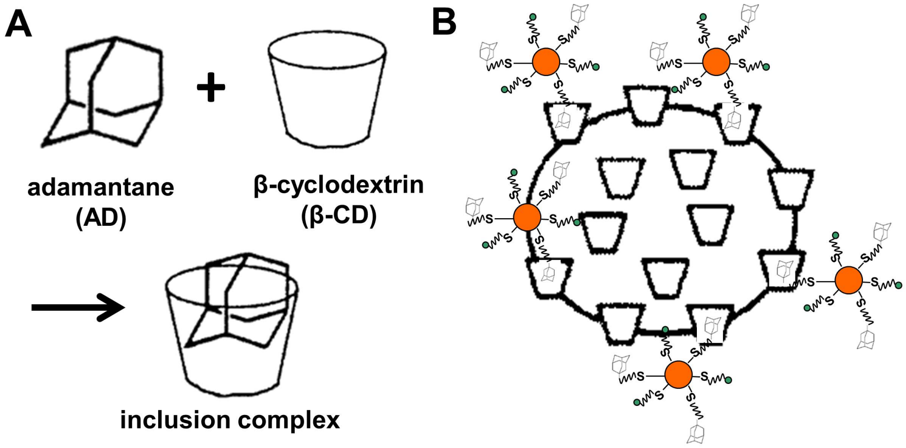

Figure 5.2: Principle of specific staining. (A) Adamantane (AD) residues are known to form inclusion complexes with beta-cyclodextrin (β-CD). (B) Multiple Au-PEG-AD particles will specifically bind to the surface of cyclodextrin-based nanoparticles due to AD-βCD interactions.

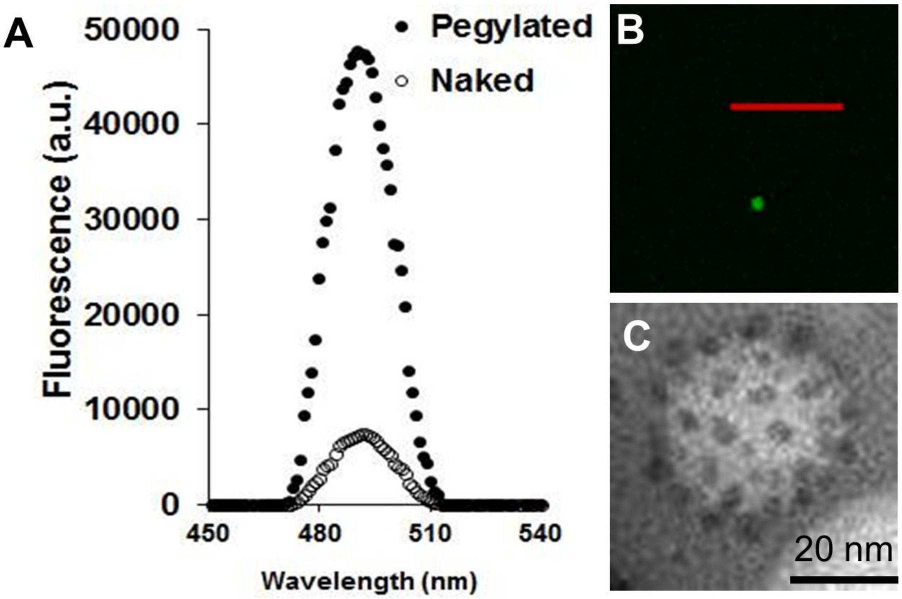

Figure 5.3: Fluorescence and binding of Au$_5$-PEG$_{1000}$-AD$_{50}$ NPs. (A) Emission spectra. 5 nm AuNPs are weakly fluorescent when excited by an argon laser at 488 nm. PEGylation using gold-sulfur linkage confers fluorescence signal to the gold particle. Emission: 500-550 nm bandpass (BP) filter. (B) The confocal micrograph shows fluorescence of a cluster of Au$_5$-PEG$_{1000}$-AD$_{50}$ NPs. Scale bar = 20 µm. (C) This TEM image shows direct binding of Au$_5$-PEG$_{1000}$-AD$_{50}$ NPs (individual dark spots) atop the surface of IT-101, a CDP-based nanoparticle (white). Scale bar = 20 nm.

metal to ligand charge transfer (MMLCT) interactions in their excited states. Compared to other capping ligands (e.g., triphenylphosphine), sulfur-containing ligands give more prominent MMLCT for AuNPs [189]. Thus, the application of this gold-sulfur based stain onto tissue sections permits visualization using confocal microscopy. In addition, TEM can reveal these AuNPs due to their inherently high electron density.

For signal specificity, the stain displays multiple copies of AD on the AuNP periphery to exploit the strong hydrophobic interaction between cyclodextrin cups of the nanoparticles and adamantane ($K_d = 10^{-4} - 10^{-5}$ M) [190]. Fig. 5.2 is a schematic illustration of the specific interaction between the proposed stain and a cyclodextrin-polymer (CDP) based nanoparticle.

The staining of tissue sections usually proceeds in buffered salt, which incidentally can lead to aggregation of AuNPs. Because the fluorescence of thiol-capped AuNPs are restricted to small sizes ($\leq$5 nm), PEGylation provides steric stability of the stain against salt. By UV-

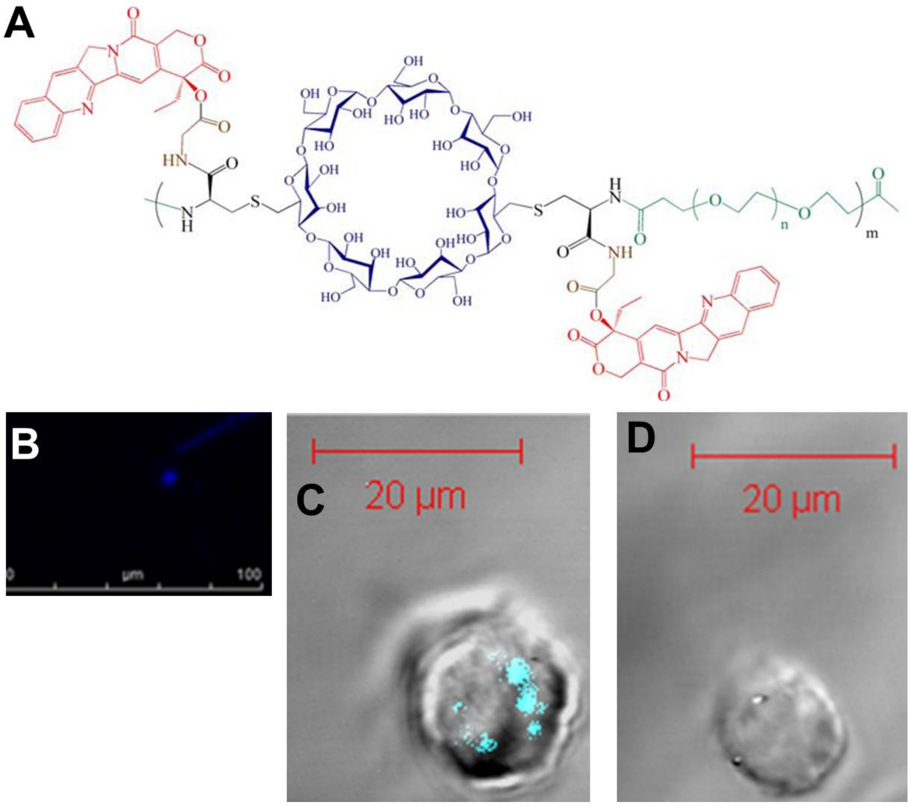

Figure 5.4: Fluorescence of IT-101. (A) Structure of IT-101. The components of the parent polymer are β-CD (blue), PEG (green), and L-cysteine (black). CPT (red) is attached to the polymer via a single glycine amino acid linker (brown). (B) The fluorescence of IT-101 (blue) originates from CPT. Excitation = 370 nm; emission = 440 nm. Neuro2A cells incubated with IT-101 showed uptake of IT-101 given the intense CPT fluorescence (C), while untreated cells did not (D).

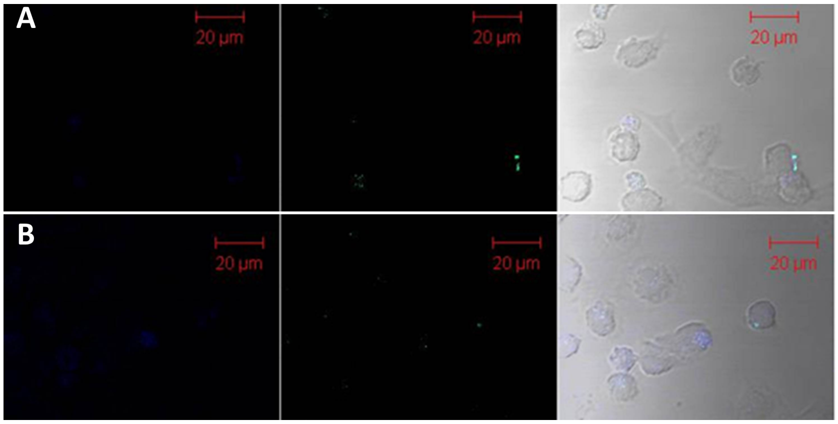

Figure 5.5: Nature of staining. (A) After incubation with β-CDP for 7 h, Neuro2A cells took up the polymer, and were stained by Au$_5$-PEG$_{1000}$-AD$_{50}$ NPs. There was no CPT fluorescence because the polymer solution did not contain any CPT. (B) After incubation with pure CPT (for only 90 min to avoid cytotoxicity), Neuro2A cells showed CPT fluorescence and limited gold fluorescence. There was no overlap between both types of signals. Left = CPT (ex: 370 nm; em: 440 nm). Middle = Au$_5$-PEG$_{1000}$-AD$_{50}$ (ex: 488 nm; em: 500-550 nm bandpass filter). Right = Merged image with bright field.

Vis spectrometery and confocal microscopy, capping AuNP with thiolated PEG gave rise to a pronounced elevation in fluorescence (Fig. 5.3A-B) when excited by an argon laser (488 nm). It is desirable to verify the binding of the stain on CDP-based nanoparticles. We employed IT-101 as the model nanoparticle (see Fig 5.4A for its chemical structure). Incubation of IT-101 with the chemical stain led to obvious binding on the surface of IT-101 (Fig. 5.3C).

Optimization of chemical stain

We then exploited the fluorescence of IT-101 to more accurately characterize the binding properties of Au_5-PEG_{1000}-AD NPs as a chemical stain. (CPT demonstrates fluorescence with peak excitation and emission wavelengths of 370 and 450 nm, respectively [191]. It is thus not surprising that IT-101 emits fluorescence at similar wavelengths as CPT (Fig. 5.4)).

Fig. 5.3C only revealed binding of the stain atop IT-101, but did not indicate whether the binding was toward CPT or β-CD as hypothesized. As a hydrophobic molecule, CPT may interact with the stain. To address this question, Neuro2A cells were incubated with either pure β-CDP or pure CPT, rinsed with PBS, and stained by Au_5-PEG_{1000}-AD NPs (dispersed in 1× PBS). Cells were mounted for viewing under a confocal microscope after PBS rinses to remove any non-specifically bound stain. Fig 5.5 demonstrated that binding was due to CDP, not CPT. While Neuro2A cells (mouse neuroblastoma) preincubated with blank β-CDP solution (without CPT) showed gold staining, the same cells preincubated with pure CPT (no β-CDP) did not.

The above experiments set the stage to optimize the hydrophobicity required for effective staining of IT-101 (or cyclodextrin-containing nanoparticles) in biological tissues or cells. While Au_5-PEG_{1000}-AD NPs must display sufficient AD residues to interact with CDP-based nanoparticles, they cannot be too hydrophobic to maintain solubility in the salt buffer for staining tissue sections. We prepared Au_5-PEG_{1000}-AD_x ($x = 0, 25, 50$) NPs by tuning the molar ratios of AD-$dPEG_{12}^{TM}$-SPDP and $mPEG_{1000}$-SH (Fig. 5.2) added to an aqueous suspension of 5 nm AuNPs.

For instance, the preparation of Au_5-PEG_{1000}-AD_{25} and Au_5-PEG_{1000}-AD_{50} NPs entails the addition of AD-$dPEG_{12}^{TM}$-SPDP and $mPEG_{1000}$-SH in a molar ratio of 1:3 and 1:1, respectively. Au_5-PEG_{1000}-AD_0 NPs served as negative control to verify the need of AD for effective staining. Fig. 5.6 presents staining data of Au_5-PEG_{1000}-AD_x NPs on Neuro2A cells pretreated with the same concentration of IT-101. Clearly, the colocalization of IT-101 and Au_5-PEG_{1000}-AD_x NPs fluorescence signals increased with AD content of the stain. This colocalization suggests that the chemical stain stains for IT-101 as a self-assembled particle, not merely CDP fragments without CPT. For future experiments covered in this thesis, we shall adopt **Au_5-PEG_{1000}-AD_{50}** NPs as the default chemical stain unless otherwise mentioned. (Results shown in Fig. 5.3 and Fig. 5.5 also entailed the use of Au_5-PEG_{1000}-AD_{50} NPs).

Generality of chemical stain

Results illustrated thus far anchor upon the use of Au_5-PEG_{1000}-AD_{50} NPs to stain only one type of cyclodextrin-polymer nanoparticle (IT-101) in biological specimens. Is is possible to apply this stain to other CDP-based nanoparticles, say CALAA-01 (Fig. 5.7)?

Unlike IT-101, CALAA-01 exhibits mulitple copies of the targeting ligands (human transferrin; Tf) on its periphery to target surface receptors of cancer cells, and may block effective binding between AD and CD cups. We developed an ELISA-like assay to show that binding of the chemical stain to CALAA-01 is specific and dose-dependent (Fig. 5.8A-C). In brief, CALAA-01 nanoparticles at a constant concentration were deposited into an ELISA plate pre-coated with antibodies against human Tf. After rinsing away excess CALAA-01, the application of different concentrations of Au_5-PEG_{1000}-AD_{50} NPs to the ELISA plate followed. Despite repeated rinsing to remove non-specifically bound Au_5-PEG_{1000}-AD_{50} NPs, the ELISA plate retained the stain in a dose-dependent fashion, as evidenced by the gradual increase in red color (by inspection) as well as absorbance reading at 520 nm (peak absorbance of Au_5-PEG_{1000}-AD_{50}). As negative

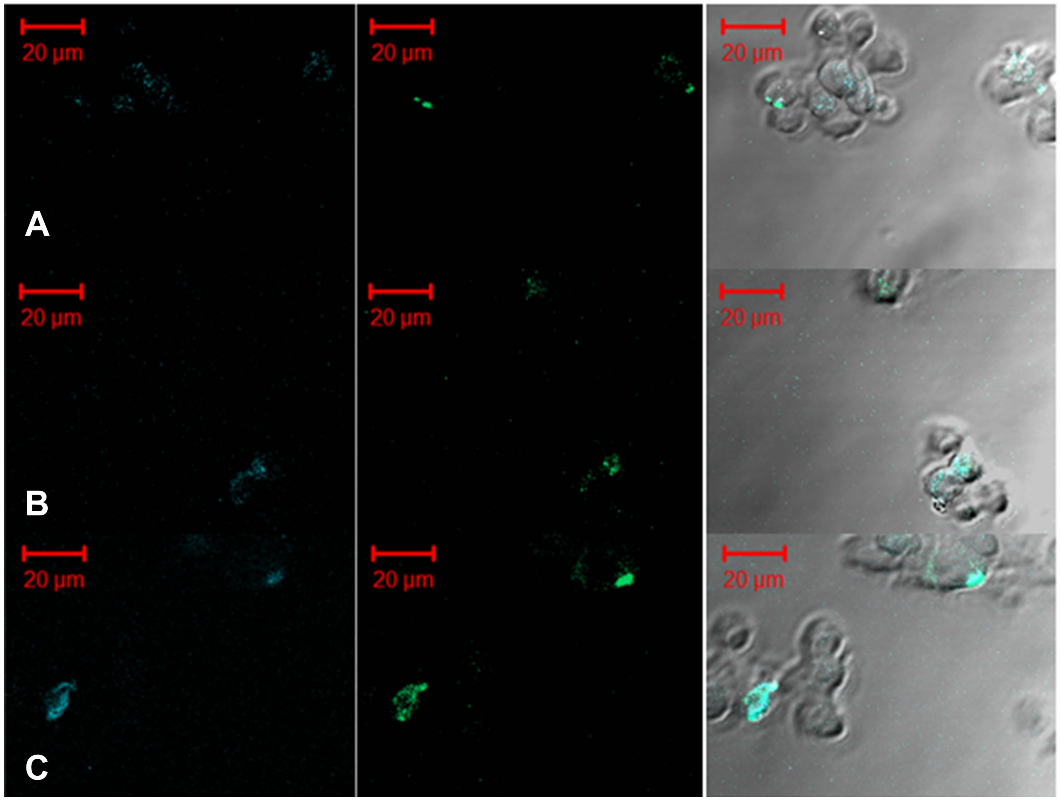

Figure 5.6: Optimization of staining. N2A cells were pretreated with IT-101 at 37 °C for 7 h, rinsed with 1× PBS, and stained for IT-101 using the same concentration of (A) Au$_5$-PEG$_{1000}$-AD$_0$, (B) Au$_5$-PEG$_{1000}$-AD$_{25}$, and (C) Au-PEG-AD$_{50}$ NPs. The colocalization of IT-101 and Au$_5$-PEG$_{1000}$-AD$_x$ NPs fluorescence signals increased with AD content. Staining due to Au$_5$-PEG$_{1000}$-AD$_{50}$ NPs showed overlapping with IT-101 fluorescence signals. Left = CPT (ex: 370 nm; em: 440 nm). Middle = Au$_5$-PEG$_{1000}$-AD$_x$ NPs (ex: 488 nm; em: 500-550 nm bandpass filter). Right = Merged image with bright field.

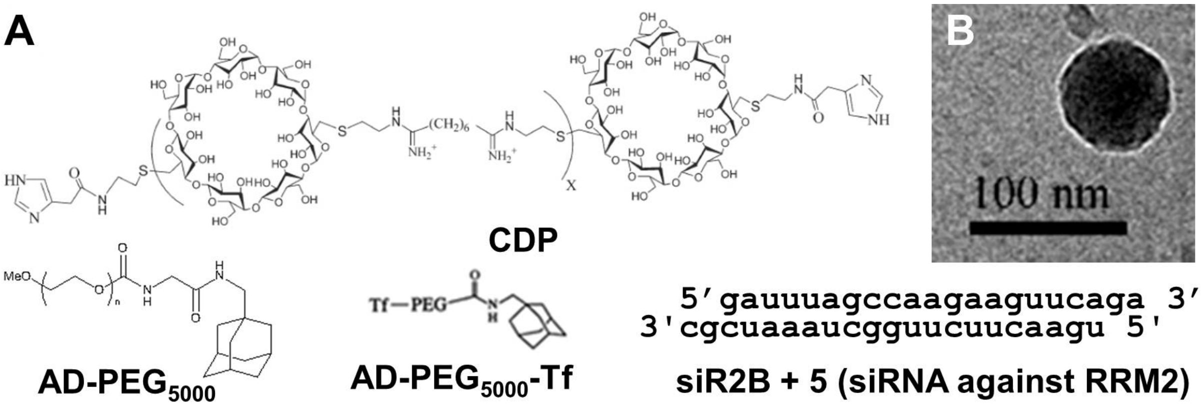

Figure 5.7: Composition of CALAA-01. (A) The delivery components are (i) a linear, catioinic cyclodextrin-containing polymer (CDP), (ii) an adamantane-PEG conjugate (AD-PEG$_{5000}$), and (iii) an AD-PEG conjugate with an human transferrin protein (Tf) connected to the other end of AD (AD-PEG$_{5000}$-Tf). These partsr will condense with siRNA (sequence shown) that specifically cleaves the mRNA encoding the M2 subunit of ribonucleotide reductase (RRM2). (B) The mixing of all components triggers the self-assembly of CALAA-01 nanoparticles of 70 nm in size. In this TEM image, the CALAA-01 nanoparticle appears dark due to staining of siRNA by uranyl acetate.

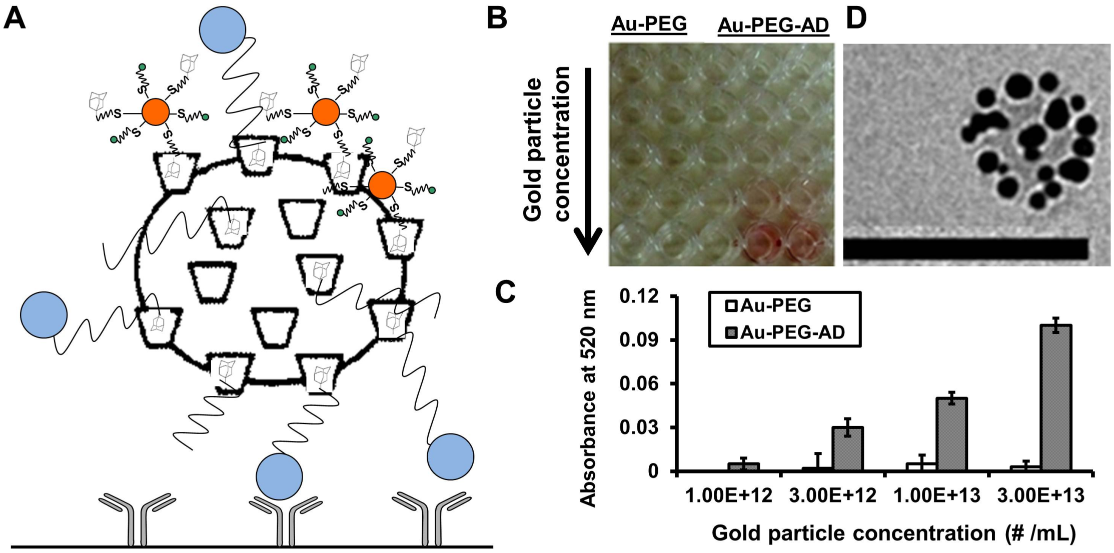

Figure 5.8: Binding of CALAA-01. (A) This schematic representation depicts the design of the ELISA-like binding assay. Blue circle = human transferrin (Tf); wavy line = PEG_{5000}; Y-shape = antibody against Tf pre-coated on the ELISA plate (black horizontal line). (B) After depositing CALAA-01 nanoparticles onto the ELISA plate (precoated with anti-Tf), Au_5-PEG_{1000}-AD_{50} NPs showed dose-dependent binding (red color originates from the applied gold stain). Control Au_5-PEG_{1000}-AD_0 NPs led to no binding independent of concentration. (C) Direct absorbance readout at 520 nm from the ELISA plate indicates dose-dependent staining by Au_5-PEG_{1000}-AD_{50} NPs. (D) This cryo-TEM image shows binding of isolated Au_5-PEG_{1000}-AD_{50} NPs atop a CALAA-01 NP. Scale bar = 100 nm.

control, no Au_5-PEG_{1000}-AD_{50} NPs were retained when no CALAA-01 was deposited in the ELISA plate beforehand, indicating the hydrophobic interaction between CD cups and AD as the nature of binding (data not shown). Furthermore, cryo-TEM delineates binding of isolated Au_5-PEG_{1000}-AD_{50} NPs atop a CALAA-01 nanoparticle (Fig. 5.8D).

Upon confirmation using the ELISA-like assay, an additional validation study to show the binding of Au_5-PEG_{1000}-AD_{50} NPs followed. Mice bearing subcutaneous Neuro2A tumors received i.v. injections of Tf-targeted, (Cy3)siRNA-containing, CDP-based nanoparticles. These nanoparticles are virtually the same as CALAA-01, except they contain a control siRNA sequence that targets the firefly luciferase gene (siGL3). Some of these siRNA strands contain a Cy3 moiety at the 5' end of the sense strand. Subsequent animal sacrifice allowed for the extraction of tumor. TEM confirmed the presence of such nanoparticles in Neuro2A cells within the tumor, confirming the successful intracellular delivery by targeted nanoparticles (Fig. 5.9).

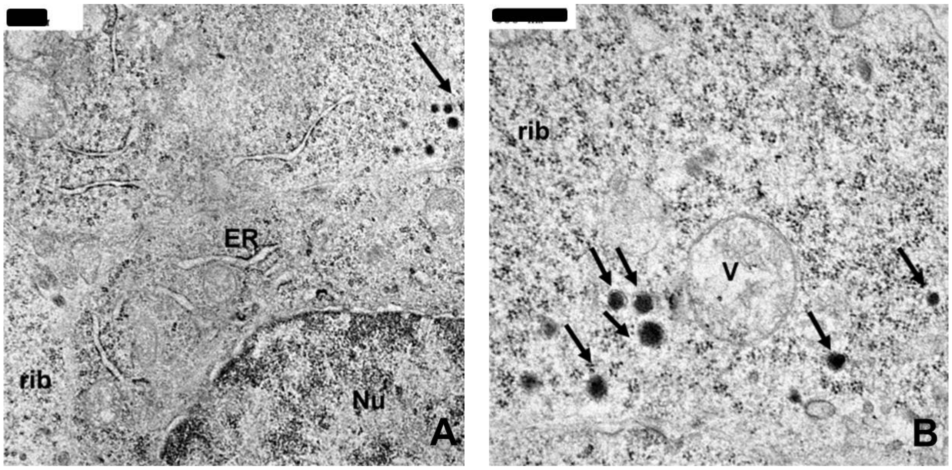

Figure 5.9: TEM revealed localization of targeted CDP nanoparticles (containing Cy3-siGL3) inside Neuro2A cells of the mouse subcutaneous tumor. (A) The proximity of targeted nanoparticles to the nucleus shows their intracellular localization. (B) Expanded view. Nu = nucleus, rib = ribosome, ER = endoplasmic reticulum, V = vesicle, black arrow = nanoparticles. Scale bar = 500 nm.

Confocal microscopy of the same tumor tisuses followed, used in conjunction with Au_5-PEG_{1000}-AD_{50} NPs. Like the staining of tumor tissues from previous IT-101 experiments, there was significant overlap of fluorescent signals due to Au_5-PEG_{1000}-AD_{50} NPs and Cy3-siRNA. The presence of gold fluorescence signals must accompany those of Cy3-siRNA, not vice versa (Fig. 5.10). This suggests that intracellular accumulation of targeted nanoparticles in Neuro2A cells within the tumor, and that Cy3-siRNA might have been released due to nanoparticle disassembly within Neuro2A cells. As negative control, Neuro2A tumors from mice injected with D5W failed to show any fluorescence of either Au_5-PEG_{1000}-AD_{50} NPs or Cy3-siRNA (data not shown).

Application of chemical stain

In summary, Au_5-PEG_{1000}-AD_{50} NPs can detect CDP-based NPs. Below are some applications of the stain to reveal pharmacological insights of nanoparticle-based therapeutics.

Intratumoral transport of IT-101

Schluep et al. [182] employed positron emission tomography (PET) to track the in vivo distribution pattern of radioactively labeled IT-101 in tumor-bearing mice as a function of time,

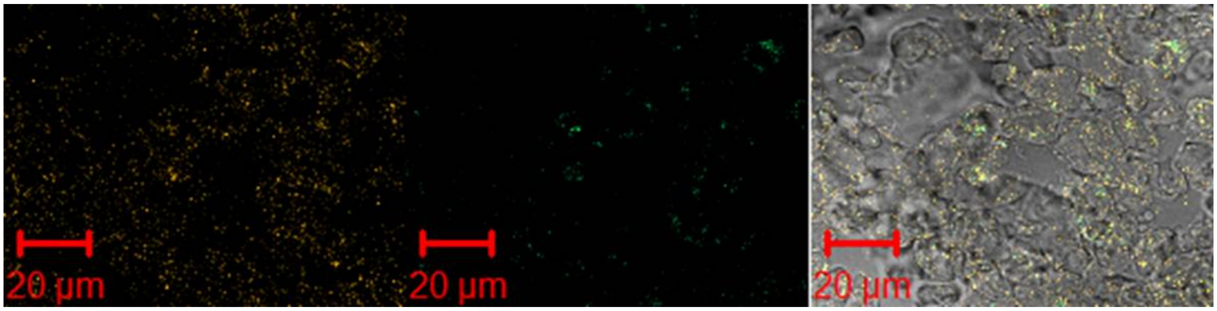

Figure 5.10: Confocal microscopy of the same Neuro2A tumor tissue as shown in Fig. 5.9. Au_5-PEG_{1000}-AD_{50} NPs bound to Cy3-siRNA containing, CDP-based targeted nanoparticles, whose localization was strictly intracellular. Left = Cy3-siGL3 (ex: 540 nm; em: 560-610 nm bandpass filter). Middle = Au_5-PEG_{1000}-AD_{50} (ex: 488 nm; em: 500-550 nm bandpass filter). Right = Merged image with bright field.

and discovered a more elevated label concentration in the tumor interstitium than that in blood plasma after 24 h. Moreover, they noted a gradual increase in label concentration in the tumor up to the 24th hour. Such dynamics of IT-101 tumor retention underscore the EPR effect and indicate that the majority of the nanoparticles stay intact in circulation and do not considerably disassemble into individual CDP strands. The same authors also utilized compartmental modeling to support the validity of the PET data, indicating that the apparent permeability of IT-101 out of blood vessels correspond to that of a nanoparticle of 37 nm in size, in close agreement to the hydrodynamic diameter of IT-101 (∼30 nm). Taken this together, the authors proposed a "sink" in which IT-101 nanoparticles could accumulate within the tumor.

However, PET and mathematical modelling data cannot provide any morphological information of the precise location of this "sink" within the tumor. For general tumor-bearing animal models, prior studies attributed the nature of this "sink" for untargeted nanoparticles (e.g., dextran-coated iron oxide nanoparticles [192], long-circulating liposomes [145], and PEGylated gold nanoparticles [193]) to tumor vascular endothelial cells, tumor-associated macrophages, tumor stroma in the extracellular space. CDP nanoparticles are different from the above three particle types, because they contain hydrophobic pockets within the CD molecules for interaction with lipid rafts of cell membranes [175]. Will they reflect a different intratumoral fate?

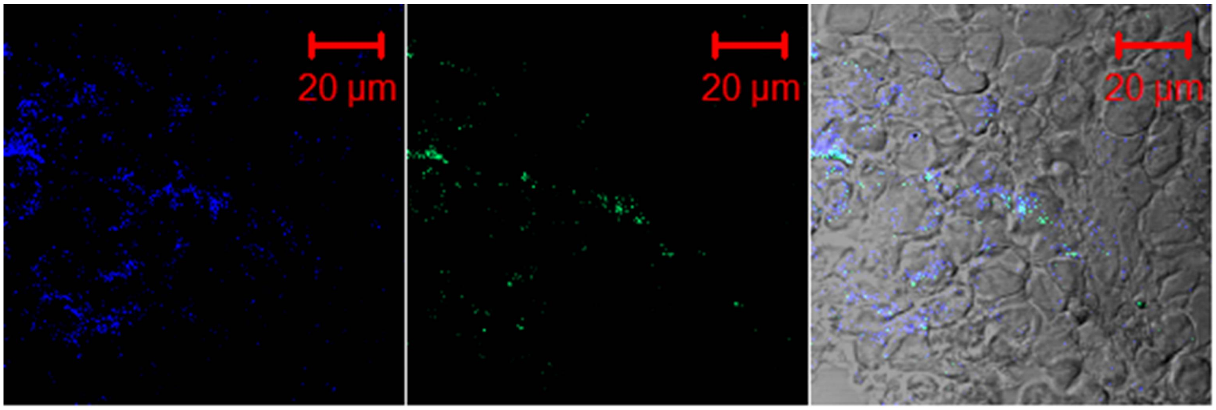

Figure 5.11: Intracellular sink of IT-101. Mice bearing Neuro2A tumors received injections of IT-101. Animal sacrifice 24 h later permits the extraction of tumors, whose cryosections were stained for the presence of IT-101 using Au_5-PEG_{1000}-AD_{50} NPs. From this representative confocal micrograph, IT-101 accumulated in Neuro2A cells within the tumor, indicating Neuro2A cells as the biological "sinks" for IT-101. Left = CPT (ex: 370 nm; em: 440 nm). Middle = Au_5-PEG_{1000}-AD_{50} NPs (ex: 488 nm; em: 500-550 nm bandpass filter). Right = Merged image with bright field.

Our chemical stain could clarify the nature of this biological "sink" for CDP-based nanoparticles. Mice bearing subcutaneous Neuro2A tumors received i.v. injections of IT-101. 24 h later, animal sacrifice took place to permit tumor extraction. Staining tumor cryosections with Au_5-PEG_{1000}-AD_{50} NPs revealed prominent colocalization of fluorescence signals due to CPT and Au_5-PEG_{1000}-AD_{50} NPs that bind to CDs (Fig. 5.11). IT-101, not just released CPT, was inside tumor Neuro2A cells. Thus, the "sink" for IT-101 within the tumor arose from the internalization by cancerous cells, in stark contrast to intratumoral fate of other untargeted nanoparticles listed above. Perhaps tumor cell internalization is a unique "sink" to CDP-based nanoparticles due to their surface properties. This "sink" may explain why the amounts of IT-101 and CPT in the tumor remained relatively constant for several days after an i.v. injection [194].

Dose-dependent accumulation of CALAA-01 in patients

Therapeutics that are designed to engage RNA interference (RNAi) pathways have the potential to provide new, major ways of imparting therapy to patients [195] [196].

A key obstacle with applying siRNAs in mammals is their intracellular delivery to specific tissues and organs that express the target gene, via the use of clinically compatible methods of administration. Several delivery vehicles have been combined with siRNAs to improve their delivery in animals, and early clinical data are beginning to emerge.

Davis et al. is now conducting the first, to their knowledge, in-human siRNA phase I clinical trial involving the systemic administration of siRNA to patients with solid cancers using a targeted, nanoparticle delivery system (clinical trial registration number: NCT00689065) [160][187]. Patients with solid cancers refractory to standard-of-care therapies are administered doses of CALAA-01 nanoparticles on days 1, 3, 8, and 10 of a 21-day cycle by a 30-min i.v. infusion.

We investigated biopsies from three metastatic melanoma patients (A, B, and C), who received CALAA-01 doses of 18, 24, and 30 mg/m^2 siRNA, respectively. Given the highly experimental nature of this protocol, the regulatory process at both the local and federal levels explicitly precluded a provision for mandatory biopsies in all patients. Therefore, biopsies were obtained on a voluntary basis. Biopsies in these three patients were collected after the final dose of cycle 1 (denoted A_{post}, B_{post} and $C1_{post}$) and compared to archived tissue (denoted A_{pre}, B_{pre} and $C1_{pre}$). Patient C continued therapy beyond one cycle and provided another set of biopsy material ($C2_{pre}$ that was obtained approximately 1 month after the final dose of cycle 1, and $C2_{post}$ that was collected on the day of the final dose of cycle 2).

Sections of the tumor tissue were stained for the presence of CALAA-01 nanoparticles using Au_5-PEG_{1000}-AD_{50} NPs. Samples A, B and C1, analyzed in a blinded fashion, demonstrated a heterogeneous distribution of nanoparticles only in post-dosing tumor tissue (Fig. 5.12). The nanoparticles could localize intracellularly in tumor tissue and were not found in the adjacent epidermis. In these biopsies, TEM images were dominated by melanosomes [197], inhibiting the identification of the nanoparticles (data not shown). Samples $C1_{post}$ and $C2_{post}$ reveal the highest number and intensity of stained regions. B_{post} exhibits a decreased amount of staining relative

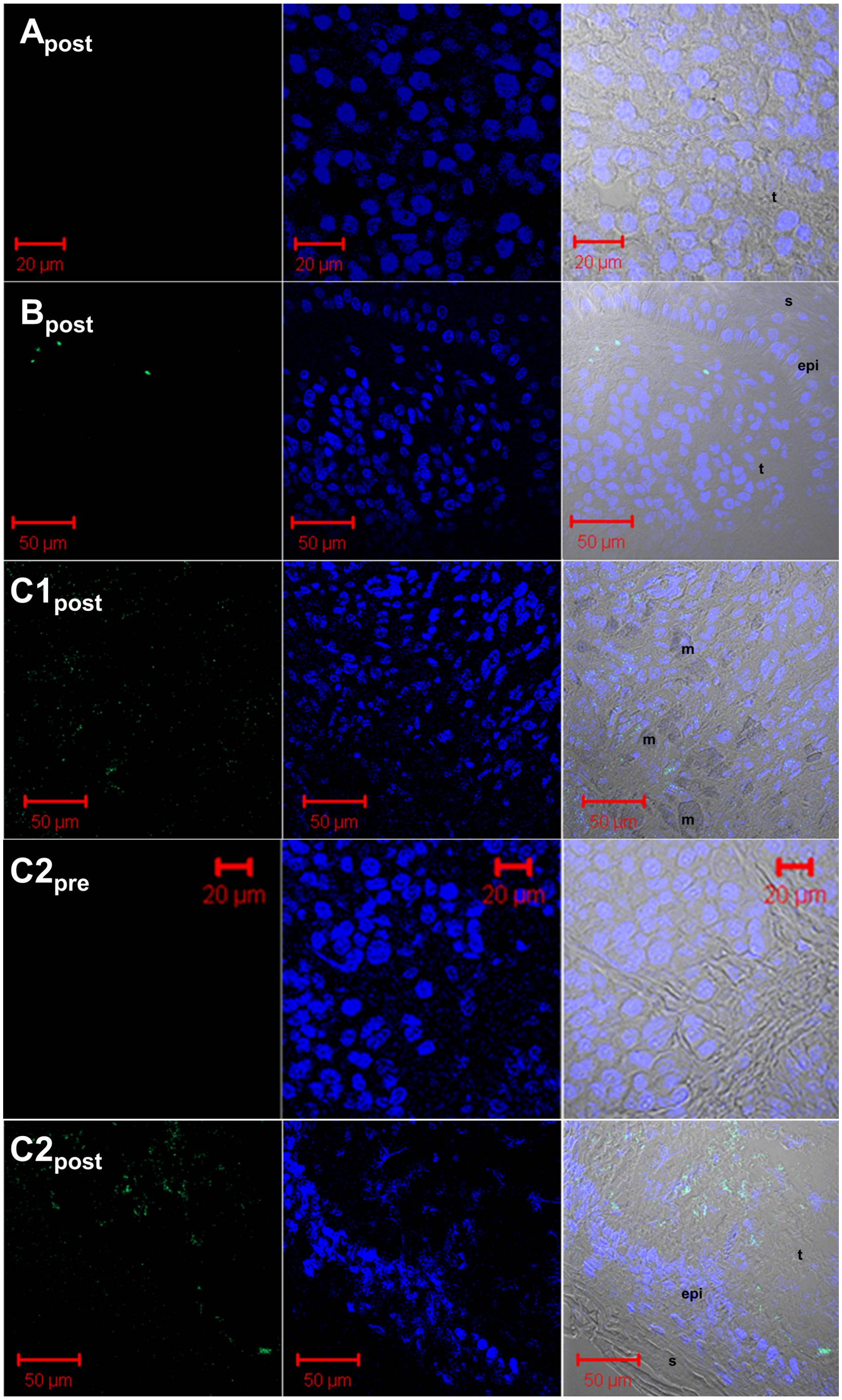

Figure 5.12: Detection of CALAA-01 nanoparticles in human tumors. Confocal micrographs of post-treatment biopsy sections from patients A, B, and C demonstrate the dose-dependent accumulation of CALAA-01 nanoparticles. epi, epidermis, m, melanophage; s, skin side; t, tumor side. Left = Au_5-PEG_{1000}-AD_{50} (ex: 488 nm; em: 500-550 nm bandpass filter), green. Middle = DAPI counter stain, blue. Right = Merged image with bright field.

to samples C1$_{post}$ and C2$_{post}$. A$_{post}$ does not reveal the presence of the stain. All pre-dosing samples are completely negative for the stain (data not shown). We do not know how long the nanoparticles reside within the cells and release siRNA. Because the nanoparticles are observed in the sample C1$_{post}$ and not the sample C2$_{pre}$, they must disassemble within 1 month.

From the same tumor tissues used for staining with Au_5-PEG_{1000}-AD_{50} NPs, downstream molecular biological and immunohistochemical analyses reflected notable decrease in RRM2 expression at both mRNA and protein levels due to the RRM2-specific siRNA. Moreover, results from a modified 5'-RNA-ligand-mediated RACE (5'-RLM-RACE) PCR technique showed that the delivered siRNA induces the desired mRNA cleavage in both C2$_{pre}$ and C2$_{post}$ tumor biopsies (data not shown). Taken these results together, this is the first direct evidence of an RNAi mechanism of action in a human (patient C) from systematically administered siRNA.

In summary, systemically administered siRNA, when encapsulated in targeted nanoparticles, can accumulate in melanoma cells within patient tumors. This is the first example of a dose-dependent accumulation of targeted nanoparticles in tumors of humans from systemic injections for nanoparticles of any type. siRNA delivered by the CALAA-01 platform can engage the RNAi machinery in a solid human tumor. Thus, siRNA can be a gene-specific therapeutic for humans.

5.4 Conclusion

Cyclodextrins have a long history of usage in drug delivery formulations, with the first patient treated with CD-containing pharamaceutics back in 1953 [198]. CDs can enhance water solubility of hydrophobic drugs by forming non-covalent, water-soluble inclusion complexes. They can also improve safety and bioavailability. Due to these attractive properties, multiple pharmaceutics based on CD-polymer (CDP) conjugates have emerged into the market since the 1980s.

As a cancer treatment modality, nanocarriers like CDP-based nanoparticles can protect the drug payload from premature degradation as well as enhance their retention into solid tumors and intracellular localization. To ascertain their therapeutic efficacy, it is essential to track their in vivo pharmacological behavior of nanoparticles besides downstream biological effects (e.g., toxicity, immune response, tumor regression, gene inhibition at mRNA and protein levels). For pharmacological effects, pertinent parameters include blood pharmacokinetics and organ-level distribution, as well as retention kinetics and transport within the target tumor tissue.

The precise tracking of pharmacological behavior in animal models via live imaging generally necessitates the chemical attachment of fluorophores, quantum dots, or radioactive labels on the carrier polymer and/or drug payload, with the assumption that such addition of labels would not drastically affect the self-assembly of nanoparticles as well as their resultant physicochemical properties. For patient use, moreover, regulatory authorities do not permit the inclusion of labels owing to their potential toxicity arisen from indefinite accumulation in the body. Thus, the only viable option to acquire pharmacological data in a clinical setting is through ex vivo analysis by microscopy of tumor biopsies collected from patients.

Here, we report the design and optimization of a chemical stain that specifically recognizes CDP nanoparticles ex vivo. The stain comprises a 5 nm gold nanoparticle core, with its surfce decorated with multiple copies of adamantane and PEG chains via gold-sulfur linkages on the periphery. Such design confers the chemical stain three properties: (1) pronounced fluorescence for detection by confocal microscopy, (2) strong binding to hydrophobic cyclodextrin cups of CDP nanoparticles, and (3) steric stability against salt-induced aggregation. The application of this chemical stain (Au_5-PEG_{1000}-AD_{50} NPs) ex vivo to treated cells or tumor cryosections that contain administered CDP nanoparticles allows for their detection. This stain reveals intracellular accumulation of CDP nanoparticles (IT-101 and CALAA-01) in cells, animal tumor tissues, and patient tumor biopsies, and thus warrants the extraction of key in vivo pharmacological information (such as intratumoral transport and dose response) in an ex vivo setting.

Acknowledgment

We thank Christopher A. Alabi for making Au-PEG-AD, and Han Han for the cryo-TEM analysis. We thank H. Sazegar, E. Seja, A. Villanueva, and the G-CRC nursing staff (UCLA), L. Kalinoski, J. Peterkin, S. Rele, Y. Liang and J. Y. C. Liu (Calando Pharmaceuticals) for their assistance in conducting the clinical trial. We thank Dr. J. S. Economou for performing the tumor biopsies, and Drs. B. Chmielowski and Z. Wainberg for patient referrals (UCLA). This work was supported in part by the Daljit S. & Elaine Sarkaria Biomarker Laboratory Fund.

5.5 Materials and Methods

Synthesis of SPDP-dPEG$_{12}^{TM}$-AD

To a solution of SPDP-dPEG$_{12}^{TM}$-NHS (100 mg, 0.11 mmol; Quanta Biodesign) in 3 mL of anhydrous dichloromethane was added adamantanemethylamine (0.11 mmol, 21 µL). The solution was stirred for 16 h at RT, after which the solvent was removed and the product dried under vacuuo. (MALDI-TOF) $[M+Na]^+$ 984.08, $[M+K]^+$ 1000.16.

Assembly of Au$_5$-PEG$_{1000}$-AD$_x$ NPs

To identify the optimal amount of adamantane (AD) required for staining, different molar ratios of SPDP-dPEG$_{12}^{TM}$-AD and methoxy-PEG$_{1000}$-SH (Laysan Bio) was added to aqueous suspensions of 5 nm gold nanoparticles (Nanopartz). To make Au$_5$-PEG$_{1000}$-AD$_{25}$ NPs, mPEG$_{1000}$-thiol (21 µg, 21 nmol) and SPDP-dPEG$_{12}^{TM}$-AD (8 µg, 7 nmol) were added to 1 mL of pre-sonicated gold suspension (10^{13} particles per mL). For Au$_5$-PEG$_{1000}$-AD$_{50}$ NPs, mPEG$_{1000}$-thiol (14 µg, 14 nmol) and SPDP-dPEG$_{12}^{TM}$-AD (16 µg, 14 nmol) were added instead. As negative control, Au$_5$-PEG$_{1000}$-AD$_0$ (no AD) NPs were also prepared by adding only mPEG$_{1000}$-thiol (28 µg, 28 nmol).

Independent of AD content, the reaction mixture was vortexed at RT for 30 min and diluted to 4 mL with deionized water. The resulting 4 mL solution was diafiltered twice with a 10 kDa membrane (Millipore), resuspended to 1 mL of 1× PBS, and stored at 4 °C for future use.

In vitro transfection of IT-101

5×10^4 Neuro2A cells were cultured on 625 mm^2 cover-slips pre-deposited in a 6-well plate for 2 d at 37 °C and 5% CO_2 in complete growth medium (DMEM medium supplemented with 10% FBS, 100 units/mL penicillin, and 100 units/mL streptomycin).

On the day of transfection, the cells received transfection of 30 µg polymer/mL of IT-101 in complete growth medium for 7 h at 37 °C and 5% CO_2.

Nature of IT-101 staining by Au_5-PEG_{1000}-AD_{50} NPs

Neuro2A cells on cover-slips were incubated with pure cyclodextrin polymer (CDP) for 7 h. As another control, the same experiment was repeated with pure camptothecin (CPT). To prevent cytotoxic effects, the transfection with CPT lasted for 90 min. Cells transfected with CDP and CPT were stained by Au_5-PEG_{1000}-AD_{50} NPs and mounted for confocal microscopy.

Tumor formation and systemic IT-101 delivery

Neuro2A-Luc cells were cultured in complete growth medium (DMEM supplemented with 10% FBS, 100 units/mL penicillin, and 100 units/mL streptomycin). In the right hind flank, immunodeficient (NOD.CB17-Prkdcscid/J) mice (Jackson Laboratory) received subcutaneous implantation of N2A cells (at 10^6 cells per mouse per 0.1 mL of DMEM). Before injection, tumors reached 100-200 mm^3 in size, as determined by caliper measurements ($0.5 \times l \times w^2$). Two mice received i.v. administration of IT-101 (10 mg polymer/kg animal; formulated in 0.1 mL of D5W) via the tail-vein. As controls, two other mice received i.v. injections of 0.1 mL of D5W. Animal sacrifice by CO_2 overdose took place 24 h after injection to collect tumors for confocal microscopy.

ELISA-like binding of CALAA-01 by Au_5-PEG_{1000}-AD_{50} NPs

The entire procedure was conducted at RT with mild shaking on a plate shaker. Into each well of a 96-well ELISA plate was coated with 0.1 mL of coating buffer (10 µg/mL mouse IgG against human transferrin (Bethyl Laboratories) in 50 mM carbonate-bicarbonate buffer, pH = 9.6) for 1 h. Three rinses with 0.1 mL of wash buffer (50 mM Tris, 140 mM NaCl, 0.05% Tween 20, pH = 8) followed to remove unbound antibodies. Next, blocking by adding 0.2 mL of blocking buffer (50 mM Tris, 140 mM NaCl, 1% bovine serum albumin, pH = 8) took place for 1 h, followed by three brief rinses. After that, each well was loaded with 0.1 mL of either targeted CDP particle solution (0.5 mol% AD-PEG$_{5000}$-Tf in 1× PBS) or 1× PBS (negative control) and incubated for 2 h. After five rinses to remove unbound targeted particles, each well was loaded with 0.1 mL of staining solution (Au$_5$-PEG$_{1000}$-AD$_{50}$ or Au$_5$-PEG$_{1000}$ NPs) and incubated for 2 h. Upon five rinses to remove unbound stain, each well was loaded with 0.1 mL of 1× PBS for absorbance measurement at 520 nm (surface plasmonic peak for Au$_5$-PEG$_{1000}$-AD$_{50}$ NPs) using a Safire^2 Microplate Reader (Tecan). Reported values are mean absorbance from duplicate experiments.

Cryo-TEM of complex of CALAA-01 and Au$_5$-PEG$_{1000}$-AD$_{50}$ NPs

Au$_5$-PEG$_{1000}$-AD$_{50}$ NPs were added to CALAA-01 nanoparticles and allowed to incubate for 1 h prior to cryo-TEM analysis. An automated climate-controlled plunge-freezer (Vitrobot, FEI) was used for sample vitrification. In here, humidity was set at 100% to minimize evaporation and temperature was set at 21 °C. A glow discharged Quantifoil holey carbon grid (EMS) was loaded into this chamber and 5 µL of sample was applied onto the grid. Blotting time was set at 1 s and drain time at 1 s before the sample was plunged into the center of a Vitrobot cup filled with liquid ethane. The grid was then quickly transferred into the outer ring containing liquid nitrogen and stored in a grid box under liquid nitrogen for later analysis. Vitrified sample was loaded onto a pre-vacuumed and pre-cooled (with liquid nitrogen) Cryo sample holder. The holder was then inserted into Techni FEI T12 TEM for imaging.

Systemic delivery of siRNA-containing CDP nanoparticles

Two NOD.CB17-Prkdcscid/J mice bearing subcutaneous Neuro2A tumors (prepared identically as for IT-101 delivery) received i.v. administration of siRNA-containing CDP nanoparticles (5 mg siRNA/kg animal; formulated in 0.1 mL of D5W) via the tail-vein. The model siRNA sequence, siGL3 (sense: 5'-CUUACGCUGAGUACUUCGAdTdT-3'; anti-sense: 5'-UCGAAGUACUCAGCGUAAGdTdT-3'), used here targets the mRNA encoding the firefly luciferase gene (Integrated DNA Technologies). 20% of the siGL3 molecules in the formulation contain a Cy3 residue at the 5' end of the sense strand. Two other control mice received i.v. injections of 0.1 mL of D5W. Animal sacrifice by CO$_2$ overdose took place 24 h after injection to collect tumors for confocal microscopy (for Au-PEG-AD$_{50}$ staining) and TEM.

Chapter 6

Conclusion

Falling between individual molecules and the corresponding bulk materials, the unique size of nanomaterials opens the possibility of interaction with biological tissues, spurring the emergence of the field of bionanotechnology and the creation of nanoparticle-based therapeutics, in vitro diagnostics, and in vivo contrast agents.

The application of nanotechnology to drug delivery has exerted considerable impact on medicine in the past few decades. Using nanotechnology, one can prolong the circulation of hydrophobic small molecules or macromolecules in blood plasma, tailor their delivery to specific tissues or intracellular locations, and even visualize sites of drug delivery by combining therapeutic agents with imaging modalities [199]. Over 20 nanoparticle-based therapeutics are in clinical use, and numerous others are at various stages of preclinical and clinical development. With the gradual shrinkage of pipelines from pharmaceutical companies as well as the imminent release of several blockbuster drugs from patent [200], nanoparticle-based therapeutics are expected to play an ever increasingly important role in the modern medicine landscape.

Despite advances in using different drug payload and delivery vehicles to target different diseases, the nanomedicine field still lacks consensual and mechanistic understanding in how therapeutic nanoparticles can reach targeted biological sites in vivo. This thesis establishes design criteria of nanoparticle properties (e.g., hydrodynamic size, surface charge, targeting ligand density, hydrophobicity, electrophoretic mobility, porosity) to achieve effective delivery of therapeutics. To examine the in vivo “structure-function” relationships of nanoparticles in a mechanistic fashion, all studies involve the adjustment of one nanoparticle physicochemical parameter, while keeping all other parameters constant.

The thesis concerns the pharmacological fate of nanoparticles following their systemic administrations into living systems. While such “fate” largely depends on nanoparticle physicochemical parameters, the route of administration is also a crucial factor. Clinical drug delivery applications mainly employ the systemic route, for its significant advantages over other options. Local injections (i.e., subcutaneous or intratumoral) are not useful for targeting metastatic tumors, and cannot overcome the intratumoral pressure gradient due to fast tumor proliferation. Oral delivery of protein-based nanoparticles suffers from degradation in gastrointestinal acid, low absorption, hepatic first-pass metabolism, and a significant initial increase in drug concentration.

Normal mice received systemic administrations of PEGylated gold nanoparticles (Au_x-PEG_y NPs) in the submicron size range ($10^0 \sim 10^2$ nm) as model probes. Metallic nanoparticles generally exhibit strong Mie scattering, and permits for detection by dynamic light scattering (DLS) for the determination of hydrodynamic diameter and zeta potential, two key colloidal physicochemical properties open to manipulation in all mechanistic studies.

One fundamental advantage of gold is its versatility: it is compatibile with the application of multiple imaging modalities. The collective use of inductively coupled plasma mass spectrometery (ICP-MS), histology with silver enhancement, and transmission electron microscopy (TEM) permits the ex vivo tracking of blood pharmacokinetics as well as distribution of Au_x-PEG_y NPs at the organ, tissue, and cellular levels, respectively, all resulting from the injection into the same animal (Fig. 1.2). The covalent attachment of PEG chains onto the particle surface (PEGylation) confers aqueous solubility, steric stability against physiological amounts of salt and serum, and enhanced plasma circulation to the nanoparticles.

Here, most distribution studies utilize organs extracted mice sacrificed 24 h after injection of

Au_x-PEG_y NPs. For the onset of the enhanced permeation and retention (EPR) effect to target tumors passively (Chapter 2), 24 h represents a typical duration for the plasma concentration gradient to pump injected nanoparticles into the tumor through the blood endothelial pores. Thus, results from these distribution studies indicate an "eqilibrium" pattern of nanoparticles. Future work may include studies conducted at earlier or later time points (e.g., 30 min, 4 h, or 2 d after injection) to characterize the dynamics of particle accumulation.

The avoidance of reticuloendothelial system (RES) uptake has long been a key consideration in designing nanoparticles to achieve prolonged circulation. PEGylation is a viable strategy to sterically protect nanoparticles from aggregation due to the non-specific binding of serum complement proteins (e.g., opsonins) that can trigger RES clearance. Yet, the engraftment of PEG chains onto larger particles is not sufficient to curb RES uptake. RES uptake seems to largely depend on particle size, not PEG chain length. At the organ level, particle accumulation in the liver and spleen correlates positively with particle size (Fig. 4.4). At both tissue and cellular levels, hepatic macrophages (Kupffer cells) and the spleen (both members of the RES) are responsible for clearing larger nanoparticles by phagocytic uptake (Fig. 2.5), leading to the premature clearance of nanoparticles from blood circulation (Fig. 4.3).

In this thesis, model probes are nearly spherical. Material anisotropy may provide another solution to attenuate RES uptake besides PEGylation. Particle geometry, not size, can dictate to the uptake of micro- and nanosized objects by macrophages in vitro [201] [202] [203]. Within animal models, PEGylated gold nanorods demonstrate more effective evasion of uptake by the liver and spleen than PEGylated gold nanoparticles [204]. Improvements in fabrication techniques to control particle geometry and anisotropic material assembly at the nanoscale [205] lead to the creation of more interesting shapes (e.g., nanodiamond [206], nanofullerene [207], nanocube [208]), and may encourage careful elucidation of the effect of particle geometry on RES clearance.

As a point of digression, nanosized objects with different physicochemical and structural properties can possess different blood contact properties, compatibility issues, stimulatory and supressive responses of the immune system when delivered systemically to animal models [209]. The exposure of nanoparticles to cultured cells and tissues can also induce oxidative stress, triggering the production of inflammatory cytokines and reactive oxygen species (ROS) [210]. As particles decrease in size, the fraction of atoms exposed to the particle surface increases, causing discontinuous crystal planes and structural defects. Defects can serve as reactive sites for the production of ROS, and can cause downstream toxicity as these particles interact with biological tissues. Toxic effects may include mitochondrial perturbation, inflammation, protein denaturation, and DNA damage [211]. At present, there exist no universal standards for assessing the immune toxicity of nanoparticles. Whereas European authorities mandate the application of immune function tests as an initial screen for immunotoxicity, the US and Japanese guidelines adopt the "as-needed approach", recommending such tests only when prior evidence indicates a need [212] [213]. Global representatives from industry, academia, and government agencies must jointly establish acceptable standards to determine in vivo toxicity. Possible assay criteria may include blood chemistry, hematology, histopathology, and immunogenicity.

Back to the in vivo distribution problem, kidneys of normal mice demonstrate unexpected retention patterns of Au_x-PEG_y NPs. While particle accumulation nearby the renal peritubular capillaries show no clear dependence on size (Figs. 4.5 and 4.8), there exists a unique hydrodynamic size (ca. 75 ± 25 nm) that can maximize nanoparticle accumulation in the kidney mesangium, at the organ (Fig. 4.4), tissue (Fig. 4.6), and cellular levels (Fig. 4.9). This maxima (up to 5% of injected dose) originates from a delicate balance between two physiological processes at work: uptake of mesangial cells and filtration by the perforated endothelium of the glomerular capillaries. This is the first example of passively targeting the kidney mesangium (and its associated mesangial cells) using nanoparticles of controlled size, and opens the possibility of designing nanoparticle-based therapeutics for treatment of diseases specifically at the kidney mesangium (e.g., diabetic nephropathy [214], IgA glomerulonephritis [215], mesangial sclerosis [216]). Moreover, to enhance delivery into mesangial cells, therapeutic nanoparticles of 75 ± 25 nm in diameter can even contain ligands that target surface receptors (e.g., mannose [217], pro(renin) [218]). Furthermore, nanoparticle of different sizes for kidney passive targeting all possess a weakly negative surface charge (ca. -10 mV). Because the kidney is both a size- and charge-selective filter (Fig. 4.1), renal nanoparticle accumulation is also expected to depend on the surface charge of the nanoparticle. Follow-up studies will investigate the fate of positive nanoparticles within the mesangium. One possiblity is that positive nanoparticles may irreversibly bind to the strongly negative glomerular basement membrane (GBM) without entering the mesangium. Another possibility is that such nanoparticles will non-specifically bind to negatively charged cell membranes of some other organs, drastically reducing their retention in the kidney. There has not been a careful study that mechanistically examines the effect of surface charge on blood pharmacokinetics and in vivo distribution. From the above, mechanistic studies show the fate of i.v. administered nanoparticles in the liver, spleen, and kidney, chief organs of retention for normal mice. Their results can be extended to examine the pharmacological behavior of nanoparticle-based therapeutics in disease animal models (e.g., cancer).

In tumor-bearing animals, the in vivo distribution patterns of the liver and kidney are similar to those observed in normal mice. In Chapter 2, because PEGylated gold nanoparticles of different sizes have PEG coatings of the same length (PEG_{5000}), they do not have the same ζ-potential (unlike Chapter 4). The liver (most notably Kupffer cells) removes Au_x-PEG_{5000} NPs in a size-dependent fashion (Fig. 2.5), whereas the renal corpuscles are the sinks for particle deposition (Fig. 2.7). In the tumor, regardless of the particle size, i.v. injected Au_x-PEG_{5000} NPs slowly accumulate in the interstitium by the enhanced permeation and retention (EPR) effect (Fig. 2.1), and constantly lie in the vicinity of leukocytes (Fig. 2.3). Under extremely rare instances do the smaller nanoparticles (ca. 40 nm) enter the cancerous cells and get entrapped in vesicles. For therapeutic nanoparticles to maximize their efficacy, they need to arrive at specific intracellular locations of cancer cells. Mechanical methods employ physical forces to directly deliver nanoparticles into intracellular locations (e.g., nuclei, cytoplasm). Microinjection uses capillary forces to insert nanoparticles under an optical microscope [219]. While capillary forces are sufficiently gentle to ensure cell viability, microinjection is low-throughput, technically demanding, and expensive. Electroporation uses a high-voltage electric field to transiently create hydrophilic perforations in the cell membrane, facilitating the diffusion of nanoparticles into the cell [220]. While electric forces can deliver multiple nanoparticle types to multiple cell lines, the strong pulses can cause cell death. Viral-based platforms (e.g., adenovirus or lentivrus) can deliver nucleic acids with high efficiency, but their intractability due to random insertions into the host genome induces toxicity that limits their potential for safe clinical applications [221]. Because this thesis emphasizes on cellular targeting via systemic injections of non-viral nanoparticles, both mechanical and viral delivery strategies are beyond the scope of this thesis.

In Chapter 3, we examine the mechanism of active targeting of cancer cells by injecting PEGylated gold nanoparticles (Au_{50}-PEG_{5000}-Tf_x NPs) that contain various amounts of human transferrin (a targeting ligand that engages the transferrin receptors in cancer cells within the tumor) into mice bearing subcutaneous tumors. To allow for a mechanistic analysis, all Au_{50}-PEG_{5000}-Tf_x NPs share a near-constant size and surface charge (ca. 75 nm and -10 mV) although their ligand content spans two orders of magnitude (Fig. 3.4). With multiple copies of transferrin ligands, these nanoparticles can bind to transferrin receptors overexpressed on cancer cells at a much higher affinity than the free transferrin counterpart (multivalency effect; Fig. 3.6). At the organ level, targeted nanoparticles accumulate in the bulk tumor (due the EPR effect) by the same magnitude (2% ID), independent of ligand content (Fig. 3.7). At the tissue and cellular levels, they can only internalize into cancer cells (specifically endosomal vesicles) in significant amounts above a threshold ligand content (between 18 and 144 ligands per nanoparticle) (Fig. 3.8). Below this threshold, targeted nanoparticles behave very similarly to their untargeted counterparts, and would not target cancer cell receptors effectively. In the liver (whereby hepatocytes only express transferrin receptors much more weakly than cancer cells), targeted nanoparticles rarely deposit inside hepatocytes even above the same threshold ligand content (Fig. 3.9). Most nanoparticles experience phagocytic clearance by Kupffer cells, thus explaining the high bulk retention in the liver (ca. 18% ID). Thus, active targeting does not affect the bulk localization of nanoparticles in the tumor, but only affects their internalization into target cells provided a sufficiently high ligand content to engage surface cell receptors. From modeling based on simple classical kinetics, effective receptor-ligand binding can be possible when both nanoparticle ligand content and cell receptor density are high (Fig. 3.10). In summary, we elucidate the mechanism of active targeting in vivo by fixing the particle size and surface charge, and by using tumors derived from only one cell line. Future work can explore the mechanism using nanoparticles of a different size and surface charge, tumor models with different expression levels of cancer cell surface receptors, as well as different ligand-receptor systems to test the generality of this ligand/receptor content threshold for effective internalization into target cancer cells.

Based on fluid mechanical grounds, Au_x-PEG_y NPs as model probes can validly mimic the in vivo flow pattern of therapeutic nanoparticles of the same size (Appendix B) despite their much higher density compared to actual therapeutic nanoparticles (cyclodextrin, lipid, polymer, nucleic acid). While the bulk accumulation in the tumor is somewhat limited (2% ID), an interesting observation is that therapeutic nanoparticles can still lead to appreciable tumor regression and gene inhibition in animal models [152] [146]. A possible interpretation is that, with its enormous drug payload (ca. 2000 siRNA strands per nanoparticle), nanoparticles can impart their intended therapeutic action despite a tiny fraction reaching intracellular locations.

In Chapter 5, we apply mechanistic insights derived from model gold nanoparticle probes (Chapter 3) to understand the delivery of actual therapeutic nanoparticles. Over the past decade, Davis and colleagues have created two types of cyclodextrin-polymer (CDP) nanoparticle conjugates to encapsulate drug payloads based on small molecules (camptothecin; CPT) and nucleic acids (siRNAs). Both delivery systems (IT-101 and CALAA-01) are currently under clinical development. The investigatation of the pharmacological fate of both types of CDP-based nanoparticles calls for the creation of a sterically stable, water-compatible, and fluorescent chemical stain (Fig. 5.1). Based on PEGylated gold nanoparticles with surface decoration of multiple adamantane moieties (Au_5-PEG_{1000}-AD_{50} NPs), this chemical stain specifically can bind to the cyclodextrin cups of the CDP nanoparticles embedded in transfected cells (Fig. 5.6), tumor samples from animals (Fig. 5.10), and patient tumor biopsies (Fig. 5.12), ex vivo. The application of chemical stain permits the analysis of in vivo behavior of CDP-based therapeutic nanoparticles. In tumor-bearing animals, IT-101 nanoparticles are shown to passively target the tumor and accumulate inside cancer cells 24 h after injection, with its fluorescence signals of the chemical stain colocalizing to those of CPT. This suggests the successful delivery of CPT to cancer cells by the CDP nanoparticle platform in great abundance, in stark contrast to the delivery of free CPT that has short blood circulation (Fig. 5.11). From tumor biopsies collected from melanoma patients, staining shows that CALAA-01 nanoparticles can selectively target the tumor (at times arrive at intracellular locations) without accumulating in the skin. Interestingly, with human transferrin as targeting ligands, they accumulate in the tumor and enter cells in a dose-depedent fashion, whereby the dose of infusion positively correlates to the degree of accumulation (Fig. 5.12). Because melanoma cells highly express surface transferrin receptors, this “dose response” in human tumor biopsies is the first ever reported for targeted nanoparticles of any type, underscoring the utility of the CDP nanoparticle platform to achieve targeted delivery of siRNAs to intracellular locations in humans. With regards to this thesis, moreoever, dose-response is consistent with the mechanism of active targeting in that CALAA-01 nanoparticles (with the same hydrodynamic size as Au_{50}-PEG_{5000}-Tf_{144} NPs) contain an average of 133 Tf moieties per nanoparticle, above the threshold ligand content required for significant internalization into cancer cells as predicted by mechanistic studies illustred in Chapter 3.

In Chapter 5, the chemical stain is fluorescent due to the coupling of sulfur atoms from PEG_{1000} chains to surface gold atoms of Au_5-PEG_{1000}-AD_{50} NPs. Gold nanoparticles were the preferred material to construct the cyclodextrin stain because of their high electron density for detection by TEM. This fluorescence intensity, however, is very weak for sensitive detection under confocal microscopy. From our initial idea, Au_5-PEG_{1000}-AD_{50} NPs can bind to and reveal the presence of CDP nanoparticles at the tissue level (using confocal microscopy) as well as cellular level (using TEM). Unfortunately, the binding of the chemical stain to CDP nanoparticles to tissue sections for TEM imaging is unsuccessful, perhaps due to the poor penetration through the heavily polymerized Epon tissue block. Epon is a material of choice for enhanced morphology in tissue sections, but does not necessarily favor antigenic binding. Other tissue block materials (e.g., Lowicryl) or tissue-embedding methods are possible to enhance binding, but suffer from poor tissue morphology. Thus, if TEM is unnecessary for the imaging studies, a new approach to utilize more powerful contrast agents, such as quantum dots (for elevated fluorescence and attenuated tissue autofluorescence) [222] and second harmonic generation nanoprobes (for enhanced quantum yield and less quenching) [223], is needed for viewing under confocal microscopy.

Chapter 5 illustrates the ex vivo detection of CDP nanoparticles in tissue sections. At the forefront of imaging is the real-time, in vivo tracking of pharmacological events (following the administration of therapeutics) in a precise, sensitive, longitudinal (for prolonged imaging), highly resolved, and quantitative fashion, accompanied by an assortment of nanoparticle-based contrast agents. As another key component in the field of bionanotechnology besides drug delivery, in vivo imaging constitutes an indispensable tool in cancer research, clinical trials, and medical practice. Fluorescence imaging stays in the mainsteam, but the development of imaging techniques based on bioluminescent, optical, photoacoustic properties is underway. While current imaging technologies focus on tumor detection, future improved imaging systems will display the expression/activity of biomarker molecules, shed light on biological processes that influence drug pharmacodynamics, and provide simultaneous detection and ablation of tumors. The major stumbling block of nanoparticle-based in vivo imaging agents is their low target-to-noise ratio. The development of targeting strategies (passive and active) empowers the design and optimization of nanoparticle-based probes with augmented accumulation in tumors and subdued clearance (e.g., macrophage uptake by RES organs, non-specific tissue extravasation, and renal elimination). As a result, only 5% of the injected contrast agent can reach the target biological destination in appreciable amounts [224]. Clearly, effective in vivo targeting is of crucial importance in improving technologies for drug delivery and molecular imaging.

Ultimately, the success of nanoparticles for in vivo biomedical applications relies upon their ability to overcome biological barriers. Ongoing fundamental research to highlight structure-function relationships between nanoparticle physicochemical properties and pharmacological behavior is crucial to yield additional insights to tackle unanswered questions and overcome technical bottlenecks. Quantitative measurements on the kinetics, amount, mechanisms, and trajectories of in vivo nanoparticle trafficking are still in lack. More sophisticated material and bioconjugate chemistry methods are much required to fabricate nanosized objects with more fine-tuned properties and in a high throughput manner. Realization of these future goals, in conjunction with more comprehensive understanding in the pathophysiology of different disease types, will steer the rational design of more potent nanoparticle-based therapeutics and imaging agents to diagnose and combat human malignancies.

Appendix A

List of Common Methods

Animal manipulations are performed with sterile methods, in compliance with NIH Guidelines for Animal Care and approved by the Caltech Institutional Animal Care and Use Committee.

Dynamic light scattering (DLS)

Hydrodynamic diameter (HD) and ζ-potential (ZP) of AuNPs were measured using ZetaPals (Brookhaven Instruments Corporation). For HD measurements, the particle pellet was resuspended in 1.2 mL of deionized water or 1× PBS. Using the Smoluchowski model, reported HDs are average values from 3 runs of 3 min each. The refractive index of Au_x-PEG_y NPs is taken as 0.47, the common refractive index of gold. For ZP analysis, the pellet was re-suspended in 1.4 mL of 1 mM KCl. The pH of solution is set as 5.3 (pH of 1 mM KCl). Using the HD values measured above, reported ZPs are average values from 10 runs each with a target residual of 0.012 measured at a conductance of 320 ± 32 µS.

Inductively coupled plasma mass spectrometry (ICP-MS)

Homogenized organs were oxidized in 0.5 mL of acid mixture (70% HNO_3 and 35% HCl at a 3:1 volume ratio) in a microwave until they fully dissolved. After adding 20.5 mL of deionized water, the sample was centrifuged at $3200 \times g$ for 15 min to remove cell debris, leaving the supernatant for gold content analysis using HP 4500 ICP-MS (Agilent). Nebulization occurred with a flow of

1.3 L/min of argon using a Babbington type nebulizer in a pyrex Scott-type spray chamber. The argon plasma power was 1200 W with a flow of 15 L/min and an auxiliary flow of 1.1 L/min. A calibration curve of various concentrations of Au_x-PEG_y NPs was used to measure the gold content, using 2.5% HNO_3 and 0.42% HCl as the blank solvent and tissues from uninjected mice to account for background organ gold content.

Histology with silver enhancement

PFA-fixed tissue blocks (∼1 cm^3) were dehydrated using an increasing ethanol gradient and absolute xylene, followed by embedding in molten paraffin overnight. Semithin tissue sections of 3-5 µm thick were generated using an RM 2165 microtome (Leica) and mounted on Superfrost poly-L-lysine coated glass slides (Fisher). Deparrifinized sections were rehydrated with a reducing ethanol gradient and rinsed with deionized water for 5 times, dried, and stained for AuNPs using the Silver Enhancement Kit for Light and Electron Microscopy (Ted Pella) in the dark for 20 min at RT. After rinsing with running tap water for 2 min, sections were counter-stained with Gill's 3 hematoxylin and 1% eosin (in 95% ethanol) for 40 s each, dehydrated, and mounted with Permount for viewing under an Axioplan 2 light microscope (Zeiss) with a 40× objective.

Confocal immunofluorescence microscopy

Cells pretreated with IT-101 were fixed with 4% PFA (in 1× PBS) at RT for 15 min and permeabilized with pre-chilled acetone at −20 °C for 10 min. Alternatively, 2 cm^3 tissue blocks were fixed in 4% PFA for 3 d, immersed in 5% sucrose and 30% sucrose for 2 h each, and embedded in 9% gelatin (in 1× PBS). The gradual freezing of gelatin tissue blocks from RT to −80 °C allowed the generation of 10 µm-thick cryosections using a microtome at −25 °C. Sections were rinsed with 1× PBS to remove any surface gelatin and fixed with pre-chilled acetone at −20 °C for 20 min to permeabilize the cell membrane.

To detect any intracellular CDP-based nanoparticles, fixed and permeabilized cells or tissue sections were stained by Au_5-PEG_{1000}-AD_{50} NPs (resuspended in 1× PBS at a concentration of 1.5×10^{11} particles/mL). This staining solution may also contain fluorescently labeled antibodies or nucleic acids at appropriate dilutions (e.g., 1 µg/mL). Staining proceeded in the dark at RT for 2 h. After brief rinses with 1× PBS, slides were dried gently and mounted with Mowiol 4-88 (in 33% glycerol in 1× PBS) or ProLong Gold antifade reagent with DAPI (Invitrogen).

A Zeiss LSM 510 inverted confocal scanning microscope (with a Plan-Neofluar ×40/0.75 objective and up to 2× optical zoom) was used to collect the images. The excitation wavelengths of DAPI/CPT, Au_5-PEG_{1000}-AD_{50} NPs, and Cy3/AlexaFluor 555 (for labeling antibodies and nucleic acids) are 740 nm (two-photon laser), 488 nm (argon laser), and 543 nm (HeNe laser), respectively. Their corresponding emission filters are 400-460 nm, bandpass (BP) 500-550 nm infrared radiation (IR), and BP 560-610 nm IR, respectively. The measured resolution at which images were acquired is 512×512 pixels, and the image bit-depth is 8-bit. The Zeiss LSM Image Browser Software allows the extraction of images.

Transmission electron microscopy (TEM)

Fixed tissue blocks ($\sim$1 mm^3) were fixed in 2.5% glutaraldehyde (in 0.1 M sodium cacodylate, pH = 7.4) for 2 h, stained by 1% OsO_4 at 4 °C for 2 h, and 0.9% OsO_4 and 0.3% $K_3Fe(CN)_6$ at 4 °C for 2 h. Dehydration with an increasing ethanol gradient and propylene oxide enabled tissue embedding in Epon 812 resins (Electron Microscopy Sciences). Using a Diatome Ultra 45° diamond knife (EMS) on an Ultracut UCT ultramicrotome (Leica), 80 nm thick sections were deposited on carbon and formvar-coated, 200-mesh, nickel grids (EMS). Sections were stained with 0.2 µm-filtered 3% uranyl acetate (SPI Supplies) and Reynolds lead citrate [225] for visualization under a 120 kV BioTwin CM120 TEM (Philips).

Appendix B

Theoretical Considerations

An advantage of employing Au$_x$-PEG$_y$ NPs as model agents to optimize drug delivery processes lies in their ability to mimic the flow patterns of actual therapeutic nanoparticles. Here, we seek to justify the validity of using Au$_x$-PEG$_y$ NPs with simple arguments from fluid mechanics. Unless otherwise mentioned, this section assumes spherical geometry for Au$_x$-PEG$_y$ NPs.

A measure of the flow characteristics around a particle of radius R is the particle Reynolds number (Re_p), a ratio between the inertial and viscous forces acting on the particle due to its surrounding flow. Let ρ and μ be the density and viscosity of the fluid, and U be the imposed velocity field in tumor blood capillaries. If the Au$_x$-PEG$_y$ NPs and the actual therapeutic particle have the same size, their Re_p should be identical. Thus, the fluid flow around both particle types should have the same qualitative behavior. At body temperature, for water, $\rho = 992.2$ kg/m^3 and $\mu = 6.53 \times 10^{-4}$ Pa $\cdot$ s. The average blood flow in a tumor tissue is 10^{-2} m/s [226]. For an Au$_{50}$-PEG$_{5000}$ NP ($\sim$75 nm), $Re_p = 5 \times 10^{-4} \ll 1$, indicating low Re flow.

$$Re_p = \frac{\rho U R}{\mu}$$

The particle Péclet number (Pe) describes nature of particle movement under an imposed velocity. It compares the relative importance of convection and diffusion. For a spherical particle, the Stokes-Einstein relationship gives an expression for D, diffusion coefficient, and hence Pe.

C is the Cunningham slip correction factor that accounts for the breakdown of the no-slip boundary condition at the particle surface as the particle dimension approaches the mean free path of solvent molecules. At body temperature, and using $C = 5$ for a 75 nm particle, $Pe = 8$, implying that particle motion is largely due to the influence of convective forces. Because Pe solely depends on hydrodynamic size of the particle, both Au$_x$-PEG$_y$ NPs and actual therapeutic particles of the same size are pushed along the blood capillaries by convective forces.

$$Pe = \frac{UR}{D} = \frac{UR}{kTC/6\pi\mu R} = \frac{6\pi\mu U R^2}{kTC}$$

The Stokes number (St) is the ratio of stop distance to the characteristic length scale of flow, L. τ is the stopping time due to its encounter of an obstacle. A gold particle ($\rho_p = 19300$ kg/m^3) is much denser than any carbohydrate- or polymer-based actual therapeutic particle (e.g., $\rho_p = 1000$ kg/m^3 for β-cyclodextrins). The former should bear a higher inertial force to follow the streamline of blood flow in tumor capillaries than the latter. Based on histology images of the Neuro2A tumor, each turn in blood vessel (L) is around 5 µm width. St for Au$_x$-PEG$_y$ NPs is about $10^{-4} \ll 1$. For the actual therapeutic particle, St is 5×10^{-5}. Becauses $St \ll 1$ for Au$_x$-PEG$_y$ NPs and therapeutic nanoparticles, both will trace the fluid streamlines of tumor capillaries closely as they bypass irregular obstacles of the vasculature.

$$St = \frac{U\tau}{L} = \frac{2U}{9\mu L} C R^2 \rho_p$$

For all studies with Au$_x$-PEG$_y$ NPs discussed above, the i.v. injection concentration was kept constantly at 4.5×10^{11} particles per 0.1 mL of D5W per animal. Despite the dense surface engraftment of PEG chains ($\sigma = 0.1$), the i.v. administration of Au$_x$-PEG$_y$ NPs into animals at this concentration is not difficult. What governs the viscosity of this suspension?

In a given volume V that contains n spherical particles of radius R and volume v_s, the volume fraction of spheres, ϕ, is given below. Given an injection formulation of Au$_{50}$-PEG$_{5000}$ NPs (R = 37.5 nm), $\phi \sim 10^{-3} \ll 1$. Thus, the suspension is considered dilute. The effective viscosity, μ_{eff}, due to the introduction of a dilute suspension of uncharged, force-and torque-free colloidal particles (roughly appropriate for weakly charged Au$_x$-PEG$_y$ NPs) under symmetric straining motion in a Newtonian fluid is given below [227]:

$$\phi = \frac{nv_s}{V} = \frac{n}{V}\left(\frac{4}{3}\pi R^3\right) \qquad \frac{\mu_{eff}}{\mu} = 1 + \frac{5}{2}\phi$$

The order ϕ correction of μ stems from the additional deviatoric viscous dissipation. This equation assumes a similar density between the sphere (ρ_s) and surrounding fluid (ρ_f), and does not necessarily apply to the much denser gold particle suspension. To verify mathematically, consider the Cauchy momentum equation in the low Reynolds number regime ($Re_p \ll 1$), where g is the constant force of gravity acting on the sphere due to the density discrepancy:

$$0 = \nabla \cdot \sigma - \delta\rho g \implies \int \sigma_{ij} dV = \int \frac{d\sigma_{ik}}{dx_k} x_j dV + \int \Delta\rho g_i x_j dV$$

As g_i is a constant vector and hence can be pulled out of the volume integral, the right integral identically equals zero. This step ultimately leads to the derivation of Einstein's original μ_{eff} expression. The discrepancy in density between spheres and fluid is still permissible. This makes physical sense because, as a body force, gravity always act in the normal direction and never exerts any deviatoric stress to shear the spheres horizontally with the fluid. The sedimentation of the spheres and the shearing of fluid due to the suspension are orthogonal to each other.

The order ϕ correction to μ_{eff} is very limited because $\phi \ll 1$!

Bibliography

[1] K. D. Wittrup. Directed evolution in chemical engineering. *AIChE J.* **51**, 3084 (2005).

[2] D. Velegol, H. A. Jerri, J. J. McDermott, N. Chaturvedi. Microfactories for colloidal assemblies. *AIChE J.* **56**, 564 (2010).

[3] M. E. Davis. The rise and realization of molecular chemical engineering. *AIChE J.* **55**, 1636 (2009).

[4] V. Wagner, A. Dullaart, A.-K. Bock, A. Zweck. Nanotechnology and medicine. *Radiol.* **230**, 315 (2004).

[5] J. Yin. Chemical engineering and virology: Challenges and opportunities at the interface. *AIChE J.* **53**, 2202 (2007).

[6] R. S. Kane. Polyvalency: Recent developments and new opportunities for chemical engineers. *AIChE J.* **52**, 3638 (2006).

[7] M. C. Roco. Converging science and technology at the nanoscale: Opportunities for education and training. *Nat. Biotechnol.* **21**, 1247 (2003).

[8] K. Y. Kim. Research training and academic disciplines at the convergence of nanotechnology and biomedicine in the United States. *Nat. Biotechnol.* **25**, 359 (2007).

[9] R. F. Service. Nanotechnology takes aim at cancer. *Science* **310**, 1132 (2005).

[10] G. Zheng, F. Patolsky, Y. Cui, W. U. Wang, C. M. Lieber. Multiplexed electrical detection of cancer markers with nanowire sensor arrays. *Nat. Biotechnol.* **23**, 1294 (2005).

[11] J.-M. Nam, C. S. Thaxton, C. A. Mirkin. Nanoparticle-based bio-barcodes for the ultrasensitive detection of proteins. *Science* **301**, 1884 (2003).

[12] F. Xia, *et al.*. Colorimetric detection of DNA, small molecules, proteins, and ions using unmodified gold nanoparticles and conjugated polyelectrolytes. *Science* **107**, 10837 (2010).

[13] S. Kim, *et al.*. Near-infrared fluorescent type II quantum dots for sentinel lymph node mapping. *Nat. Biotechnol.* **22**, 9397 (2004).

[14] H. S. Choi, *et al.*. Rapid translocation of nanoparticles from the lung airspaces to the body of nanoparticles from the lung airspaces to the body. *Nat. Biotechnol.* **28**, 13001303 (2010).

[15] V. Wagner, A. Dullaart, A.-K. Bock, A. Zweck. The emerging nanomedicine landscape. *Nat. Biotechnol.* **24**, 1211 (2006).

[16] R. S. Langer, N. A. Peppas. Present and future applications of biomaterials in controlled drug delivery systems. *Biomater.* **2**, 201 (1981).

[17] R. Langer, J. Folkman. Polymers for the sustained release of proteins and other macromolecules. *Nature* **263**, 797 (1976).

[18] P. Colombo, R. Bettini, P. Santi, N. A. Peppas. Swellable matrices for controlled drug delivery: Gel-layer behaviour, mechanisms and optimal performance. *Pharm. Sci. Technol. Today* **3**, 198 (2000).

[19] R. K. Verma, B. Mishra, S. Garg. Osmotically controlled oral drug delivery. *Drug Dev. Ind. Pharm.* **26**, 695 (2000).

[20] L. S. Nair, C. T. Laurencin. Biodegradable polymers as biomaterials. *Prog. Polym. Sci.* **32**, 762 (2007).

[21] D. Schmaljohann. Thermo- and ph-responsive polymers in drug delivery. *Adv. Drug Deliver. Rev.* **58**, 1655 (2006).

[22] P. Burgess, *et al.*. On firm ground: IP protection of therapeutic nanoparticles. *Nat. Biotechnol.* **28**, 1267 (2010).

[23] T. M. Allen, P. R. Cullis. Drug delivery systems: Entering the mainstream. *Science* **303**, 1818 (2004).

[24] A. Bangham, R. Horne. Negative staining of phospholipids and their structural modification by surface-active agents as observed in the electron microscope. *J. Mol. Biol.* **8**, 660 (1964).

[25] G. Gregoriadis. Drug entrapment in liposomes. *FEBS Lett.* **36**, 292 (1973).

[26] M. L. Immordino, F. Dosio, L. Cattel. Stealth liposomes: Review of the basic science, rationale, and clinical applications, existing and potential. *Intl. J. Nanomed.* **1**, 297 (2006).

[27] T. M. Allen, A. Chonn. Large unilamellar liposomes with low uptake into the reticuloendothelial system. *FEBS Lett.* **223**, 42 (1987).

[28] A. L. Klibanov, K. Maruyama, V. P. Torchilin, L. Huang. Amphipathic polyethyleneglycols effectively prolong the circulation time of liposomes. *FEBS Lett.* **268**, 235 (1990).

[29] Y. Kaneda. Virosomes: Evolution of the liposome as a targeted drug delivery system. *Adv. Drug Deliv. Rev.* **43**, 197 (2000).

[30] F. Ahmed, *et al.*. Shrinkage of a rapidly growing tumor by drug-loaded polymersomes: pH-triggered release through copolymer degradation. *Mol. Pharm.* **3**, 340 (1974).

[31] A. S. L. Derycke, P. A. M. de Witte. Liposomes for photodynamic therapy. *Adv. Drug Deliv. Rev.* **56**, 17 (2004).

[32] V. P. Torchilin. Liposomes as delivery agents for medical imaging. *Mol. Med. Today* **2**, 242 (1996).

[33] P. Sapra, T. M. Allen. Ligand-targeted liposomal anticancer drugs. *Prog. Lipid Res.* **42**, 439 (2003).

[34] O. P. Medina, Y. Zhu, K. Kairemo. Targeted liposomal drug delivery in cancer. *Curr. Pharm. Des.* **10**, 2981 (2004).

[35] U. Scheffel, B. A. Rhodes, T. K. Natarajan, J. Henry N. Wagner. Albumin microspheres for study of the reticuloendothelial system. *J. Nucl. Med.* **13**, 498 (1972).

[36] P. A. Kramer. Albumin microspheres as vehicles for achieving specificity in drug delivery. *J. Pharm. Sci.* **63**, 1646 (1974).

[37] L. Zhang, *et al.*. Nanoparticles in medicine: Therapeutic applications and developments. *Clin. Pharmacol. Ther.* **83**, 761 (2008).

[38] H. Ringsdorf. Structure and properties of pharmacologically active polymers. *J. Polym. Sci. Pol. Sym.* **51**, 135 (1975).

[39] R. Langer, J. P. Vacanti. Tissue engineering. *Science* **260**, 920 (1993).

[40] E. Chiellini, R. Solaro. Biodegradable polymeric materials. *Science* **8**, 305 (1996).

[41] B. Jeong, Y. H. Bae, D. S. Lee, S. W. Kim. Biodegradable block copolymers as injectable drug-delivery systems. *Nature* **388**, 860 (1997).

[42] F. Kawai. Microbial degradation of polyethers. *Appl. Microbiol. Biotechnol.* **58**, 30 (2002).

[43] A. Guiotto, *et al.*. Anchimeric assistance effect on regioselective hydrolysis of branched PEGs: A mechanistic investigation. *Bioorg. Med. Chem.* **12**, 5031 (2004).

[44] A. Abuchowski, J. R. McCoy, N. C. Palczuk, T. van Es, F. F. Davis. Effect of covalent attachment of polyethylene glycol on immunogenicity and circulating life of bovine liver catalase. *J. Biol. Chem.* **252**, 3582 (1977).

[45] Y. Ashihara, T. Kono, S. Yamazaki, Y. Inada. Modification of E. coli L-asparaginase with polyethylene glycol: Disappearance of binding ability to anti-asparaginase serum. *Biochem. Biophys. Res. Commun.* **83**, 385 (1978).

[46] M. J. Knauf, *et al.*. Relationship of effective molecular size to systemic clearance in rats of recombinant interleukin-2 chemically modified with water-soluble polymers. *J. Biol. Chem.* **263**, 15064 (1988).

[47] K. Takahashi, H. Nishimura, T. Yoshimoto, Y. Saito, Y. Inada. A chemical modification to make horseradish peroxidase soluble and active in benzene. *Biochem. Biophys. Res. Commun.* **121**, 261 (1984).

[48] K. Yang, *et al.*. Tailoring structurefunction and pharmacokinetic properties of single-chain Fv proteins by site-specific PEGylation. *Protein Eng.* **16**, 761 (2003).

[49] R. Langer. Drug delivery and targeting. *Nature* **392**, S5 (1998).

[50] S. David, A. Abuchowski, Y. K. Park, F. F. Davis. Alteration of the circulating life and antigenic properties of bovine adenosine deaminase in mice by attachment of polyethylene glycol. *Clin. Exp. Immunol.* **46**, 649 (1981).

[51] A. Abuchowski, *et al.*. Cancer therapy with chemically modified enzymes. I. Antitumor properties of polyethylene glycol-asparaginase conjugates. *Cancer Biochem. Biophys.* **7**, 175 (1984).

[52] L. Roseng, H. Tolleshauge, T. Berg. Uptake, intracellular transport, and degradation of polyethylene glycol-modified asialofetuin in hepatocytes. *J. Biol. Chem.* **267**, 22987 (1992).

[53] S. Kubetzko, C. A. Sarkar, A. Pluckthun. Protein PEGylation decreases observed target association rates via a dual blocking mechanism. *Mol. Pharmacology* **68**, 1439 (2005).

[54] S. Kumar, J. Aaron, K. Sokolov. Directional conjugation of antibodies to nanoparticles for synthesis of multiplexed optical contrast agents with both delivery and targeting moieties. *Nat. Protocol* **3**, 314 (2008).

[55] L. W. Seymour, R. Duncan, J. Strohalm, J. Kopecek. Effect of molecular weight (mw) of n-(2-hydroxypropyl)methacrylamide copolymers on body distribution and rate of excretion after subcutaneous, intraperitoneal, and intravenous administration to rats. *J. Biomed. Mat. Res.* **21**, 1341 (1987).

[56] T. Yamaoka, Y. Tabata, Y. Ikada. Distribution and tissue uptake of poly(ethylene glycol) with different molecular weights after intravenous administration to mice. *J. Pharm. Sci.* **83**, 601 (1994).

[57] F. M. Veronese, G. Pasut. Pegylation, successful approach to drug delivery. *Drug Discover. Today* **10**, 1451 (2005).

[58] R. B. Greenwald, A. Pendri, D. Bolikal, C. W. Gilbert. Highly water soluble taxol derivatives: 2'-polyethyleneglycol esters as potential prodrugs. *Bioorg. Med. Chem. Lett.* **4**, 2465 (1994).

[59] R. B. Greenwald, *et al.*. Drug delivery systems. 2. Camptothecin 20-o-poly(ethylene glycol) ester transport forms. *J. Med. Chem.* **39**, 1938 (1996).

[60] F. M. Veronese, *et al.*. PEG-doxorubicin conjugates: Influence of polymer structure on drug release, in vitro cytotoxicity, biodistribution, and antitumor activity. *Bioconjugate Chem.* **16**, 775 (2005).

[61] C. Kojima, Y. Toi, A. Harada, K. Kono. Preparation of poly(ethylene glycol)-attached dendrimers encapsulating photosensitizers for application to photodynamic therapy. *Bioconjugate Chem.* **18**, 663 (2007).

[62] H. Yang, S. T. Lopina. Stealth dendrimers for antiarrhythmic quinidine delivery. *J. Mater. Sci.: Mater. Med.* **18**, 2061 (2007).

[63] S. Mitragotri, J. Lahann. Physical approaches to biomaterial design. *Nat. Mater.* **8**, 15 (2009).

[64] L. Y. T. Chou, K. Ming, W. C. W. Chan. Strategies for the intracellular delivery of nanoparticles. *Chem. Soc. Rev.* **40**, 233 (2011).

[65] P. Vallance, T. G. Smart. The future of pharmacology. *Br. J. Pharmacol.* **147**, S304 (2001).

[66] D. Andes, W. A. Craig. Animal model pharmacokinetics and pharmacodynamics: A critical review. *Int. J. Antimicrob. Agents* **19**, 261 (2002).

[67] P. Lees, F. M. Cunningham, J. Elliot. Principles of pharmacodynamics and their applications in veterinary pharmacology. *J. Vet. Pharmacol. Therap.* **27**, 397 (2004).

[68] N. G. Khlebtsov, L. A. Dykman. Optical properties and biomedical applications of plasmonic nanoparticles. *J. Quant. Spectrosc. Radiat. Transfer* **111**, 1 (2010).

[69] V. Sharma, K. Park, M. Srinivasarao. Colloidal dispersion of gold nanorods: Historical background, optical properties, seed-mediated synthesis, shape separation and self-assembly. *Mater. Sci. Engr. R* **65**, 1 (2009).

[70] M. Faraday. The Bakerian lecture: Experimental relations of gold (and other metals) to light. *Philosophical Transactions Royal Soc. London* **147**, 145 (1857).

[71] R. A. Zsigmondy, *The Chemistry of Colloids* (John Wiley and Sons, 1917).

[72] T. Svedberg, *The Formation of Colloids* (D. Van Nostrand Company, 1921).

[73] A. Einstein. Investigations on the theory of Brownian movement. *Annalen der Physik* **17**, 549 (1905).

[74] M. Smoluchowski. On the kinetic theory of Brownian motion and of suspensions. *Annalen der Physik* **326**, 756 (1906).

[75] P. Langevin. The theory of Brownian movement. *Comptes Rendus Hebdomadaires des Seances de l'Academie des Sciences* **146**, 530 (1908).

[76] A. K. Oyelere, P. C. Chen, X. Huang, I. H. El-Sayed, M. A. El-Sayed. Peptide-conjugated gold nanorods for nuclear targeting. *Bioconjugate Chem.* **18**, 1490 (2007).

[77] N. G. Khlebtsov, L. A. Dykman. Biodistribution and toxicity of engineered gold nanoparticles: A review of in vitro and in vivo studies. *Chem. Soc. Rev.* **40**, 1647 (2011).

[78] G. F. Paciotti, *et al.*. Colloidal gold: A novel nanoparticle vector for tumor directed drug delivery. *Annu. Rev. Immunol.* **11**, 169 (2004).

[79] J. A. Schwartz, *et al.*. Feasibility study of particle-assisted laser ablation of brain tumors in orthotopic canine model. *Cancer Res.* **69**, 1659 (2009).

[80] J. Turkevich, G. Garton, P. C. Stevenson. The color of colloidal gold. *J. Colloid Sci.* **9**, 26 (1954).

[81] G. Frens. Controlled nucleation for the regulation of the particle size in monodisperse gold suspensions. *Nat. Phy. Sci.* **241**, 20 (1972).

[82] G. Mie. Contributions on the optics of turbid media, particularly colloidal metal solutions. *Annalen der Physik* **25**, 377 (1908).

[83] W. H. DeJong, *et al.*. Particle size-dependent organ distribution of gold nanoparticles after intravenous administration. *Biomater.* **29**, 1912 (2008).

[84] G. Danscher. Histochemical demonstration of heavy metals. *Histochem.* **71**, 1 (1981).

[85] B. D. Chithrani, A. A. Ghazani, W. C. W. Chan. Determining the size and shape dependence of gold nanoparticle uptake into mammalian cells. *Nano Lett.* **6**, 662 (2006).

[86] E. E. Connor, J. Mwamuka, A. Gole, C. J. Murphy, M. D. Wyatt. Gold nanoparticles are taken up by human cells but do not cause acute cytotoxicity. *Small* **1**, 325 (2005).

[87] C. M. Goodman, C. D. McCusker, T. Yilmaz, V. M. Rotello. Toxicity of gold nanoparticles functionalized with cationic and anionic side chains. *Bioconjugate Chem.* **15**, 897 (2004).

[88] C. J. Murphy, *et al.*. Gold nanoparticles in biology: Beyond toxicity to cellular imaging. *Acc. Chem. Res.* **41**, 1721 (2008).

[89] M. Luck, *et al.*. Identification of plasma proteins facilitated by enrichment on particulate surfaces: Analysis by two-dimensional electrophoresis and N-terminal microsequencing. *Electrophoresis* **18**, 2961 (1997).

[90] A. Gessner, *et al.*. Nanoparticles with decreasing surface hydrophobicities: Influence on plasma protein adsorption. *Int. J. Pharm.* **196**, 245 (2000).

[91] M. A. Dobrovolskaia, *et al.*. Interaction of colloidal gold nanoparticles with human blood: Effects on particle size and analysis of plasma protein binding profiles. *Nanomed.* **5**, 106 (2009).

[92] B. Balakrishnan, D. Kumar, Y. Yoshida, A. Jayakrishnan. Chemical modification of poly(vinyl chloride) resin using poly(ethylene glycol) to improve blood compatibility. *Biomaterials* **26**, 3495 (2005).

[93] M. Yang, H. C. Yau, H. L. Chan. Adsorption kinetics and ligand-binding properties of thiol-modified double-stranded DNA on a gold surface. *Langmuir* **14**, 6121 (1998).

[94] P. D. Jadzinsky, G. Calero, C. J. Ackerson, D. A. Bushnell, R. D. Kornberg. Structure of a thiol monolayer-protected gold nanoparticle at 1.1 resolution. *Science* **318**, 430 (2007).

[95] M. Brust, M. Walker, D. Bethell, D. J. Schiffrin, R. Whyman. Synthesis of thiol-derivatized gold nanoparticles in a two-phase liquid-liquid system. *J. Chem. Soc. Chem. Commun.* **7**, 801 (1994).

[96] T. OCallaghan. The prevention agenda. *Nature* **471**, S2 (2011).

[97] A. Jemal, R. Siegel, J. Xu, E. Ward. Cancer statistics, 2010. *CA Cancer J. Clin.* **60**, 277 (2010).

[98] M. Ferrari. Cancer nanotechnology: Opportunities and challenges. *Nat. Rev. Cancer* **5**, 161 (2005).

[99] J. W. Park, *et al.*. Anti-HER2 immunoliposomes: Enhanced efficacy attributable to targeted delivery. *Clin. Cancer Res.* **8**, 1172 (2002).

[100] M. F. Kircher, U. Mahmood, R. S. King, R. Weissleder, L. Josephson. A multimodal nanoparticle for preoperative magnetic resonance imaging and intraoperative optical brain tumor delineation. *Cancer Res.* **63**, 8122 (2003).

[101] J.-M. Nam, S. I. Stoeva, C. A. Mirkin. Bio-bar-code-based DNA detection with PCR-like sensitivity. *J. Am. Chem. Soc.* **126**, 5932 (2004).

[102] H. Maeda, J. Wu, T. Sawa, Y. Matsumura, K. Hori. Tumor vascular permeability and the EPR effect in macromolecular therapeutics: A review. *J. Control Release* **65**, 271 (2000).

[103] R. K. Jain. Physiological barriers to delivery of monoclonal antibodies and other macromolecules in tumors. *Cancer Res.* **50**, 814S (1990).

[104] Y. Matsumura, H. Maeda. A new concept for macromolecular therapeutics in cancer chemotherapy: Mechanism of tumoritropic accumulation of proteins and the antitumor agent Smancs. *Cancer Res.* **46**, 6387 (1986).

[105] V. P. Torchilin. Recent advances with liposomes as pharmaceutical carriers. *Nat. Rev. Drug Discov.* **4**, 145 (2005).

[106] D. Peer, *et al.*. Nanocarriers as an emerging platform for cancer therapy. *Nat. Nanotechnol.* **2**, 751 (2007).

[107] M. M. Gottesman, T. Fojo, S. E. Bates. Multidrug resistance in cancer: Role of ATP dependent transporters. *Nat. Rev. Drug Discov.* **2**, 48 (2002).

[108] R. K. Jain. Barriers to drug-delivery in solid tumors. *Sci. Am.* **271**, 58 (1994).

[109] S. A. Alexander. Adsorption of chain molecules with a polar head: A scaling description. *J. Phys. (Paris)* **38**, 983 (1977).

[110] P. G. de Gennes. Conformations of polymers attached to an interface. *Macromolecules* **13**, 1069 (1980).

[111] M. Daoud, J. P. Cotton. Star shaped polymers : A model for the conformation and its concentration dependence. *J. Phys. (Paris)* **43**, 531 (1982).

[112] Y. B. Z. T. M. Birshtein and, O. V. Boriso and, A. R. Khokhlov, T. A. Yurasova. Conformations of comb-like macromolecules. *Polymer Sci. U.S.S.R.* **29**, 1293 (1987).

[113] F. Kienberger, *et al.*. Static and dynamical properties of single poly(ethylene glycol) molecules investigated by force spectroscopy. *Single Mol.* **1**, 123 (2000).

[114] N. Dan, M. Tirrell. Polymers tethered to curved interfaces. A self-consistent-field analysis. *Macromolecules* **25**, 2890 (1992).

[115] K. C. Li, S. D. Pandit, S. Guccione, M. D. Bednarski. Molecular imaging applications in nanomedicine. *Biomed. Microdevices* **6**, 113 (2004).

[116] J. S. Murday, R. W. Siegel, J. Stein, J. F. Wright. Translational nanomedicine: Status assessment and opportunities. *Nanomed.: Nanotechnol. Biol. and Med.* **5**, 251 (2009).

[117] R. K. Jain. Transport of molecules in the tumor interstitium: A review. *Cancer Res.* **47**, 3039 (1987).

[118] Y. Tan, S. Li, B. R. Pitt, L. Huang. The inhibitory role of cpg immunostimulatory motifs in cationic lipid vector-mediated transgene expression in vivo. *Hum. Gene Ther.* **10**, 2153 (1999).

[119] F. Yuan, *et al.*. Vascular permeability in a human tumor xenograft: Molecular size dependence and cutoff size. *Cancer Res.* **55**, 3752 (1995).

[120] S. K. Hobbs, *et al.*. Regulation of transport pathways in tumor sessels: Role of tumor type and microenvironment. *Proc. Natl. Acad. Sci. USA.* **95**, 4607 (1998).

[121] A. Aderem, D. M. Underhill. Mechanisms of phagocytosis in macrophages. *Annu. Rev. Immunol.* **17**, 593 (1999).

[122] U. Hopf, G. Ramadori. Physiology and pathophysiology of the reticuloendothelial system of the liver. *Leber Magen Darm.* **10**, 277 (1980).

[123] H. S. Choi, *et al.*. Renal clearance of quantum dots. *Nat. Biotechnol.* **25**, 1165 (2007).

[124] L. F. Prescott, J. A. N. McAuslane, S. Freestone. The concentration-dependent disposition and kinetics of inulin. *Eur. J. Clin. Pharmacol.* **40**, 619 (1991).

[125] A. P. Chapman, *et al.*. Therapeutic antibody fragments with prolonged in vivo half-lives. *Nat. Biotechnol.* **17**, 780 (1999).

[126] S. S. Olmsted, *et al.*. Diffusion of macromolecules and virus-like particles in human cervical mucus. *Biophys. J.* **81**, 1930 (2001).

[127] A. Goel, *et al.*. Genetically engineered tetravalent single-chain Fv of the pancarcinoma monoclonal antibody CC49: Improved biodistribution and potential for therapeutic application. *Cancer Res.* **60**, 6964 (2000).

[128] G. F. Schreiner. The mesangial phagocyte and its regulation of contractile cell biology. *Am. Soc. Nephrol.* **2**, S74 (1992).

[129] H. Pavenstdt, W. Kriz, M. Kretzler. Cell biology of the glomerular podocyte. *Physiol. Rev.* **83**, 253 (2007).

[130] J. Wartiovaara, *et al.*. Nephrin strands contribute to a porous slit diaphragm scaffold as revealed by electron tomography. *J. Clin. Invest.* **114**, 1475 (2004).

[131] M. Karnovsky, S. K. Ainsworth. The structural basis of glomerular filtration. *Adv. Nephrol. Necker Hosp.* **2**, 35 (1972).

[132] S. D. Perrault, C. Walkey, T. Jennings, H. C. Fischer, W. C. W. Chan. Mediating tumor targeting efficiency of nanoparticles through design. *Nano Lett.* **9**, 1909 (2009).

[133] K. Ogawara, *et al.*. Hepatic uptake of polystyrene microspheres in rats: Effect of particle size on intrahepatic distribution. *J. Control Release* **59**, 15 (1999).

[134] W. M. Bogers, *et al.*. Kupffer cell depletion in vivo results in clearance of large-sized IgA aggregates in rats by liver endothelial cells. *Clin. Exp. Immunol.* **85**, 128 (1991).

[135] E. Sadauskas, *et al.*. Kupffer cells are central in the removal of nanoparticles from the organism. *Part. Fibre. Toxicol.* **4**, 1 (2007).

[136] C. Foglieni, *et al.*. Glomerular filtration is required for transfection of proximal tubular cells in the rat kidney following injection of DNA complexes into the renal artery. *Gene Therapy* **7**, 279 (2000).

[137] M. E. Davis, Z. Chen, D. M. Shin. Nanoparticle therapeutics: An emerging treatment modality for cancer. *Nat. Rev. Drug Discov.* **7**, 771 (2007).

[138] M. R. Dreher, *et al.*. Tumor vascular permeability, accumulation, and penetration of macromolecular drug carriers. *J. Natl. Cancer Inst.* **98**, 335 (2006).

[139] D. E. L. de Menezes, L. M. Pilarski, T. M. Allen. In vitro and in vivo targeting of immunoliposomal doxorubicin to human B-cell lymphoma. *Cancer Res.* **58**, 3320 (1998).

[140] Y. Zhou, *et al.*. Impact of single-chain Fv antibody fragment affinity on nanoparticle targeting of epidermal growth factor receptor-expressing tumor cells. *J. Mol. Biol.* **371**, 934 (2007).

[141] O. C. Farokhzad, *et al.*. Nanoparticle-aptamer bioconjugates: A new approach for targeting prostate cancer cells. *Cancer Res.* **64**, 7668 (2004).

[142] R. Bhattacharya, *et al.*. Attaching folic acid on gold nanoparticles using noncovalent interaction via different polyethylene glycol backbones and targeting of cancer cells. *Nanomed. Nanotechnol. Biol. Med.* **3**, 224 (2007).

[143] X. Montet, M. Funovics, K. Montet-Abou, R. Weissleder, L. Josephson. Multivalent effects of RGD peptides obtained by nanoparticle display. *J. Med. Chem.* **49**, 6087 (2006).

[144] S. R. Popierlarski, S. H. Pun, M. E. Davis. A nanoparticle-based model delivery system to guide the rational design of gene delivery to the liver. 1. Synthesis and characterization. *Bioconjugate Chem.* **16**, 1063 (2005).

[145] D. B. Kirpotin, *et al.*. Antibody targeting of long circulating nanoparticles does not increase tumor localization but does increase internalization in animal models. *Cancer Res.* **66**, 6732 (2006).

[146] D. W. Bartlett, H. Su, I. J. Hildebrandt, W. A. Weber, M. E. Davis. Impact of tumor-specific targeting on the biodistribution and efficacy of siRNA nanoparticles measured by multimodality in vivo imaging. *Proc. Natl. Acad. Sci. USA.* **104**, 15549 (2007).

[147] M. M. Schmidt, K. D. Wittrup. A modeling analysis of the effects of molecular size and binding affinity on tumor targeting. *Mol. Cancer Ther.* **8**, 2861 (2009).

[148] K. C. Gatter, G. Brown, I. S. Trowbridge, R. E. Woolston, D. Y. Mason. Transferrin receptors in human tissues: their distribution and possible clinical relevance. *J. Clin. Pathol.* **36**, 539 (1983).

[149] S. T. Sawyer, S. B. Krantz. Transferrin receptor number, synthesis and endocytosis during erythropoietin-induced maturation of Friend virus-infected erythroid cells. *J. Biol. Chem.* **261**, 9187 (1986).

[150] B. S. Stein, H. H. Sussman. Peptide mapping of the human transferrin receptor in normal and transformed cells. *J. Biol. Chem.* **258**, 2668 (1983).

[151] C. A. Enns, E. A. Rutledge, A. M. Williams. The transferrin receptor. *Biomembranes* **4**, 255 (1996).

[152] S. Hu-Lieskovan, J. D. Heidel, D. W. Bartlett, M. E. Davis, T. J. Triche. Sequence-specific knockdown of EWS-FLI1 by targeted, nonviral delivery of small interfering RNA inhibits tumor growth in a murine model of metastatic Ewing's sarcoma. *Cancer Res.* **65**, 8984 (2005).

[153] W. Jiang, B. Y. Kim, J. T. Rutka, W. C. W. Chan. Nanoparticle-mediated cellular response is size-dependent. *Nat. Nanotechnol.* **3**, 145 (2008).

[154] M. Moser, H. Pfister, R. M. Bruckmaier, J. Rehage, J. W. Blum. Blood serum transferrin concentration in cattle in various physiological states, in veal calves fed different amounts of iron, and in cattle affected by infectious and non-infectious diseases. *Zentralbl Veterinarmed A.* **41**, 413 (1994).

[155] S. P. Young, A. Bomford, R. Williams. The effect of the iron saturation of transferrin on its binding and uptake by rabbit reticulocytes. *Biochem. J.* **219**, 505 (1984).

[156] R. S. Lane. Differences between human Fe_1-transferrin molecules. *Br. J. Haematol.* **29**, 511 (1975).

[157] A. Ciechanover, A. L. Schwartz, A. Dautry-Varsat, H. F. Lodish. Kinetics of internalization and recycling of transferrin and the transferrin receptor in a human hepatoma cell line: Effect of lysosomotropic agents. *J. Biol. Chem.* **258**, 9681 (1983).

[158] M. Srivastava, N. O. Petersen. Diffusion of transferrin receptor clusters. *Biophys. Chem.* **75**, 201 (1998).

[159] K. Sato, *et al.*. Saccharated ferric oxide (SFO)-induced osteomalacia: In vitro inhibition by SFO of bone formation and 1, 25-dihydroxy-vitamin D production in renal tubules. *Bones* **21**, 57 (1997).

[160] M. E. Davis. The first targeted delivery of siRNA in humans via a self-assembling, cyclodextrin polymer-based nanoparticle: From concept to clinic. *Mol. Pharm.* **6**, 659 (2009).

[161] T. S. Zimmermann, *et al.*. RNAi-mediated gene silencing in non-human primates. *Nature* **6**, 111 (2006).

[162] H. S. Choi, *et al.*. Tissue- and organ-selective biodistribution of NIR fluorescent quantum dots. *Nano Lett.* **9**, 2354 (2009).

[163] F. C. Luft, *et al.*. Effects of moxalactam and cefotaxime on rabbit renal tissue. *Antimicrob. Agents Chemother.* **21**, 830 (1982).

[164] Y. S. Kanwar, M. G. Farquhar. Presence of heparan sulfate in the glomerular basement membrane. *Proc. Natl. Acad. Sci. USA.* **76**, 1303 (1979).

[165] S. Ogawa, *et al.*. High-resolution ultrastructural comparison of renal glomerular and tubular basement membranes. *Am. J. Nephrol.* **19**, 686 (1999).

[166] A.-T. Lahdenkari, *et al.*. Podocytes are firmly attached to glomerular basement membrane in kidneys with heavy proteinuria. *J. Am. Soc. Nephrol.* **15**, 2611 (2004).

[167] M. Tan, *et al.*. An effective targeted nanoglobular manganese(II) chelate conjugate for magnetic resonance molecular imaging of tumor extracellular matrix. *Mol. Pharm.* **7**, 936 (2010).

[168] M. L. Schipper, *et al.*. Particle size, surface coating, and PEGylation influence the biodistribution of quantum dots in living mice. *Small* **5**, 126 (2009).

[169] B. L. et al. In vitro effects of nanoparticles on renal cells. *Part. Fibre. Toxicol.* **5**, 1 (2008).

[170] Z. Chen, *et al.*. Acute toxicological effects of copper nanoparticles in vivo. *Toxicol. Lett.* **163**, 109 (2006).

[171] T. Sakai, W. Kriz. The structural relationship between mesangial cells and basement membrane of the renal glomerulus. *Anat. Embryol.* **176**, 373 (1987).

[172] S. Takae, *et al.*. Ligand density effect on biorecognition by PEGylated gold nanoparticles: Regulated interaction of RCA120 lectin with lactose installed to the distal end of tethered PEG strands on gold surface. *Biomacromolecules* **6**, 818 (2005).

[173] H. D. Hill, J. E. Millstone, M. J. Banholzer, C. A. Mirkin. The role radius of curvature plays in thiolated oligonucleotide loading on gold nanoparticles. *ACS Nano* **3**, 418 (2009).

[174] C. Wijmans, E. Zhulina. Polymer brushes at curved surfaces. *Macromolecules* **26**, 7214 (1993).

[175] M. E. Davis, M. E. Brewster. Cyclodextrin-based pharmaceutics: Past, present and future. *Nat. Rev. Drug Discov.* **3**, 1023 (2004).

[176] M. E. Davis, *et al.*. Self-assembling nucleic acid delivery vehicles via linear, water-soluble, cyclodextrin-containing polymers. *Curr. Med. Chem.* **11**, 179 (2004).

[177] J. Cheng, K. T. Khin, G. S. Jensen, A. Liu, M. E. Davis. Synthesis of linear, β-cyclodextrin-based polymers and their camptothecin conjugates. *Bioconjugate Chem.* **14**, 1007 (2004).

[178] M. E. Wall, *et al.*. Plant antitumor agents. I. The isolation and structure of camptothecin, a novel alkaloid leukemia and tumor inhibitor from Camptotheca acuminata. *J. Am. Chem. Soc.* **88**, 3888 (1966).

[179] F. M. Muggia, P. J. Creaven, H. H. Hansen, M. H. Cohen, O. S. Selawry. Phase I clinical trial of weekly and daily treatment with camptothecin (NSC-100880): Correlation with preclinical studies. *Cancer Chemother. Rep.* **56**, 515 (1972).

[180] T. Schluep, J. Cheng, K. T. Khin, M. E. Davis. Pharmacokinetics and biodistribution of the camptothecinpolymer conjugate IT-101 in rats and tumor-bearing mice. *Cancer Chemother. Pharmacol.* **57**, 654 (2006).

[181] T. Schluep, *et al.*. Preclinical efficacy of the camptothecin-polymer conjugate IT-101 in multiple cancer models. *Clin. Cancer Res.* **12**, 1606 (2006).

[182] T. Schluep, *et al.*. Pharmacokinetics and tumor dynamics of the nanoparticle IT-101 from PET imaging and tumor histological measurements. *Proc. Natl. Acad. Sci. USA.* **106**, 11394 (2009).

[183] J. D. Heidel, *et al.*. Potent siRNA inhibitors of ribonucleotide reductase subunit RRM2 reduce cell proliferation in vitro and in vivo. *Clin. Cancer Res.* **13**, 2207 (2007).

[184] N. M. Cerequeira, S. Pereira, P. A. Fernandes, M. J. Ramos. Overview of ribonucleotide reductase inhibitors: An appealing target in anti-tumor therapy. *Curr. Med. Chem.* **12**, 1283 (2005).

[185] D. W. Bartlett, M. E. Davis. Physicochemical and biological characterization of targeted, nucleic acid-containing nanoparticles. *Bioconjugate Chem.* **18**, 456 (2007).

[186] J. D. Heidel, *et al.*. Administration in non-human primates of escalating intravenous doses of targeted nanoparticles containing ribonucleotide reductase subunit M2 siRNA. *Proc. Natl. Acad. Sci. USA.* **104**, 5715 (2007).

[187] M. E. Davis, *et al.*. Evidence of RNAi in humans from systemically administered siRNA via targeted nanoparticles. *Nature* **464**, 1067 (2010).

[188] Z. Zhang, *et al.*. Fluorescent property of gold nanoparticles with different surface structures. *Chin. J. Phys. Chem.* **20**, 796 (2007).

[189] Q. J. Pan, Y. R. Guo, H. X. Zhang, H. G. Fu. Ab initio study on excited-state properties and weak metal-metal interaction of binuclear Au(I) complexes with phosphorus and/or thio ligands. *Acta. Chim. Sin.* **65**, 595 (2007).

[190] W. C. Cromwell, K. Bystrom, M. R. Eftink. Cyclodextrin-adamantanecarboxylate inclusion complexes: Studies of the variation in cavity size. *J. Phys. Chem.* **89**, 326 (1985).

[191] B. Ziomkowska, S. Kruszewski, R. Siuda, M. Cyrankiewicz. Deactivation rate of camptothecin determined by factor analysis of steady-state fluorescence and absorption spectra. *Optica Applicata* **36**, 137 (2006).

[192] A. Moore, E. Marecos, J. Alexei Bogdanov, R. Weissleder. Tumoral distribution of long-circulating dextran-coated iron oxide nanoparticles in a rodent model. *Radiology* **214**, 568 (2000).

[193] C. H. J. Choi, C. A. Alabi, P. Webster, M. E. Davis. Mechanism of active targeting in solid tumors with transferrin containing gold nanoparticles. *Proc. Natl. Acad. Sci. USA.* **107**, 1235 (2010).

[194] T. Numbenjapon, *et al.*. Preclinical results of camptothecin-polymer conjugate (IT-101) in multiple human lymphoma xenograft models. *Clin. Cancer Res.* **15**, 4365 (2009).

[195] D. Bumcrot, M. Manoharan, V. Koteliansky, D. W. Y. Sah. RNAi therapeutics: A potential new class of pharmaceutical drugs. *Nat. Chem. Biol.* **2**, 711 (2006).

[196] D. Castanotto, J. J. Rossi. The promises and pitfalls of RNA-interference-based therapeutics. *Nature* **457**, 426 (2009).

[197] R. Riehl, M. Schartl, G. Kollinger. Comparative studies on the ultrastructure of malignant melanoma in fish and human by freeze-etching and transmission electron microscropy. *J. Cancer Res. Clin. Oncol.* **107**, 21 (1984).

[198] K. Freudenberg, F. Cramer, H. Plieninger. Verfahren zur herstellung von einschlussverbindungen physiologisch wirksamer organischer verbindungen. *German Patent* **895769** (1953).

[199] O. C. Farokhzad, R. Langer. Impact of nanotechnology on drug delivery. *ACS Nano* **3**, 16 (2009).

[200] G. Glass. Pharmaceutical patent challenges – Time for reassessment? *Nat. Rev. Drug Discov.* **3**, 1057 (2004).

[201] J. A. Champion, S. Mitragotri. Role of target geometry in phagocytosis. *Proc. Natl. Acad. Sci. USA* **103**, 4930 (2006).

[202] S. E. A. Gratton, *et al.*. The effect of particle design on cellular internalization pathways. *Proc. Natl. Acad. Sci. USA* **105**, 11613 (2008).

[203] M. Bartneck, *et al.*. Rapid uptake of gold nanorods by primary human blood phagocytes and immunomodulatory effects of surface chemistry. *ACS Nano* **4**, 30733086 (2010).

[204] Arnida, M. Jant-Amsbury, A. Ray, C. Peterson, H. Ghandehari. Geometry and surface characteristics of gold nanoparticles influence their biodistribution and uptake by macrophages. *Eur. J. Pharm. Biopharm.* **77**, 417 (2011).

[205] M. R. Jones, *et al.*. DNA-nanoparticle superlattices formed from anisotropic building blocks. *Nat. Mater.* **9**, 913 (2010).

[206] E. K. Chow, *et al.*. Nanodiamond therapeutic delivery agents mediate enhanced chemoresistant tumor treatment. *Sci. Transl. Med.* **3**, 1 (2011).

[207] R. Maeda-Mamiya, *et al.*. In vivo gene delivery by cationic tetraamino fullerene. *Proc. Natl. Acad. Sci. USA* **107**, 5339 (2010).

[208] N. Lee, *et al.*. Magnetosome-like ferrimagnetic iron oxide nanocubes for highly sensitive MRI of single cells and transplanted pancreatic islets. *Proc. Natl. Acad. Sci. USA* **108**, 2662 (2011).

[209] M. A. Dobrovolskaia, S. E. McNeil. Immunological properties of engineered nanomaterials. *Nat. Nanotechnol.* **2**, 469 (2007).

[210] A. Nel. Air pollution-related illness: Effects of particles. *Science* **308**, 804 (2005).

[211] A. Nel, T. Xia, L. Madler, N. Li. Toxic potential of materials at the nanolevel. *Science* **311**, 622 (2006).

[212] E. Putman, J. van der Laan, H. van Loveren. Assessing immunotoxicity: Guidelines. *Fundam. Clin. Pharmacol.* **17**, 615 (2003).

[213] D. J. Snodin. Regulatory immunotoxicology: Does the published evidence support mandatory nonclinical immune function screening in drug development? *Regul. Toxicol. Pharmacol.* **40**, 336 (2004).

[214] Z. Zhang, *et al.*. MicroRNA-21 protects from mesangial cell proliferation induced by diabetic nephropathy in db/db mice. *FEBS Lett.* **583**, 2009 (2009).

[215] D. Michalk, R. Waldherr, H. P. Seelig, H. P. Weber, K. Schrer. Idiopathic mesangial IgA-glomerulonephritis in childhood: Description of 19 pediatric cases and review of the literature. *Eur. J. Pediatr.* **134**, 13 (1980).

[216] R. Habib, M. C. Gubler, C. Antignac, M. F. Gagnadoux. Diffuse mesangial sclerosis: A congenital glomerulopathy with nephrotic syndrome. *Adv. Nephrol. Necker. Hosp.* **22**, 43 (1993).

[217] S. A. Linehan, L. Martínez-Pomares, P. D. Stahl, S. Gordon. Mannose receptor and its putative ligands in normal murine lymphoid and nonlymphoid organs: In situ expression of mannose receptor by selected macrophages, endothelial cells, perivascular microglia, and mesangial cells, but not dendritic cells. *J. Exp. Med.* **189**, 1961 (1999).

[218] J. Huang, H. M. Siragy. Glucose promotes the production of interleukine-1 β and cyclooxygenase-2 in mesangial cells via enhanced (pro)renin receptor expression. *J. Exp. Med.* **150**, 5557 (2009).

[219] Y. Zhang, L.-C. Yu. Microinjection as a tool of mechanical delivery. *Curr. Opin. Biotechnol* **19**, 506 (2008).

[220] D. J. Stephens, R. Pepperkok. The many ways to cross the plasma membrane. *Proc. Natl. Acad. Sci. USA.* **98**, 4295 (2001).

[221] S. E. Martin, N. Caplen. Applications of RNA interference in mammalian systems. *Annu. Rev. Genomics Hum. Genet.* **8**, 81 (2007).

[222] V. Biju, T. Itoh, M. Ishikawa. Delivering quantum dots to cells: Bioconjugated quantum dots for targeted and nonspecific extracellular and intracellular imaging. *Chem. Soc. Rev.* **39**, 3031 (2010).

[223] P. Pantazis, J. Maloney, D. Wu, S. E. Fraser. Second harmonic generating (SHG) nanoprobes for in vivo imaging. *Proc. Natl. Acad. Sci. USA* **107**, 14535 (2010).

[224] R. Weissleder, M. J. Pittet. Imaging in the era of molecular oncology. *Nature* **452**, 580 (2008).

[225] E. S. Reynolds. The use of lead citrate at high pH as an electron-opaque stain in electron microscopy. *J. Cell Biol.* **17**, 208 (1963).

[226] R. K. Jain. Determinants of tumor blood flow: A review. *Cancer Res.* **48**, 2641 (1988).

[227] A. Einstein. A new determination of molecular dimensions. *Annalen der Physik* **19**, 289 (1906).